2012-6

A Study of Integrated UWB Antennas Optimised for Time Domain Performance

Antoine Dumoulin
Technological University Dublin

A STUDY OF INTEGRATED UWB ANTENNAS OPTIMISED FOR TIME DOMAIN PERFORMANCE

Antoine Dumoulin
Bachelor of Engineering

Doctor of Philosophy

Dublin Institute of Technology

Supervisor:
Professor Max J. Ammann

School of Electronic & Communication Engineering

JUNE 2012

ABSTRACT

Antennas for impulse radio ultra-wideband based portable devices are required to be compact and able to transmit or receive waveforms with minimal distortion in order to support proximity ranging with a centimetre-scale precision.

The first part of thesis characterises several pulse types for use in the generation of picosecond-scale signals in respect to the regulatory power and frequency standards while the principles of antenna transient transmission and reception are stated. The proximity effect of planar conductors on the performance of an ultra-wideband antenna is investigated in both spectral and temporal domain demonstrating the relationship between the antenna-reflector separation and the antenna performance. Balanced and unbalanced antennas are also investigated for integration into asset-tracking tag applications and are designed to operate in close proximity to PCB boards while meeting realistic dimensional constraints and acceptable time domain performances.

Monopole antenna designs are reported with performances optimized for minimum pulse dispersion. Minimization of pulse dispersion effects in the antenna designs is achieved using pulses with optimal spectral fit to the UWB emission mask. The generation of these waveforms are reported for the first time. An antenna de-embedding method is reported enabling validation of the simulated fidelity factor of radiated patterns. Novel differentially-fed planar dipole and slot antennas are reported for direct IC output integration. Design objectives and optimisation are focused on bandwidth enhancement and pulse dispersion minimisation. Finally, time- and frequency-domain measurements are carried out using an approach based on the superposition principle.

DECLARATION

I certify that this thesis which I now submit for examination for the award of PhD, is entirely my own work and has not been taken from the work of others save and to the extent that such work has been cited and acknowledged within the text of my own work.

This thesis was prepared according to the regulations for postgraduate study by research of the Dublin Institute of Technology and has not been submitted in whole or in part for an award in any other Institute or University.

The work reported on in this thesis conforms to the principles and requirements of the Institute's guidelines for ethics in research.

The Institute will waive its rights to lend or copy this thesis, in whole or in part, to a third party for a period of three years after the award of PhD is conferred. At the end of this period, the Institute will assume its usual rights for dissemination of research findings, unless Decawave Ltd, and AeroScout Ltd, inform DIT in writing that they do not wish for the information to be released. Use of any material from this thesis has to be duly acknowledged.

Signature: _____ Date: _____

Antoine Dumoulin

ACKNOWLEDGMENTS

First of all, I would like to thank Professor Max Ammann for his patience, availability and his support during my entire Ph.D. His advice, knowledge and management skills were invaluable and I consider myself fortunate to have him as a supervisor and as a friend.

I would like to thank especially, Matthias John for his insight in optimisation and antenna design and Pádraig McEvoy for his guidance, advice in measurement process, and writing skills.

Thanks to all my colleagues at the Antenna & High Frequency Research Centre, Abraham, Adam, Afshin, Domenico, Giuseppe, Maria, Oisín, Sergio, Shynu and Xiulong, for your assistances, friendship and nights out.

I would like to acknowledge, the Dublin Institute of Technology for providing the facilities, equipment, and the financial support during this work.

I would like to express my gratitude to my parents Anne and Daniel, to my sisters, Adeline and Ingrid, and to my brother in law, Francisco Guerrero, who encouraged me to pursue my studies, and gave me moral support.

Finally, I dedicate this work to my wife, Hélène, who provided me with invaluable and unconditional support during all my life in Ireland, and to my son, Gaël, who brought me joy and motivation during the last two years.

ACRONYMS

ABS	Acrylonitrile Butadiene Styrene
AUT	Antenna Under Test
AWG	Arbitrary Waveform Generator
CEPT	Conférence Européenne des administrations des Postes et Télécommunications
CPU	Central Processor Unit
CSS	Chirp Spread Spectrum
CST	Computer Simulation Technology GmbH
DAA	Detect And Avoid
DC	Direct Current
DS-CDMA	Direct Sequence Code Division Multiple Access
DS-UWB	Direct Sequence Ultra-Wideband
ECC	European Communication Commission
EIRP	Equivalent Isotropic Radiated Power
EM	Electromagnetic
ERO	European Radiocommunications Office
ETSI	European Technical Standards Institute
FCC	Federal Communication Commission
FFT	Fast Fourier Transform
FWHM	Full Width at Half Maximum
GA	Genetic Algorithm
IC	Integrated Circuits
IDA	Infocom Development Authority
IEEE	Institute of Electrical and Electronics Engineers
IFFT	Inverse Fast Fourier Transform
IR-UWB	Impulse Radio Ultra-Wideband
ISI	Inter Symbol Interference
LDC	Low Duty Cycle
MB-OFDM	Multi-Band Orthogonal Frequency Division Multiplexing
MIC	Ministry of Internal affairs and Communications
MIR	Micropower Impulse Radar
OFDM	Orthogonal Frequency Division Multiplexing
PAN	Personal Area Network

ParEGO	Parallel Efficient Global Optimiser
PCB	Printed Circuit Board
PSD	Power Spectrum Density
RF	Radio Frequency
RFID	Radio Frequency Identification
RTLS	Real Time Location System
SNR	Signal to Noise Ratio
SRD	Step Recovery Diode
SRRC	Square Root Raised Cosine
USAF	United State Air Force
UWB	Ultra-Wideband
VNA	Vector Network Analyser
VSWR	Voltage Standing Wave Ratio
WSN	Wireless Sensor Network

CONTENTS

ABSTRACT ..... **II**

DECLARATION ..... **III**

ACKNOWLEDGMENTS ..... **IV**

ACRONYMS ..... **V**

CONTENTS **1**

LIST OF FIGURES **4**

LIST OF TABLES **9**

CHAPTER 1: INTRODUCTION **10**

1.1. UWB REGULATION 12

1.2. MOTIVATION AND RESEARCH OBJECTIVES 14

1.2.1. Motivation for Bézier Spline Based Printed Antenna *15*

1.2.2. Motivation for Genetic Algorithm *16*

1.2.3. Motivation for Impulse Optimisation *17*

1.3. OUTLINE OF THE THESIS 18

CHAPTER 2: UWB ANTENNA CHARACTERISATION **20**

2.1. FREQUENCY-DOMAIN DESCRIPTORS 20

2.1.1. Input Impedance *20*

2.1.2. Input Reflection Coefficient *22*

2.1.3. Directivity *23*

2.1.4. Efficiency *24*

2.1.5. Gain *24*

2.1.6. Phase Centre *25*

2.1.7. Transmission Coefficient, Transfer Function and Group Delay *26*

2.2. TIME-DOMAIN CHARACTERISATION 28

2.2.1. Transmission Mode *28*

2.2.2. Reception Model *31*

2.3. TIME-DOMAIN DESCRIPTORS 33

2.3.1. Fidelity Factor *34*
2.4. MEASUREMENT SETUP 35
2.4.1. Frequency-domain Measurement Setup *35*
2.4.2. Time-domain Measurement Setup *36*
2.4.3. Coordinate Systems *39*
CHAPTER 3: UWB SIGNALS 40
3.1. UWB SIGNAL DEFINITIONS 40
3.2. TYPE OF UWB SIGNAL 43
3.2.1. Rectangular Pulse *43*
3.2.2. Gaussian Pulse *44*
3.2.3. Square Root Raised Cosine Pulse *48*
3.2.4. Chirp Signal *50*
3.2.5. Other UWB Pulses *51*
3.3. RADIATION OF UWB SIGNAL 53
3.4. RECEPTION OF UWB SIGNAL 55
3.5. CONCLUSION 57
CHAPTER 4: UWB MONOPOLE PERFORMANCE IN PROXIMITY TO PLANAR REFLECTORS 58
4.1. ANTENNA GEOMETRIES AND OPTIMISATION 58
4.1.1. Geometry *58*
4.1.2. Optimisation *59*
4.2. FREE SPACE RESULTS 61
4.2.1. Return Loss *61*
4.2.2. Radiation Pattern *61*
4.2.3. Fidelity Factor *62*
4.3. REFLECTOR PROXIMITY EFFECT ON ANTENNA PERFORMANCE 63
4.3.1. Return Loss *63*
4.3.2. Radiation Pattern *65*
4.3.3. Fidelity Factor *66*
4.4. CONCLUSION 69
CHAPTER 5: NOVEL METHOD FOR ANTENNA TIME-DOMAIN OPTIMISATION 70

5.1. MONOPOLE ANTENNA CONSTRUCTION AND MODELLING 71
5.2. DESIGN OPTIMISATION 72
5.3. FREQUENCY-DOMAIN RESULTS 74
5.3.1. Return Loss 74
5.3.2. Radiation Pattern 75
5.4. TIME-DOMAIN RESULTS 76
5.4.1. Simulation Results 76
5.4.2. Time-Domain Measurement Setup 79
5.4.3. Pulse Equalisation 81
5.4.4. Antenna Impulse Response De-embedding 82
5.4.5. Measured Time-domain Results 85
5.5. CONCLUSION 86

CHAPTER 6: DIFFERENTIALLY-FED UWB ANTENNAS 87

6.1. DIFFERENTIALLY FED BALANCED DIPOLE ANTENNAS 88
6.1.1. Geometry and Optimisation 88
6.1.2. Frequency-domain Results 91
6.1.3. Time-domain Results 92
6.2. DIFFERENTIALLY FED SLOT LIKE ANTENNAS 96
6.2.1. Elliptical Slot Antenna 96
6.2.2. Optimised Open Slot Antenna 100
6.3. CONCLUSION 105

CHAPTER 7: CONCLUSION 106

CHAPTER 8: FUTURE WORK 109

LIST OF PUBLICATIONS 119

JOURNAL PUBLICATION 119
INVITED CONFERENCE PUBLICATION 119
CONFERENCE PUBLICATIONS 119

LIST OF FIGURES

Figure 1-1: MB-OFDM spectrum allocation for UWB radio 11

Figure 1-2: UWB EIRP mask of the different regulation bodies 13

Figure 1-3: ECC and MIC UWB EIRP mask for devices using mitigation techniques 14

Figure 2-1: Diagram of an antenna connected to a source and a transmission line ... 21

Figure 2-2: Network representation of a dipole 21

Figure 2-3: Block diagram representation of two port antenna system 27

Figure 2-4: Block diagram of transmitting antenna; 28

Figure 2-5: Block diagram of receiving antenna 31

Figure 2-6: Frequency-domain measurement setup 36

Figure 2-7: Photo of the frequency-domain measurement setup 36

Figure 2-8: Time-domain measurement setup 37

Figure 2-9: Photo of the time-domain measurement setup 38

Figure 2-10: Flow chart of the automated MATLAB script 38

Figure 2-11: Coordinate systems used for the radiation pattern and fidelity factor ... 39

Figure 3-1: UWB signal design points 41

Figure 3-2: IEEE 802.15.4 transmit mask for a modulated Gaussian signal (T_p=1.3 ns) 42

Figure 3-3: IEEE 802.15.4 transmit mask for a modulated rectangular pulse (T_p=1.5 ns) 42

Figure 3-4: Time-domain representation of a rectangular pulse 44

Figure 3-5: Frequency-domain representation of a rectangular pulse 44

Figure 3-6: Time-domain representation of a Gaussian pulse 45

Figure 3-7: Frequency-domain representation of a Gaussian pulse 45

Figure 3-8: Time-domain representation of Gaussian pulse derivatives 46

Figure 3-9: Frequency-domain representation of Gaussian pulse derivatives 46

Figure 3-10: Gaussian pulse modulated at 6.85 GHz 47

Figure 3-11: Power spectrum density of Gaussian pulse modulated at 6.85 GHz.....47

Figure 3-12: SRRC signal in terms of their roll-off factor.....49

Figure 3-13: Spectral representation of SRRC signal in terms of their roll-off factor 49

Figure 3-14: Modulated Gaussian and SRRC pulses.....50

Figure 3-15: Power spectrum density of Gaussian and SRRC pulses with the IEEE 802.15.4 spectrum mask for indoor use.....50

Figure 3-16: Chirp signal 51

Figure 3-17: Power spectrum density of a chirp signal.....51

Figure 3-18: Original and filtered SRD pulses 53

Figure 3-19: Original and filtered SRD pulse power spectrum density.....53

Figure 4-1: UWB monopole geometry and coordinate system.....59

Figure 4-2: UWB spline monopole optimisation goal in terms of iteration number .61

Figure 4-3: Simulated and measured S_{11} for the UWB spline monopole in free space 62

Figure 4-4: Measured free space radiation pattern of the UWB spline monopole.....62

Figure 4-5: Measured Fidelity Factor 63

Figure 4-6: Experimental setup.....64

Figure 4-7: S_{11} dependence on antenna–reflector separation.....64

Figure 4-8: S_{11} dependence on antenna–reflector separation from $\lambda/4$ to $\lambda/8$.....64

Figure 4-9: Realised gain radiation pattern angle vs. frequency in terms of antenna-reflector separation 65

Figure 4-10: Maximum directivity of the antenna system in term of antenna-reflector separation. 66
Figure 4-11: Input and antenna system impulse response in term of antenna-reflector separation 67
Figure 4-12: Impulse response fidelity factor for different antenna-reflector separation 68
Figure 4-13: 2D surface graph representing the measured normalised impulse response in terms of angle versus time. 68
Figure 5-1: Gaussian Monopole *GM* geometry and coordinate system..... 72
Figure 5-2: SRRC Monopole *SM* geometry and coordinate system 72
Figure 5-3: Monopole *GM* optimisation goal in terms of iteration number 74
Figure 5-4: S_{11} for monopole *GM* and monopole *SM* 75
Figure 5-5: Measured monopole *GM* radiation pattern in the θ=90° plane 75
Figure 5-6: Measured monopole S*M* radiation pattern in the θ=90° plane..... 76
Figure 5-7: Simulated Fidelity Factor for monopole antenna fed with modulated Gaussian and SRRC pulse..... 77
Figure 5-8: SRRC pulse: 2.5 GHz bandwidth, modulated at 6.85 GHz, with the peak value normalized to unity..... 78
Figure 5-9: Spectrum Power Density for 2.5 GHz bandwidth SRRC pulse at various centre frequencies..... 78
Figure 5-10: Tapered slot antenna optimised for time-domain performance in receiving mode 80
Figure 5-11: Time-domain measurement setup 80
Figure 5-12: *in(t)* waveform to AWG and *out(t)* pulse 81
Figure 5-13: Input, output and output equalized pulse Power Spectrum 82

Figure 5-14: UWB channel model 83

Figure 5-15: Simulated and measured radiated pulse 84

Figure 5-16: Received output signal *out*(t)*, 1st derivative pulse *out'(t),* simulated radiated signal $eRAD\_simulated\theta = 90°, \varphi = 0°, t$, measured radiated signal $eRAD\_measured\theta = 90°, \varphi = 0°, t$, normalised power spectrum density. 85

Figure 5-17: Measured and simulated Fidelity Factor for monopole GM and monopole SM with an equalized modulated SRRC excitation pulse 86

Figure 6-1: Modulated Gaussian and SRRC pulses 89

Figure 6-2: Power spectrum density of Gaussian and SRRC pulses with the IEEE 802.15.4 spectrum mask for indoor use 89

Figure 6-3: Gaussian dipole *GD* geometry and coordinate system 90

Figure 6-4: SRRC dipole *SD* geometry and coordinate system 90

Figure 6-5: S_{11} for dipole *GD* and *SD* 91

Figure 6-6: Measured dipole *GD* radiation pattern in the φ =90° plane 92

Figure 6-7: Measured dipole *SD* radiation pattern in the φ =90° plane 92

Figure 6-8: Time-domain measurement setup for differentially fed antennas 93

Figure 6-9: Dipole *SD* simulated and measured radiated signal at boresight 94

Figure 6-10: Dipole *GD* simulated and measured radiated signal at boresight 95

Figure 6-11: Power spectrum density of excitation signal derivative versus the measured radiated signals at boresight for dipole *GD* and *SD* 95

Figure 6-12: Measured and simulated Fidelity Factor for an antenna system for dipole *GD* and dipole *SD* with an equalized modulated SRRC excitation pulse 95

Figure 6-13: 3D model of an elliptical dipole integrated on 110 × 70 × 0.7 mm test board 97

Figure 6-14: Elliptical slot geometry and dimensions 98

Figure 6-15: S_{11} for different parameter sweeps; *A* (left), *B* (Right), *C* (centre) 99

Figure 6-16: Elliptical slot measured and simulated S_{11} 99

Figure 6-17: Measured elliptical radiation pattern in the φ =90° plane 100

Figure 6-18: Measured fidelity factor in the φ =90° plane 101

Figure 6-19: Optimised open slot antenna geometry and dimensions 101

Figure 6-20: Genetic Algorithm optimisation search landscape for the optimised open slot antenna 102

Figure 6-21: Optimised slot like antenna measured and simulated differential S_{11} .103

Figure 6-22: Measured optimised slot like antenna radiation pattern in the φ =90° plane 103

Figure 6-23: Optimised open slot fidelity factor 104

LIST OF TABLES

Table 3-1: Relationship between the input and radiated signal for different antennas 55

Table 3-2: Relationship between the received signal versus the incident field for different antennas 56

Table 4-1: UWB spline monopole geometry parameters (mm) 59

Table 5-1: Antennas geometry parameters (mm) 73

Table 5-2: Fidelity Factor values for antennas fed by Gaussian & SRRC pulses 78

Table 5-3: Fidelity Factor mean for narrow band SRRC pulses 79

Table 6-1: Dipole antennas dimensional constraints (mm) 89

Table 6-2: Elliptical slot antenna parameters (mm) 98

CHAPTER 1: INTRODUCTION

In the mid 1800's, James Clerk Maxwell expressed electromagnetism in the form of 20 equations, unifying the classic laws of the discipline [1]. In 1881, Oliver Heaviside reduced the complexity of Maxwell's theory by reformulating 12 of the 20 Maxwell equations using the curl and divergence operators. From this simplification, he ended up with four differential equations known now as the "Maxwell's equations" [2]. In 1897, Guglielmo Marconi sent the first ever wireless communication over open sea using spark-gap transmitters and in 1901, performed the first transatlantic communication from Poldhu, England to St. John's, Newfoundland using an array of 50 wires connected to the ground for transmission while using a 200 meters kite supported antenna for the reception [3]. Because of the spark-gap transmitter, the signal used by Marconi was inherently wideband. Since then the evolution of radio technology has greatly increased. For the following 3 decades, radio technology advancements mainly focussed on transmission of information using narrow bandwidth, due to the frequency congestion in the electromagnetic spectrum. However in the late 60's, researchers started to study Ultra Wide Band (UWB) technology. Between 1977 and 1989 the United State Air Force (USAF) had a program on the UWB system [4], and in the meantime some universities were focused on the interaction of short pulses with matter. In 1994 T.E. McEwan invented the Micropower Impulse Radar (MIR) which proves to be the first compact, inexpensive and low power radar, which consumes only microwatts from batteries [5].

In 2002, the Federal Communication Commission (FCC) allocated the 3.1 GHz to 10.6 GHz for UWB unlicensed use and a standardisation body known as the IEEE 802.15.3a working group was established to write the specification for the high-data-rate Personal Area Network (PAN) [6]. At the beginning, two different schemes were investigated, the Direct Sequence Code Division Multiple Access (DS-CDMA), and the Multi-Band Orthogonal Frequency Division Multiplexing (MB-OFDM). DS-CDMA is realised by spreading the spectrum of the transmitting signal by multiplying the latter with a signal that has a very large bandwidth. Consequently the Power Spectrum Density (PSD) of the transmitted signal is significantly lowered, limiting interferences with other radio systems. The UWB MB-OFDM scheme uses 14 subcarriers having 528 MHz of bandwidth each and divided into 6 groups as shown on Figure 1-1. The OFDM symbols can hop across subcarriers in each band group, but cannot hop between groups [7]. This provides greater flexibility to accommodate different existing regulations.

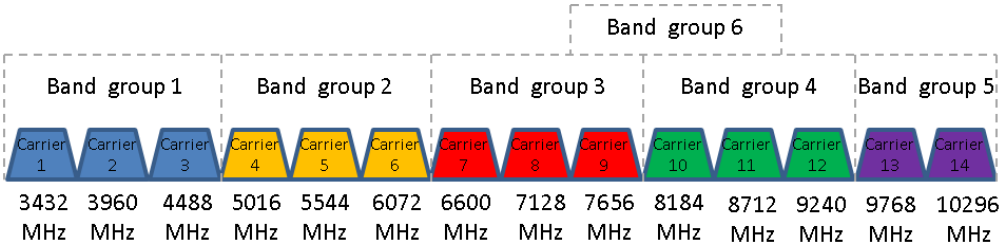

Figure 1-1: MB-OFDM spectrum allocation for UWB radio

Nevertheless the IEEE 802.15.3a task group ended up in deadlock and failed to consolidate the two approaches. However, it had setup the basis for the *WiMedia Alliance* which consists of a consortium of major electronics manufacturers.

Because of their very wide bandwidth, UWB signals have a high temporal resolution (typically less than 1ns), making this technology particularly suitable for Wireless Sensor Network (WSN) and Real Time Location System (RTLS).

However, these systems typically use low-data rate links. In March 2004, the IEEE 802.15.4a task group was officially created, and has been focusing on the standardisation of UWB radio for low-rate systems. This group chose to use two approaches for the physical layer, the Direct Sequence UWB (DS-UWB) and the Chirp Spread Spectrum (CSS) [8].

1.1. UWB Regulation

In May 2002, The FCC allocated a 7.5 GHz band ranging from 3.1 GHz to 10.6 GHz in the U.S.A. It limited the maximum Equivalent Isotropic Radiated Power (EIRP) for UWB radio to –41.3 dBm/MHz (74 nW/MHz) and specifies that a UWB signal must have, at any point in time, a fractional bandwidth equal to or greater than 20% or to have a 500 MHz bandwidth regardless of the fractional bandwidth [9]. The fractional bandwidth is given in Equation (1.1) where f_{low} and f_{high} represents the lower and upper limit of the signal spectrum.

$$BW_{frac}=2\,\frac{f_{low}-f_{high}}{f_{low}+f_{high}} \tag{1.1}$$

In February 2007, the European Communication Commission (ECC) released their decision for the use of UWB technology in Europe [10]. The organisations involved in regulations and standards are defined as follows. The European Radiocommunications Office (ERO) is the facilitator for the European Technical Standards Institute (ETSI) and for the European Conference of Postal and Telecommunications Administration (CEPT). ETSI deals with technical standards and electromagnetic compatibility issues while the CEPT is in charge of the UWB sharing and compatibility studies. Both of these organisations are conservative resulting in a more restrictive UWB spectrum mask. The ECC specifies that the

3.1 GHz to 4.8 GHz band could be used provided that mitigation techniques such Low Duty Cycle (LDC) and Detect And Avoid (DAA) are implemented.

In Asia the two most advanced UWB regulations are in Japan and Singapore. The Japanese UWB spectrum mask for indoor devices proposed by the Ministry of Internal affairs and Communications (MIC) has two bands [11]. The first band (3.4 GHz to 4.8 GHz) can be accessed if the DAA mitigation technique is implemented. Regarding Singapore, in early 2003, the agency in charge of the communication regulation, named Infocom Development Authority (IDA) created a UWB friendly Zone. Inside, researchers and companies can research, develop and test future UWB devices, using a frequency range starting at 2.2 GHz and finishing at 10.6 GHz with a maximum EIRP of –35 dBm/MHz (0.316 μW/MHz). A summary of the UWB mask for the different regulatory bodies is shown in Figure 1-2 while the UWB mask with mitigation techniques is shown in Figure 1-3.

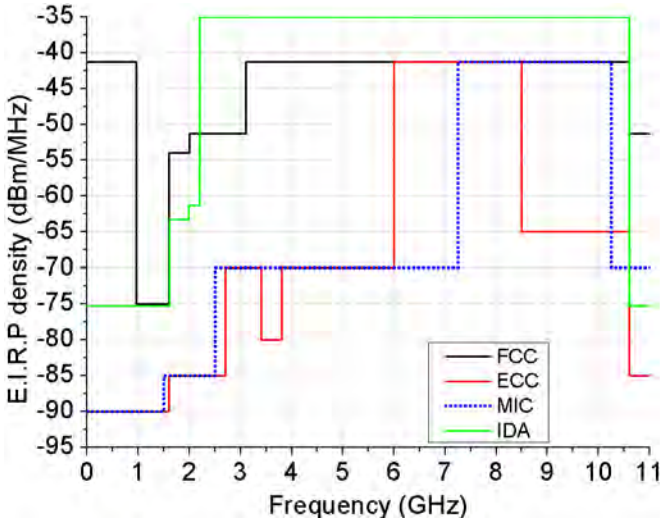

Figure 1-2: UWB EIRP mask of the different regulation bodies

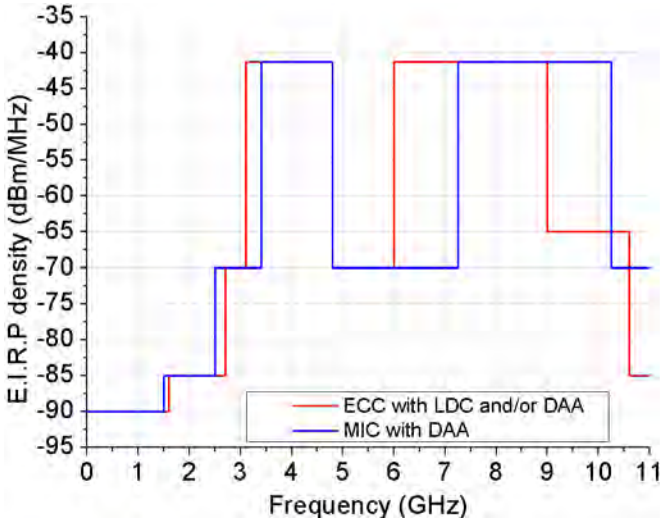

Figure 1-3: ECC and MIC UWB EIRP mask for devices using mitigation techniques

1.2. Motivation and Research Objectives

In any radio system the antenna is a crucial component because it is responsible for converting electrical currents to/from electromagnetic energy. For a UWB system the antennas need to maintain a broad matched return loss and a stable radiation pattern across an extremely wide bandwidth. For Impulse Radio UWB (IR-UWB) systems, the antenna should also transmit or receive a signal without adding distortion. To achieve this, the gain, group delay and the phase response should be linear across the entire frequency range. Any sharp variation in these parameters will impair the radiated or received signal. Also, IR-UWB antennas are most likely to be integrated into portable communication devices, such as laptops, tablet PCs, mobile phones and real time location and positioning systems (asset tag tracking and Radio Frequency Identification (RFID)). Consequently IR-UWB antennas should be low cost and low-profile while maintaining good performance, both in frequency- and temporal domain, when operating in an enclosure. Planar monopoles, dipoles and

slot antennas fulfil these requirements and hence are good candidates offering flexibility for different case scenarios.

1.2.1. Motivation for Bézier Spline Based Printed Antenna

The length of conventional antennas is proportional to the wavelength. For example, the length of thin cylindrical monopoles and dipoles is approximately a quarter and half of the free space wavelength respectively. In general the higher the frequency, the smaller the wavelength hence the smaller the antenna length [12].

UWB antennas are likely to find applications in portable devices. For the vast majority of portable device manufacturers, the electronic components are contained in the device's packaging, including the antennas. Nowadays, antennas can be easily printed on the same laminate as electronic components offering a saving in manufacturing costs. Furthermore, printed antennas exhibit broad bandwidth [13]. In the literature, most of the UWB antennas have been reported using canonical geometries [14] [15] [16]. However, for miniaturised antenna, Balanis has shown that the bandwidth of planar antennas (having their largest dimension equal of $2r$) can be improved only if its geometry best utilizes the available surface area of a circle of radius r that surrounds the antenna. [17]. To compensate for the limitation of canonical geometries, Bézier spline based geometries were implemented into planar antennas [18] [19]. A number of control points can be assigned to manipulate the shape of parametric curves. This allows the antenna design to have smooth and efficient geometric features while having a wider bandwidth and better radiation performances.

Planar antennas with canonical and spline geometries have been modelled, prototyped and measured. Design and optimisation methods were developed to maximize the bandwidth and radiation performance of the antenna in both

frequency- and time-domain. The goal is to propose an antenna design method which can be exploited by other researchers and industry.

1.2.2. Motivation for Genetic Algorithm

Optimisation algorithms are used by engineers and researchers to solve complex problems. The scope of these algorithms can range from resolution of a simple equation (i.e.: the Rastrigin's Function [20]) to the optimisation of complex problems such as space network communication scheduling [21]. These algorithms can be divided into two branches, local optimisers, and global optimisers. The local optimiser achieves good performance on simple problems or pre-optimised complex problems. On the other hand, global optimisers are very efficient at solving complex problems with a large search space and/or having many local optima. Evolutionary algorithms belong to the latter group. They were designed to digitally replicate natural mechanisms and have proven to be very efficient to solve complex electromagnetic problems [22] [23] [24]. A well-known global optimiser based on the natural selection principle is the Genetic Algorithm (GA). To find the optimum solution for a given problem, the GA encodes the problem's input variables as "chromosomes" and defines the cost function and the weight of each goal for multi-objective problems. From these parameters, the GA creates and computes an initial population of individuals. Each individual will have a cost which is the output of the cost function (the problem to solve). Then each individual will be sorted out and the best individuals will have a chance to mate with others, creating the offspring for the next generation. In order to avoid being stuck in local minima, mutation on chromosomes can also be implemented. Generally these occur with low probability, in order to limit the optimisation disruption and the destruction of information carried by the chromosomes. Finally the process is repeated until the GA converges

to a stable result, or when the optimised results satisfy particular thresholds. The main drawback is that a large number of evaluations are required to find an optimal or quasi-optimal goal, leading to long optimisation times, although this is compensated by the ever increasing Central Processor Unit (CPU) computational power.

To efficiently use the spline geometry, several construction points are required. Since the complexity of a problem increases with the number of variables, traditional optimisation is not suitable, and thus computational aided optimisation is required.

In this study a genetic algorithm provided by the software MATLAB [25] was interfaced with the Electromagnetic (EM) transient solver of CST Microwave Studio [26], to optimise planar antenna geometries.

1.2.3. Motivation for Impulse Optimisation

For conventional narrow band systems, the radiation characteristics and impedance bandwidth are the most important parameters. However for carrierless communications, such as DS-UWB, other parameters must be taken into consideration. To characterise the antenna transient performance, several spatially dependent metrics can be used such as the group delay, the phase centre or the fidelity factor (FF). The latter is defined as the maximum absolute value of the cross-correlation coefficient between two signals. It can be used as an optimisation goal to optimise an antenna for time-domain performance, by cross correlating the excitation signal (or its derivative), with the transmitted signals. This method has the advantage to include other metrics such as the transfer function magnitude and phase variation, simplifying the antenna performance analysis. From a regulatory point of view, the IEEE 802.15.4 standard specifies that the transmitted pulse should have a magnitude of the cross-correlation function at least equal to 0.8 and that any side lobe shall not

be greater than 0.3 [8]. Hence, the fidelity factor of IR-UWB antennas should be greater than 80% in order to satisfy the regulation. If the antenna does not achieve sufficient time-domain performance, it will result in the degradation of the RTLS system performance (precision, range).

All antennas designed were optimised for best impulse performance using manual parametric or genetic optimisation in combination with the fidelity factor method.

1.3. Outline of the Thesis

Chapter 2 introduces the principal descriptors used, in this thesis, to characterise the various type of antennas in the frequency- and time-domain. The antenna transmission-reception model is presented as well as the main measurement setups and scripts used throughout this work.

Chapter 3 presents various signals commonly used in the generation of UWB waveforms. Their temporal and spectral characteristics are compared and analysed regarding the UWB FCC emission mask and the principles of the radiation and reception of UWB signal are stated.

The main contributions of this thesis are presented in Chapter 4 to Chapter 7.

The proximity effects of a planar reflector on a UWB monopole antenna performance are reported in Chapter 4. The frequency- and time-domain performances of the antenna are illustrated in terms of the antenna-reflector separation and compared with free space results.

Chapter 5 deals with an improved optimisation technique for time-domain performance. This method is used to enhance the bandwidth and to achieve optimal

antenna transient characteristics in a broad or single direction. An improved method for time-domain measurement is also reported.

The designs of UWB differentially fed balanced antenna, for direct IC chip output integration is described in Chapter 6. Furthermore, integration and polarisation problems are studied and the design and miniaturisation of novel slots antennas for direct PCB board integration is discussed.

A general conclusion is given in Chapter 7 while possibilities of future work are discussed in Chapter 8.

CHAPTER 2: UWB ANTENNA CHARACTERISATION

The aim of this chapter is to introduce the most important parameters describing the performance of UWB antennas in the frequency- and time-domain. In the first section, the frequency-domain parameters are presented for both unbalanced and differentially-fed balanced antennas. The second section focuses on the transmission and reception models of UWB antennas, while the subsequent section presents the use and benefits of the time descriptor for UWB antenna time-domain characterisation. Finally the last section, introduces the different measurement setups and scripts leading to scientific and repeatable results.

2.1. Frequency-domain Descriptors

2.1.1. Input Impedance

Antennas are generally connected to a Radio Frequency (RF) transmitter or receiver using a feeding transmission line circuit. The characteristic impedances Z_C of the measurement instrumentation and devices including feeding circuit (i.e. coaxial cable) are usually 50 Ω. To convey the electric energy between the antenna and the measurement devices with minimum loss, the transmission lines (microstrip, co-planar waveguide, strips line, etc…) presented in this thesis, were designed for a 50 Ω characteristic impedance.

From a circuit point of view the antenna is seen as a load as shown on Figure 2-1. Its impedance can be defined as the ratio between the voltage and current at the

antenna terminals as seen on Equation (2.1), on which its real part is composed of material, radiation resistance and dielectric loss.

$$Z_{ANT}(f) = R_{ANT}(f) + jX_{ANT}(f) \tag{2.1}$$

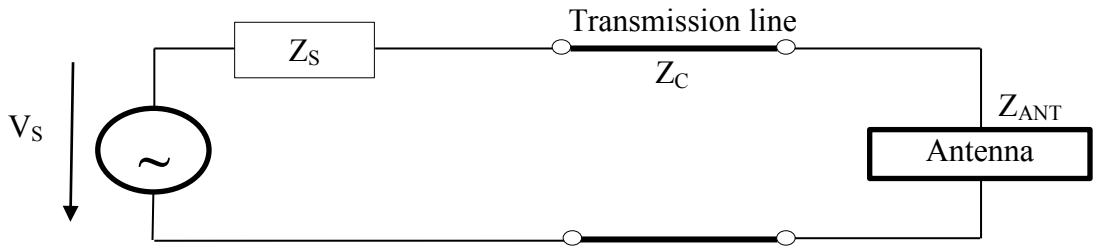

Figure 2-1: Diagram of an antenna connected to a source and a transmission line

For differentially-fed antennas their input impedance can be calculated from the definition of the Z parameter [27]. This type of antenna can be equivalent to a two port network as shown on Figure 2-2.

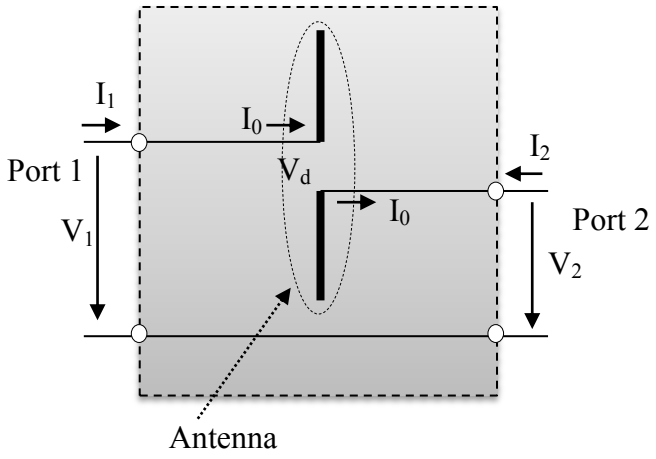

Figure 2-2: Network representation of a dipole

The voltage at the antenna ports can be defined as

$$V_1 = Z_{11}I_1 + Z_{12}I_2 \tag{2.2}$$

$$V_2 = Z_{22}I_2 + Z_{21}I_1 \tag{2.3}$$

by assuming that $I_0 = I_1 = -I_2$, then the differential voltage is determined by

$$V_d = V_1 - V_2 = I(Z_{11} - Z_{21} - Z_{12} - Z_{22}) \quad (2.4)$$

Thus the impedance $Z_{ANT\_differential}$ of an antenna fed with a differential signal can be deduced by

$$Z_{ANT\_differential} = \frac{V_d}{I_0} = (Z_{11} - Z_{21} - Z_{12} - Z_{22}) \quad (2.5)$$

2.1.2. Input Reflection Coefficient

The input reflection coefficient Γ indicates how well a circuit or device is matched in term of a reference impedance. If the impedance Z_{ANT} differs from the reference impedance Z_C then part of the current will be reflected back to the source reducing the power transmitted. In contrast, if the impedance Z_{ANT} is equal to the impedance Z_C then no reflection occurs and a maximum power transmission is achieved. For single ended antennas the magnitude of the coefficient Γ expressed in dB is commonly called S_{11} while for balanced antennas the differential mode input reflection coefficient refers to the mixed mode S-parameter S_{dd11}. The coefficient Γ is defined as follow

$$S_{dd11} = \Gamma = \frac{V_R}{V_I} = \frac{Z_{ANT} - Z_C}{Z_{ANT} + Z_C}$$
$$S_{dd11} = \Gamma = \frac{Z_{ANT\_differential} - Z_C}{Z_{ANT\_differential} + Z_C} \quad (2.6)$$

where V_R and V_I represent the reflected and incident voltage respectively. For the sake of simplicity, the S_{dd11} parameter will be called S_{11} for differentially fed antenna. The logarithmic magnitude of the coefficient Γ is defined in Equation (2.7)

$$\Gamma(dB) = 20log_{10}(|\Gamma|) \quad (2.7)$$

The voltage standing wave ratio (VSWR) can also be calculated from Equation (2.8) as follow

$$VSWR = \frac{1 + |\Gamma|}{1 - |\Gamma|} = \frac{V_{MAX}}{V_{MIN}} \tag{2.8}$$

where V_{MAX} and V_{MIN} represent the maximum and minimum amplitude of the standing wave, which is created by the mismatch between the antenna impedance and the characteristic impedance. The VSWR values range from 1:1 to ∞:1. Like the coefficient Γ, it indicates how good the match between an antenna and a transmission line is. A perfect impedance matching will translate into a VSWR equal to 1:1.

In this thesis, the bandwidth of antenna is found by calculating the frequency range where the S_{11}(dB) values are consecutively below a threshold, typically set at −10 dB or −6 dB. Notice that the equation of the fractional bandwidth was defined in Equation (1.1).

2.1.3. Directivity

The radiation pattern directivity is calculated by the ratio of the radiation intensity in a given direction $P_{rad}(\theta,\varphi,\omega)$ to the average radiation intensity in all directions, ω being the angular frequency ($2\pi f$). The isotropic radiated power $P_{iso\_rad}(\omega)$ being the average radiation power density multiplied by 4π, the directivity $D(\theta,\varphi,\omega)$ in any direction can be defined as

$$D(\varphi,\theta,\omega) = \frac{P_{rad}(\theta,\varphi,\omega)}{\frac{P_{iso\_rad}(\omega)}{4\pi}} \tag{2.9}$$

However to characterise an antenna the maximum directivity is usually taken and is represented as $D(\omega)$ as seen on Equation (2.10).

$$D(\omega) = max\big(D(\varphi,\theta,\omega)\big) \tag{2.10}$$

2.1.4. Efficiency

Another antenna performance indicator is the total efficiency which takes account of the dielectric and ohmic losses of the material used in the antenna and the losses due to mismatch. Radiation efficiency $EFF_{rad}(\omega)$ is defined as the ratio of the radiated power $P_{rad}(\omega)$ to the input power fed at the antenna port $P_{in}(\omega)$, with $EFF_{rad}(\omega)$ =1 representing the maximum energy transfer.

$$EFF_{rad}(\omega)=\frac{P_{rad}(\omega)}{P_{in}(\omega)} = \frac{EFF_C(\omega)\, EFF_D(\omega)\, P_{in}(\omega)}{P_{in}(\omega)} \tag{2.11}$$

where $EFF_C(\omega)$ is the conductive efficiency and $EFF_D(\omega)$ is the dielectric efficiency. The antenna total efficiency $EFF_{total}(\omega)$, also noted η, takes account of the radiation efficiency $EFF_{rad}(\omega)$ and the mismatch loss as defined in Equation (2.12).

$$\eta(\omega) = EFF_{total}(\omega)= EFF_{rad}(\omega)\,(1-|S_{11}|^2) \tag{2.12}$$

2.1.5. Gain

The realised gain $G_{real}(\omega)$ is proportionally related to the directivity by the radiation efficiency $EFF_{total}(\omega)$ of the antenna. It is defined as the ratio of the power radiated in a given direction to the power radiated by an isotropic antenna. To achieve a non-dispersive UWB antenna, it is desirable that the gain remains constant throughout the frequency range. Any abrupt change of the gain will likely impair the radiated or received signal.

$$G_{real}(\theta,\varphi,\omega) = D(\varphi,\theta,\omega)\, EFF_{total}(\omega) \tag{2.13}$$

At the time of writing this thesis, only a two port Vector Network Analyser (VNA) was available, making direct gain measurement of a differentially-fed balanced antenna in an antenna system impossible. However by measuring the field radiated by the antenna fed by one its ports and by using the superposition principle, it is

possible to approximate the total radiated field. For a two port balanced antenna, its realised differential gain $G_{diff}(\theta,\varphi,\omega)$ can be calculated with Equation (2.14) [28].

$$G_{diff}(\theta,\varphi,\omega) = \frac{G_i(\theta,\varphi,\omega)}{2}\frac{(1-|S_{11}-S_{21}|^2)}{(1-|S_{11}|^2-|S_{21}|^2)}\frac{\left(\left|\vec{E}_{1\theta}(\theta,\varphi,\omega)-\vec{E}_{2\theta}(\theta,\varphi,\omega)\right|^2+\left|\vec{E}_{1\varphi}(\theta,\varphi,\omega)-\vec{E}_{2\varphi}(\theta,\varphi,\omega)\right|^2\right)}{\left(\left|\vec{E}_{i\theta}(\theta,\varphi,\omega)\right|^2+\left|\vec{E}_{i\varphi}(\theta,\varphi,\omega)\right|^2\right)} \quad (2.14)$$

i= port1, port2

where $G_i(\theta,\varphi,\omega)$ in Equation (2.15) represents the realised gain of the antenna with its ports fed individually and is expressed as follows

$$G_i(\theta,\varphi,\omega) = \frac{2\pi r^2}{Z_0}\frac{\left(\left|\vec{E}_{i\theta}(\theta,\varphi,\omega)\right|^2+\left|\vec{E}_{i\varphi}(\theta,\varphi,\omega)\right|^2\right)}{P_i} \quad (2.15)$$

with r being the distance from the observation point to the antenna, Z_0 is the free space impedance which equal to $120\pi\ \Omega$.

2.1.6. Phase Centre

The phase centre is defined as a point where the variation of the phase in space is constant. From this point the radiated fields have spherical waves, meaning that fields measured along the surface of sphere, where its centre is the phase centre, should have the same phase. For instance the focal point of parabolic antenna must be at the phase centre in order to receive equiphase signals [29]. Deviation of the feed from phase centre will lead to phase errors reducing the gain of the antenna. Since the phase centre varies with frequency and because of the wide frequency range of UWB radio systems, it can be used to characterise the dispersive characteristics of UWB antennas although it is not straightforward to measure it. For best impulse performance the phase centre of antenna should remain stationary across the frequency range.

2.1.7. Transmission Coefficient, Transfer Function and Group Delay

The transmission coefficient defines spectrally the ratio of the amplitude of an incident complex waveform to the amplitude of the original excitation signal. For a system composed of two antennas, the transmission coefficient is often called the S_{21} and characterises spatially the dispersion existing in the communication channel (see Figure 2-3). From the Friis equation the relation between the channel, transmitting and receiving antennas in terms of the frequency is indicated in Equation (2.16) [30].

$$\frac{P_{RX}(\omega,\theta,\varphi)}{P_{TX}(\omega)} =$$

$$(1-|\Gamma_{TX}(\omega)|^2)(1-|\Gamma_{RX}(\omega)|^2)G_{TX}(\omega,\theta,\varphi)G_{RX}(\omega,\theta,\varphi)\left(\frac{c}{4\pi\omega R}\right)^2 \qquad (2.16)$$

$$\frac{P_{RX}(\omega,\theta,\varphi)}{P_{TX}(\omega)} = S_{21}(\omega,\theta,\varphi)$$

Where $P_{RX}(\omega,\theta,\varphi)$ is the power measured at the output of the receiving antenna, $P_{TX}(\omega)$ is the power transmitted at the transmitting antenna port, $\Gamma_{RX}(\omega)$ and $\Gamma_{TX}(\omega)$ are the input reflection coefficient of the receiving and transmitting antenna respectively, $G_{RX}(\omega,\theta,\varphi)$ and $G_{TX}(\omega,\theta,\varphi)$ are the gain of the receiving and transmitting antenna respectively and R is the distance separating both antennas. Consequently this metric contains the dispersive characteristics of the antennas and the channel which make it unsuitable to directly and accurately measure the Antenna Under Test (AUT) dispersion performance.

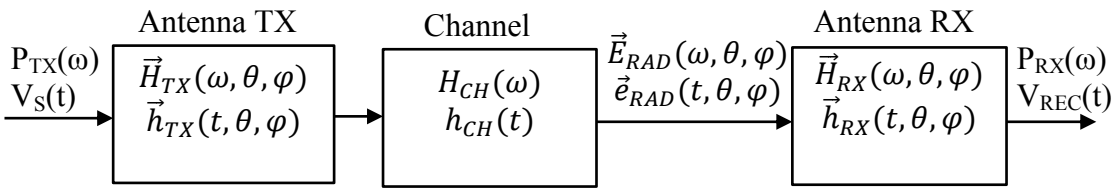

Figure 2-3: Block diagram representation of two port antenna system

To characterise the dispersion of an antenna both the transfer function magnitude and phase must be analysed. The transfer function of an antenna indicates the spectral response of an antenna relative to an excitation or incident signal. Hence to radiate or receive a signal with minimum dispersion at a particular angle in the space, an antenna shall exhibit a quasi-constant transfer function magnitude and a linear phase across the frequency range of interest. More importantly the transfer function group delay should remain constant. This metric is commonly used to characterise two port devices such as amplifiers and filters. It is defined as the negative derivative of the transfer function phase with respect to angular frequency as shown in Equation (2.18).

$$H(\omega,\theta,\varphi) = Gain(\omega,\theta,\varphi)e^{j\psi(\omega,\theta,\varphi)} \tag{2.17}$$

$$\tau(\omega,\theta,\varphi) = -\frac{d\psi(\omega,\theta,\varphi)}{d\omega} \tag{2.18}$$

Although this descriptor can provide a good estimation of the total dispersion, it does not provide a precise quantification of the distortion of the signal. This can be improved by using a statistical approach. Using the arithmetic mean and standard deviation of the group delay it becomes possible to compare antennas with each other. The group delay statistical mean $\overline{\tau(\theta,\varphi)}$ and standard deviation $\sigma_\tau(\theta,\varphi)$ are defined as follows [31]:

$$\overline{\tau(\theta,\varphi)} = \frac{1}{f_H - f_L}\int_{f_L}^{f_H} \tau(\omega,\theta,\varphi)d\omega \tag{2.19}$$

$$\sigma_\tau(\theta,\varphi) = \sqrt{\frac{1}{f_H - f_L}\int_{f_L}^{f_H} \left(\tau(\omega,\theta,\varphi) - \tau(\theta,\varphi)\right)^2 d\omega} \tag{2.20}$$

where f_L and f_H are respectively the lowest and highest frequency in the band of interest.

2.2. Time-domain Characterisation

2.2.1. Transmission Mode

Figure 2-4 represents a model of an antenna operating in transmitting mode. In free space, the farfield electric field $\vec{e}_{RAD}(t,\theta,\varphi)$ emanating from the antenna at a distance r_{TX} and direction (θ,φ), is dependent on the transmitting antenna impulse response $\vec{h}_{TX}(t,\theta,\varphi)$ and the input voltage at the antenna terminals $V_S(t)$. The impulse responses of antenna are defined as the antenna transient responses to an impulse input signal, while a transient response can be defined to the response of system, or device, to a change from the steady state response. The electric radiated field can be found using Equation (2.21) [32] [33]

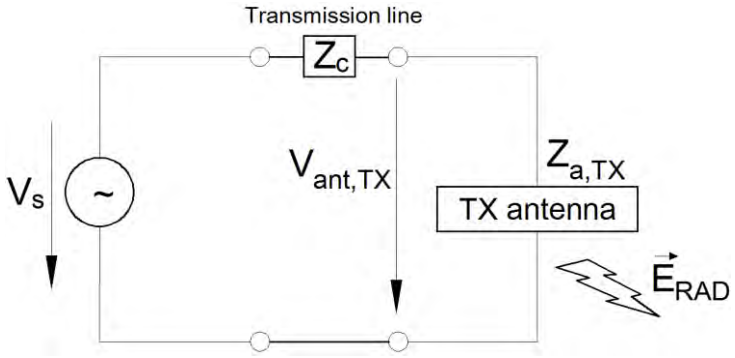

Figure 2-4: Block diagram of transmitting antenna;

$$\vec{e}_{RAD}(t,\theta,\varphi)=\frac{1}{2\pi r_{TX} c f_g}\vec{h}_{TX}(t,\theta,\varphi)*\frac{dV_{ant,TX}(t)}{dt}*\delta(t-t_{d,TX})$$

$$\text{with} \quad f_g=\frac{Z_{a,TX}}{Z_0}\frac{dV_{ant,TX}(t)}{dt}=\tau_{TX}\frac{dV_S(t)}{dt} \tag{2.21}$$

$$\text{and} \quad \tau_{TX}=\frac{2Z_{a,TX}}{Z_{a,TX}+Z_c}\,;\, Z_c=50\Omega$$

where the term $*$ stand for convolution, $V_s(t)$ is the input voltage at the antenna terminal, $V_{ant,TX}(t)$ is the voltage excited at the antenna feed, c is the speed of light, $Z_{a,TX}$ is the antenna impedance, f_g is the ratio between the antenna impedance and free space impedance Z_0 equal to 120π Ω and τ_{TX} is the voltage transmission coefficient from the transmission line to the antenna. The term $\vec{h}_{TX}(t,\theta,\varphi)$ represents the transmitting antenna impulse response when the antenna is terminated by a real impedance equal to the impedance of the feed structure. The convolution with the dirac-function $\delta(t-t_{d,TX})$ introduces a total delay $t_{d,TX}$ corresponding to the propagation time between the input reference plane and the observation point of the radiated field. By combining the above equations, Equation (2.21) can be simplified into Equation (2.22) [33]

$$\vec{e}_{RAD}(t,\theta,\varphi)=\frac{\tau_{TX}}{2\pi r_{TX} c f_g}\vec{h}_{TX}(t,\theta,\varphi)*\frac{dV_S(t)}{dt}*\delta(t-t_{d,TX}) \tag{2.22}$$

In reality $Z_{a,TX}$ is a function of frequency so that τ_{TX} and f_g are not constant. One way to solve the problem is to normalise the voltages and field to the local characteristic impedance (transmission line or medium). Starting with Equation (2.22) the normalised radiated field is given by Equation (2.23) [32].

$$\frac{\vec{e}_{RAD}(t,\theta,\varphi)}{\sqrt{Z_0}} = \frac{1}{2\pi r_{TX} c}\left[\sqrt{\frac{Z_c}{Z_{a,TX}}}\tau_{TX}\right]\frac{\vec{h}_{TX}(t,\theta,\varphi)}{\sqrt{f_g}} * \frac{1}{\sqrt{Z_c}}\frac{dV_S(t)}{dt} \tag{2.23}$$

$$* \delta(t - t_{d,TX})$$

Then Equation (2.23) can be simplified into Equation (2.24) [32] [33].

$$\frac{\vec{e}_{RAD}(t,\theta,\varphi)}{\sqrt{Z_0}} = \frac{1}{2\pi r_{TX} c}\vec{h}_{N,TX}(t,\theta,\varphi) * \frac{1}{\sqrt{Z_c}}\frac{dV_S(t)}{dt} * \delta(t - t_{d,TX})$$

$$\text{with} \quad \tau_{p,TX} = \tau_{TX}\sqrt{\frac{Z_c}{Z_{a,TX}}} \tag{2.24}$$

$$\text{and} \quad \vec{h}_{N,TX}(t,\theta,\varphi) = \frac{\tau_{p,TX}}{\sqrt{f_g}}\vec{h}_{TX}(t,\theta,\varphi)$$

The term $\tau_{p,TX}$ describes the incident power on the transmission line as the square root of the power launched onto the antenna. The normalised impulse response $\vec{h}_{N,TX}(t,\theta,\varphi)$ included the antenna impulse response $\vec{h}_{TX}(t,\theta,\varphi)$and the losses due to the mismatch between the antenna and the feeding network. It is seen that the radiated field is completely described by Equation (2.24). Applying the Fourier transform to Equation (2.24) gives the radiated field in frequency domain as shown in Equation (2.25).

$$\frac{\vec{E}_{RAD}(\omega,\theta,\varphi)}{\sqrt{Z_0}} = \frac{j\omega}{2\pi r_{TX} c} e^{-j\omega\frac{r_{TX}}{c}}\ \vec{H}_{N,TX}(\omega,\theta,\varphi)\frac{V_S(\omega)}{\sqrt{Z_c}} \tag{2.25}$$

In this equation, the ratio $\frac{r_{TX}}{c}$ represents the time delay $t_{d,TX}$ of the dirac-function, and $\vec{H}_{N,TX}(\omega,\theta,\varphi)$ represents the antenna normalised transfer function. As seen on Equation (2.25), the term $j\omega$ can be placed anywhere meaning that the derivation d/dt and the convolution $*$ can be exchanged [34], leading to the following equation.

$$\frac{\vec{e}_{RAD}(t,\theta,\varphi)}{\sqrt{Z_0}} = \frac{1}{2\pi r_{TX} c}\delta(t - t_{d,TX}) * \frac{d\vec{h}_{N,TX}(t,\theta,\varphi)}{dt} * \frac{V_S(t)}{\sqrt{Z_c}} \tag{2.26}$$

2.2.2. Reception Model

Figure 2-5 represents a model of an antenna operating in receiving mode. When the receiving antenna is illuminated with a uniform plane-wave incident E-field $\vec{e}_{INC}(t,\theta,\varphi)$ coming from the direction (θ,φ) and evaluated at the antenna phase centre, the voltage received at the load (i.e. an oscilloscope) $V_{REC}(t,\theta,\varphi)$ can be found using Equation (2.27) [32].

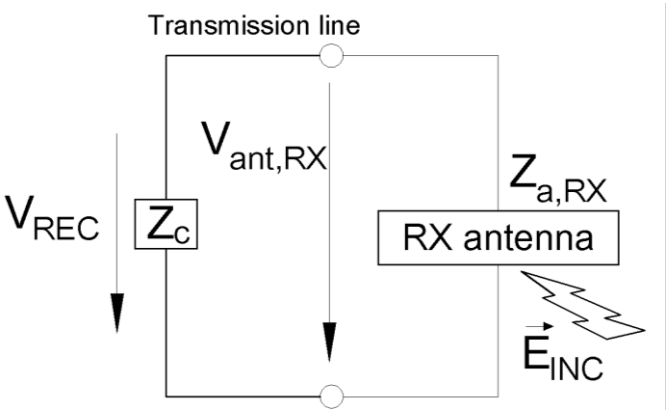

Figure 2-5: Block diagram of receiving antenna

$$V_{REC}(t,\theta,\varphi) = \vec{h}_{RX}(t,\theta,\varphi) * \vec{e}_{INC}(t,\theta,\varphi) * \tau_{RX} * \delta(t - t_{d,RX})$$
$$\text{With } \tau_{RX} = \frac{2Z_c}{Z_c + Z_{a,RX}} \text{ and } Z_C = 50\Omega \tag{2.27}$$

where $\vec{h}_{RX}(t,\theta,\varphi)$ is the impulse response of the receiving antenna, τ_{RX} is the voltage transmission coefficient from the antenna to the load Z_c, $Z_{a,RX}$ represents the antenna impedance and $\delta(t - t_{d,RX})$ represents the propagation time between the phase centre of the antenna and the reference plane where $V_{REC}(t,\theta,\varphi)$ is measured. Since τ_{RX} is not constant in frequency, it is necessary to normalise Equation (2.27) using the same method shown in Equation (2.23) and (2.24) [32] [33].

$$\frac{V_{REC}(t,\theta,\varphi)}{\sqrt{Z_c}} = \left[\sqrt{\frac{Z_{a,RX}}{Z_c}}\tau_{RX}\right]\frac{\vec{h}_{RX}(t,\theta,\varphi)}{\sqrt{f_g}} * \frac{\vec{e}_{INC}(t,\theta,\varphi)}{\sqrt{Z_0}} \quad (2.28)$$

$$* \delta(t - t_{d,RX})$$

Equation (2.28) described the normalised received voltage $V_{REC}(t,\theta,\varphi)$ at the load Z_c. Using the same methodology used for the simplification of Equation (2.23), Equation (2.28) can be simplified into Equation (2.29) [32].

$$\frac{V_{REC}(t,\theta,\varphi)}{\sqrt{Z_c}} = \vec{h}_{N,RX}(t,\theta,\varphi) * \frac{\vec{e}_{INC}(t,\theta,\varphi)}{\sqrt{Z_0}} * \delta(t - t_{d,RX})$$

$$\text{with} \quad \vec{h}_{N,RX}(t,\theta,\varphi) = \frac{\tau_{p,RX}}{\sqrt{f_g}}\vec{h}_{RX}(t,\theta,\varphi) \quad (2.29)$$

$$\text{and} \quad \tau_{p,RX} = \tau_{RX}\sqrt{\frac{Z_{a,RX}}{Z_c}}$$

In Equation (2.29), it is seen that the receiving antenna impulse response and the mismatch losses of the receive antenna are contained in the antenna normalised impulse response $\vec{h}_{N,RX}(t,\theta,\varphi)$. Applying the Fourier transform to Equation (2.29) gives the voltage received at the load in the frequency domain as shown in Equation (2.30)

$$\frac{V_{REC}(\omega,\theta,\varphi)}{\sqrt{Z_c}} = \vec{H}_{N,RX}(\omega,\theta,\varphi)\frac{\vec{E}_{INC}(\omega,\theta,\varphi)}{\sqrt{Z_0}}e^{-j\omega\frac{r_{RX}}{c}} \quad (2.30)$$

where $\vec{H}_{N,RX}(\omega,\theta,\varphi)$ is the normalised transfer function of the receiving antenna while the ratio $\frac{r_{RX}}{c}$ represents the propagation time delay $t_{d,RX}$ of the dirac-function $\delta(t - t_{d,RX})$ with r_{RX}being the distance from the receiving antenna phase centre and the reference plane where $V_{REC}(\omega,\theta,\varphi)$ is measured and the term $e^{-j\omega\frac{r_{RX}}{c}}$ represents the time delay Dirac function in the frequency domain.

In the case of an antenna system comprising a pair of identical antennas and by analysing Equation (2.26) and (2.29), it is seen that the normalised impulse response of antenna in transmitting mode is proportional to the derivative of the impulse response of the same antenna operating in receiving mode [35], as shown in Equation (2.31) and (2.32).

$$\vec{h}_{N,TX}(t,\theta,\varphi)=\frac{1}{2\pi rc}\frac{d\vec{h}_{N,RX}(t,\theta,\varphi)}{dt} \tag{2.31}$$

$$\vec{H}_{N,TX}(\omega,\theta,\varphi)=\frac{j\omega}{2\pi rc}\vec{H}_{N,RX}(\omega,\theta,\varphi) \tag{2.32}$$

2.3. Time-domain Descriptors

The performances of impulse based systems rely on the quality of a signal relative to a reference signal. Hence for an antenna designer, it is important to quantify the level of distortion of the radiated signal in the time-domain. Although it is possible to obtain time-domain results, such as radiated or received signal, using the convolution between the reference signal and the inverse Fourier transform of the transfer function, transient results could be impaired if the frequency span and the windowing function used in the frequency-domain based measurement system (i.e. vector network analyser) is not taken into consideration. Therefore, it is desirable to use dedicated time-domain measurement systems such as waveform generators and oscilloscopes where the degree of dispersion existing in the measured signal can be quantified using several time descriptors [36]. In this thesis only the fidelity factor is used to describe the time-domain performance of antennas.

2.3.1. Fidelity Factor

The fidelity factor (FF) can be used to quantify the dispersion of a reference signal caused by the antenna. The fidelity factor is based on the principle of the cross-correlation between two signals, the reference signal (excitation or incident signal), and the radiated or received signal, and calculates the similarities existing between these signals. The general equation of the fidelity factor is defined as follows:

$$\mathrm{FF}=\max\left|\frac{\int_{-\infty}^{\infty} x_1(t)x_2(t+t_d)dt}{\sqrt{\int_{-\infty}^{\infty}|x_1(t)|^2\,dt}\sqrt{\int_{-\infty}^{\infty}|x_2(t)|^2\,dt}}\right| \tag{2.33}$$

where $x_1(t)$ and $x_2(t)$ are the signals being compared and t_d indicates a time delay. Since the antenna impulse response changes when the antenna is operating in transmitting or receiving mode, the fidelity factor for these two operating modes will be different and can be defined as indicated in Equation (2.34) and Equation (2.35)

$$FF_{RAD}=\max\left|\frac{\int_{-\infty}^{\infty} V_S(t)\vec{e}_{RAD}(t+t_d,\theta,\varphi)dt}{\sqrt{\int_{-\infty}^{\infty}|V_S(t)|^2\,dt}\sqrt{\int_{-\infty}^{\infty}|\vec{e}_{RAD}(t,\theta,\varphi)|^2\,dt}}\right| \tag{2.34}$$

$$FF_{REC}=\max\left|\frac{\int_{-\infty}^{\infty} \vec{e}_{INC}(t,\theta,\varphi)V_{REC}(t+t_d,\theta,\varphi)dt}{\sqrt{\int_{-\infty}^{\infty}|\vec{e}_{INC}(t,\theta,\varphi)|^2\,dt}\sqrt{\int_{-\infty}^{\infty}|V_{REC}(t,\theta,\varphi)|^2\,dt}}\right| \tag{2.35}$$

where $\vec{e}_{RAD}(t,\theta,\varphi)$ and $\vec{e}_{INC}(t,\theta,\varphi)$ are the radiated and incident far electric fields, respectively. As the impulse response of an antenna is not constant in space, FF_{RAD} is dependent of the radiated electric field observation point while FF_{REC} depends of the angle of arrival of the incident E-field. In this thesis the simulated and measured

FF is represented in an azimuth and elevation plane polar plot although it is possible to create a 3D fidelity factor pattern.

2.4. Measurement Setup

In order to provide reliable, repeatable and accurate results, measurements were made in a partially anechoic chamber. Absorber materials were placed in strategic positions in order to minimise signal reflections that could otherwise impair the measurement results. Horn antennas were used as referenced antennas, where their S_{11} and gain were stored in a database. The antenna under test were adjusted and rotated on a fully controlled turn table. The AUT were centred on the turn table making the radiation pattern only dependent on the angular parameters (θ,φ).

2.4.1. Frequency-domain Measurement Setup

In order to have repeatable results, a customized program was interfaced with a two port VNA Rohde & Schwarz ZVB24 while controlling the turn table. The engineer is guided through a step by step procedure where initialisation, setup and calibration are required. It allows the measurement of the co-polar and cross-polar components of the E-plane and H-plane. The initial measurement results are then post processed using the Friis equation [37] in order to determine the gain of the AUT and stored in an Excel file for post processing. The frequency measurement setup is shown in Figure 2-6 and Figure 2-7.

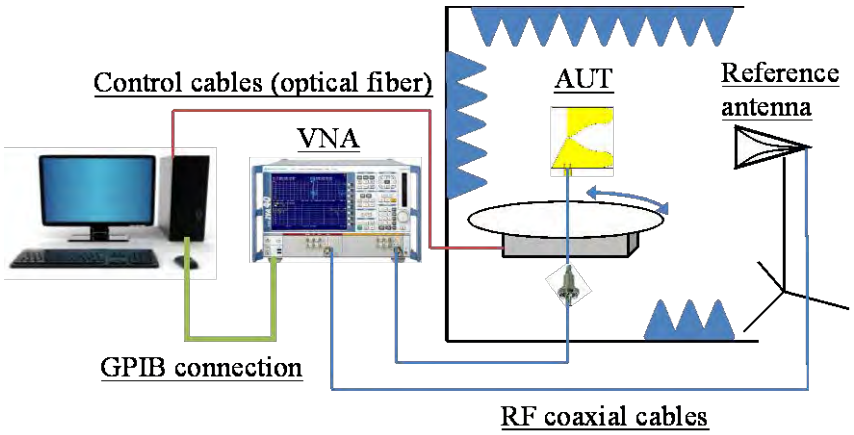

Figure 2-6: Frequency-domain measurement setup

Figure 2-7: Photo of the frequency-domain measurement setup

2.4.2. Time-domain Measurement Setup

An AGILENT DS081204A real time oscilloscope was used to measure signals in the time-domain, while a Step Recovery Diode (SRD) based generator or an Arbitrary Waveform Generator TEKTRONIX AWG 7122C were used to generate impulses at a pulse rate of 80 MHz and 24 MHz respectively. The AUT was positioned on the turn table to allow an accurate angular measurement and although the measurements were made in a multipath environment, the small time span of the

oscilloscope (2ns or 5ns) acts as time gating windows, supressing the possible multipath signals reflected back at the antenna under test.

Unlike VNAs, this high performance real time oscilloscope does not provide a reliable fully automatic measurement, especially when the peak to peak amplitude of the signal at the oscilloscope port does not exceed 10mV. Below this value the noise floor of the scope became significant and the acquisition trigger has to be adjusted, manually, with great care to capture a stable signal. Hence for the sake of measurement repeatability and accuracy a MATLAB script with an integrated graphical user interface was written. The script interfaced a computer equipped with MATLAB with the oscilloscope and controls it via a TCP/IP connection. This code scans for the signal and calibrates the trigger level and the amplitude scale depending on the signal stability and the peak-to-peak voltage of the signal V_{PP}, while calculating the FF between the received and reference signals. The script is also able to calibrate the scope to a reference plane, making the measurement of the radiated E-field possible. The MATLAB script is available upon request at the AHFR centre. The time-domain measurement setups are illustrated on Figure 2-8 and Figure 2-9. Finally, the code was thoroughly tested, debugged, and optimised for repeatability, robustness, and measurement accuracy, as illustrated in the flow chart shown in Figure 2-10.

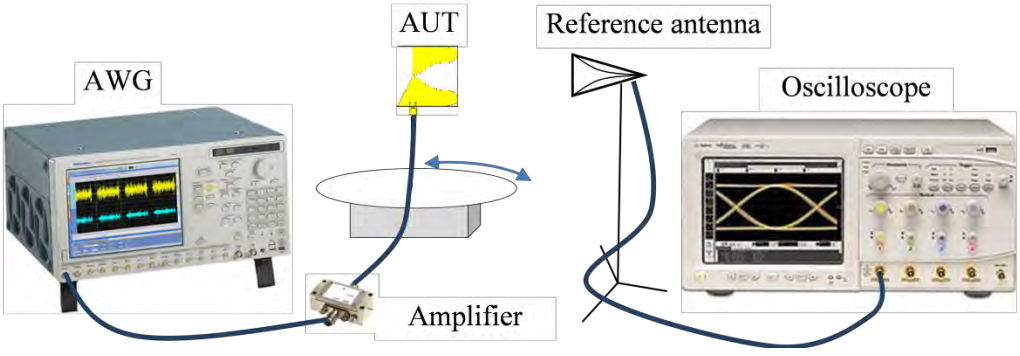

Figure 2-8: Time-domain measurement setup

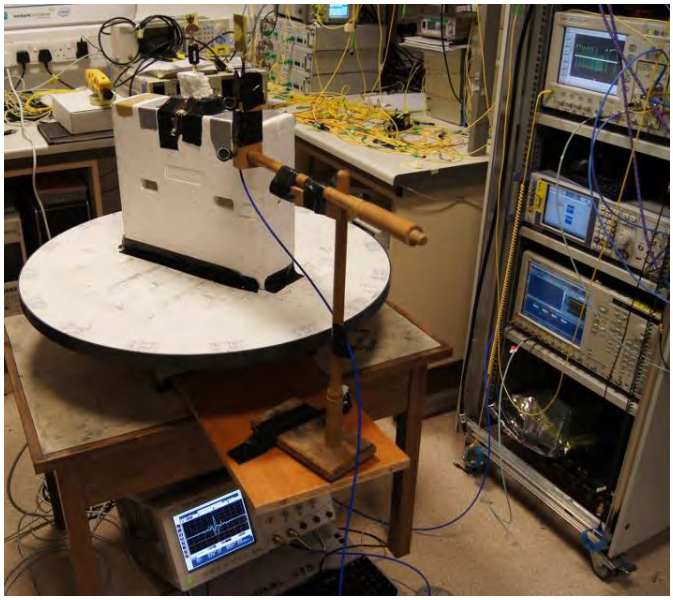

Figure 2-9: Photo of the time-domain measurement setup

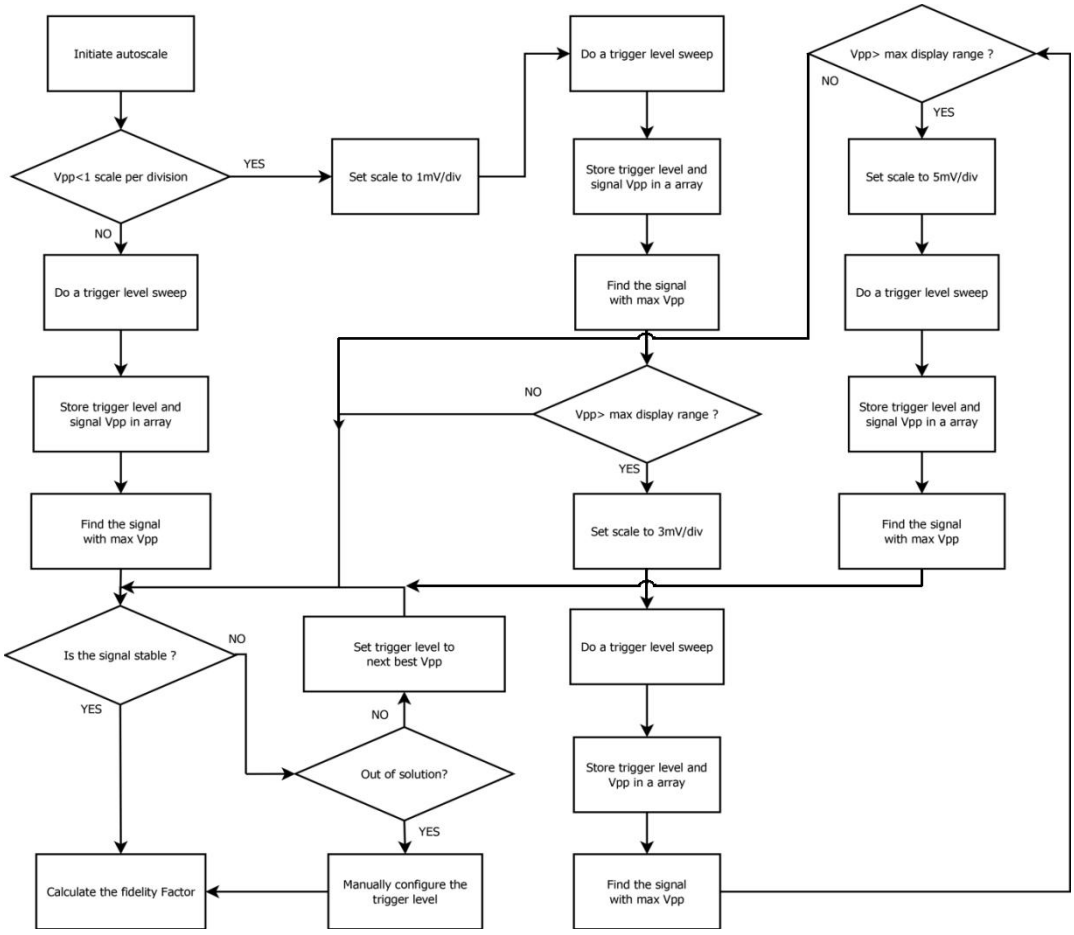

Figure 2-10: Flow chart of the automated MATLAB script

2.4.3. Coordinate Systems

In this thesis the radiation pattern is characterised in the farfield, using two dimensional plane cuts. The elevation (ZY plane) and azimuth plane (XY plane) represents the E-plane and H-plane vectors respectively as seen in Figure 2-11. Because the AUT will be tested over a broad frequency range, a contour plot is preferred to represent the radiation pattern in the plane of interest versus the frequency, simplifying the analysis of the gain.

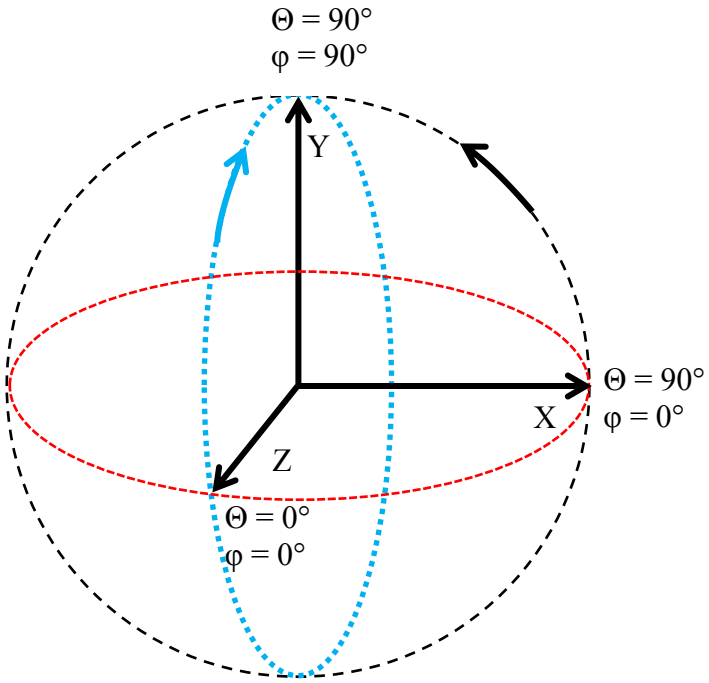

Figure 2-11: Coordinate systems used for the radiation pattern and fidelity factor

CHAPTER 3: UWB SIGNALS

UWB impulse radio signals are an integral part of RLTS and radar systems. By post processing the scattered signal and comparing against a reference signal, these systems are able to track and/or characterise objects or persons. The choice of the signal is crucial for the UWB system application, since the system precision range is inversely proportional to the signal bandwidth.

The first part of this chapter will focus on the definition of UWB signals with regard to the IEEE 802.15.4 standard and the power restrictions. The second section will present several types of signals that could potentially be used for UWB systems. Each are characterised in both frequency- and time-domain and are assessed in terms of the regulatory requirements defined in the standard. Furthermore an optimal UWB signal will also be presented and discussed. The third and fourth sections describe the basic principles of signal transmission and reception from antennas in terms of antenna impulse response.

3.1. UWB Signal Definitions

UWB signal emission masks are shaped by different regulatory bodies. According to the FCC, the signal bandwidth must be contained within the UWB frequency band (3.1 GHz to 10.6 GHz) while respecting the indoor and outdoor UWB power spectrum density mask. It should be noted that the outdoor UWB communication is reserved for handheld devices which do not used fixed infrastructure. Figure 3-1 gives a quick overview of the different limits set by the FCC regulation. It is seen that the signal 10 dB bandwidth is strongly dependent on

the signal spectrum shape especially for signals having a centre frequency f_c close to the UWB mask edge. The transmitted spectrum must also comply with the UWB physical layer (UWB PHY) transmit Power Spectrum Density (PSD) mask set by the IEEE 802.15.4 standard [8].

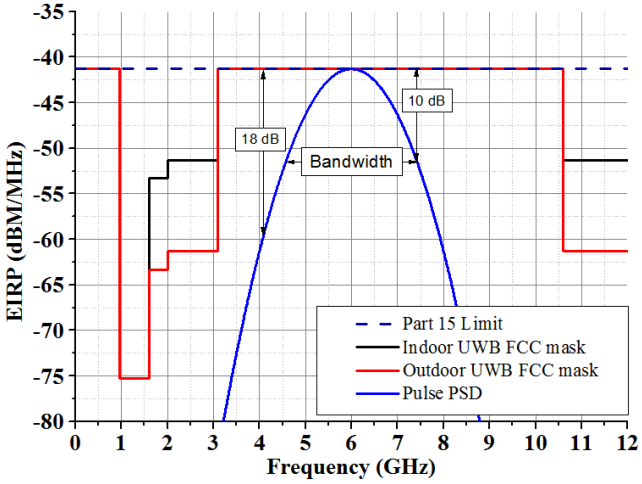

Figure 3-1: UWB signal design points

According to this standard the transmitted signal spectrum must comply with the –10 dB and –18 dB bandwidths relative to the maximum spectrum peak of the signal, as described in Equation (3.1) and Equation (3.2):

$$BW_{10dBr} = \frac{0.65}{T_p} < |f - f_c| < \frac{0.8}{T_p} \tag{3.1}$$

$$BW_{18dBr} = |f - f_c| > \frac{0.8}{T_p} \tag{3.2}$$

where T_p is the pulse duration, f is the lower or upper edge frequency and f_c is the centre frequency. Figure 3-2 shows the IEEE 802.15.4 transmit PSD mask for a Gaussian signal with pulse duration T_p =1.3 ns.

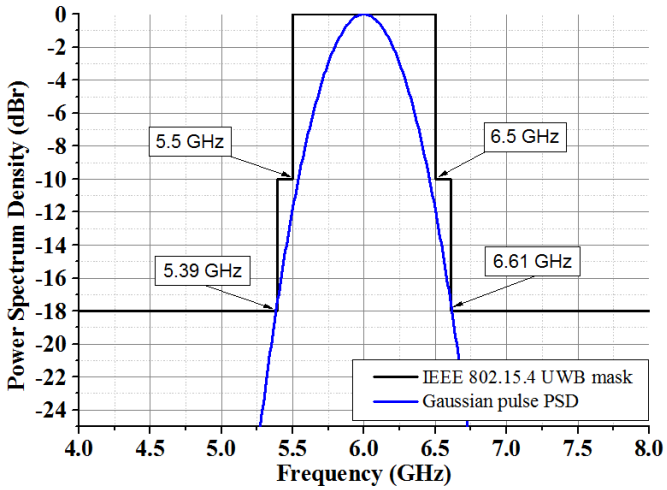

Figure 3-2: IEEE 802.15.4 transmit mask for a modulated Gaussian signal (T_p=1.3 ns)

Also a rectangular pulse with a pulse duration T_p =1.5 ns is shown in Figure 3-3. It demonstrates that due to the first spectral side lobe, the rectangular pulse fails to comply with the IEEE 802.15.4 mask. Therefore choice of pulse type is an important consideration for compliance to both regulations.

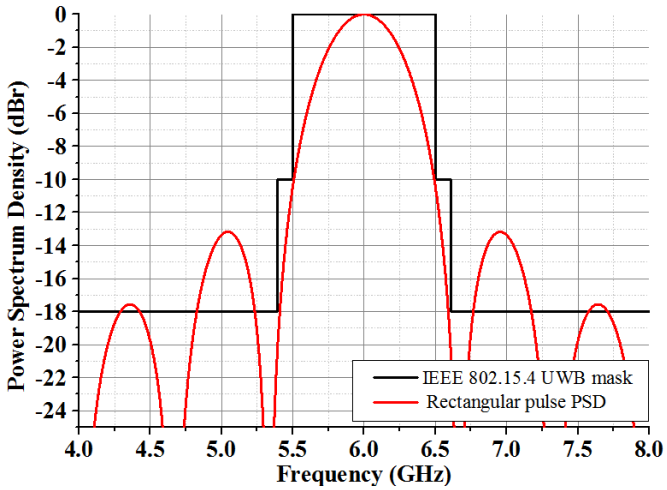

Figure 3-3: IEEE 802.15.4 transmit mask for a modulated rectangular pulse (T_p=1.5 ns)

3.2. Type of UWB Signal

According to the FCC an UWB signal shall have a minimum bandwidth of 500 MHz. To generate such bandwidth, signals with sharp transitions and extremely narrow pulses are used. Naturally, each type of signal exhibits different characteristics in the time and frequency-domain depending on signal amplitude transition time and temporal main-to-side lobe ratio resulting in a spectrum density that can have a significant impact on system performance.

3.2.1. Rectangular Pulse

The simplest pulse to represent is the rectangular pulse shown on Figure 3-4. This pulse is impossible to generate because of the sharp edges, but has time and spectral properties of theoretical interest to be studied.

The time-domain equation for the rectangular impulse is given in Equation (3.3). In Figure 3-5, it is seen that the frequency spectrum, computed via a Fast Fourier Transform (FFT), contains significant side lobes. Typically the first side lobe of the rectangular pulse is 13 dB below the peak energy, and can exceed the regulatory levels in some cases.

$$Rect(t) = \begin{cases} 1 & for\ t_0 \leq t \leq T_p \\ 0 & elsewhere \end{cases} \tag{3.3}$$

Also it is known that the sharper the rise and fall of a time-domain signal, the more energy the spectral side lobe will contain [38]. Hence by smoothing the rise and fall edge of a time signal it is possible to reduce the level of energy contained in the spectral side lobes

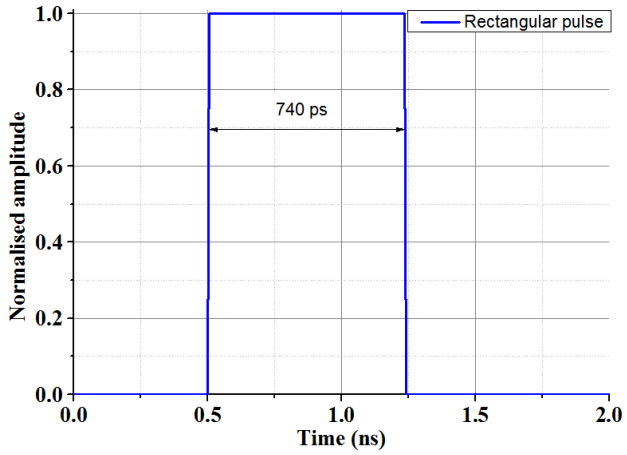

Figure 3-4: Time-domain representation of a rectangular pulse

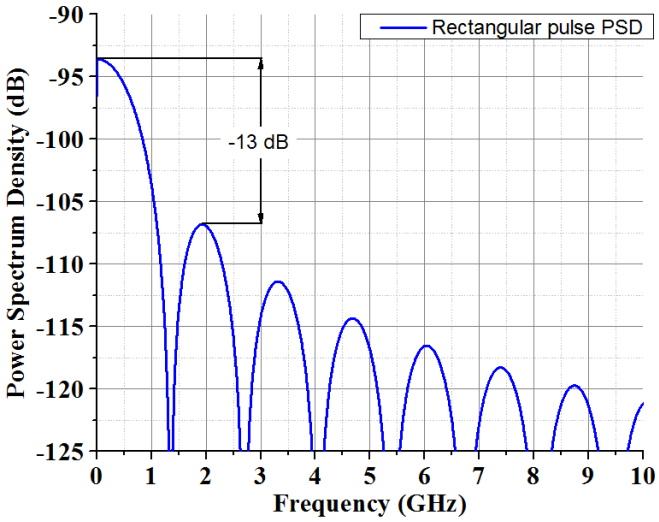

Figure 3-5: Frequency-domain representation of a rectangular pulse

3.2.2. Gaussian Pulse

The Gaussian pulse is a well-known wavelet that has been used extensively by researchers for use as excitation signals for antenna design [30] [39] [40]. This impulse, shown in Figure 3-6, has a very smooth amplitude transition in the time-domain and is described by the following equation.

$$Gauss(t) = \exp\left(-\frac{1}{2}\left(\frac{t}{(\tau)}\right)^2\right) \tag{3.4}$$

with τ being the pulse width parameter defined in Equation (3.5).

$$\tau = \frac{1}{2\pi f_{bw}\sqrt{log_{10}(2.71828)}} \tag{3.5}$$

where f_{bw} is the required 10 dB bandwidth (Hz). It is seen, in Figure 3-7, that the Gaussian pulse has no spectral lobes, which indicates that all the energy is contained in the main lobe.

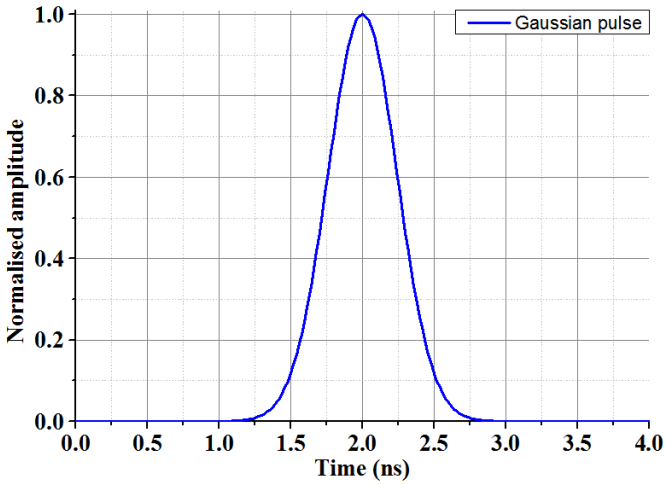

Figure 3-6: Time-domain representation of a Gaussian pulse

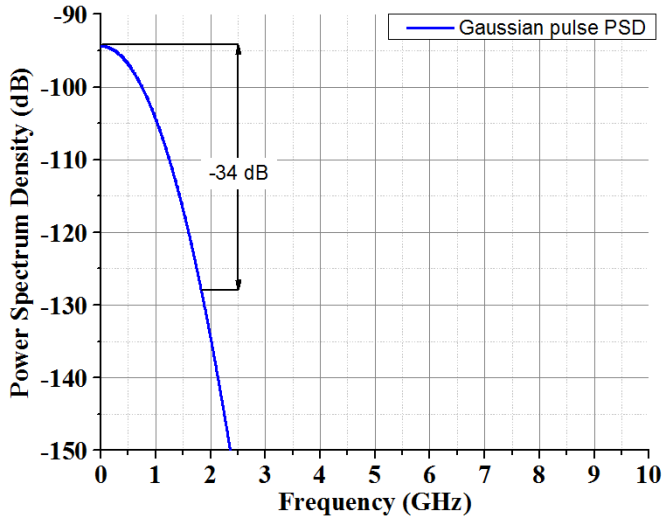

Figure 3-7: Frequency-domain representation of a Gaussian pulse

3.2.2.1. FCC UWB Compliant Gaussian Pulse

One way to comply with the FCC UWB regulation is to use the Gaussian derivatives. Figure 3-8 represents different Gaussian derivatives at different orders of derivation. Each has been tuned for the best 10 dB bandwidth and best compliance

with the FCC UWB indoor regulation. It is seen in Figure 3-9, that the fourth and fifth order derivative spectra lie within the FCC UWB indoor mask but they do not fill completely the 7.5 GHz 10 dB bandwidth available. However none of them are suitable for the FCC UWB outdoor EIRP mask (red curve).

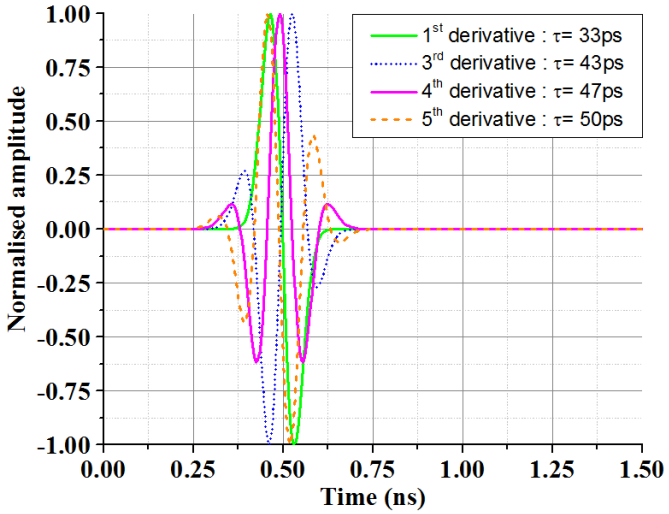

Figure 3-8: Time-domain representation of Gaussian pulse derivatives

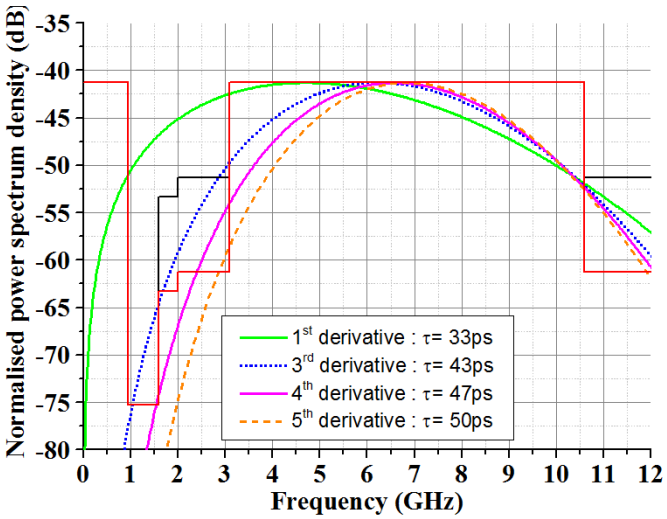

Figure 3-9: Frequency-domain representation of Gaussian pulse derivatives

Another solution to comply with the energy levels addressed by the different regulatory bodies is to multiply the baseband Gaussian impulse with a carrier as shown in Equation (3.6).

$$Gauss_m(t) = Gauss(t)\cos(2\pi f_c t) \tag{3.6}$$

where f_c is the frequency of the signal carrier. Figure 3-10 and Figure 3-11 show two modulated Gaussian pulses having spectral energy levels compliant with the FCC UWB indoor (τ = 85 ps) and outdoor mask (τ = 91 ps). This method allows the baseband signal to be frequency shifted to the operating centre frequency, while the signal bandwidth can be adjusted independently to fit the mask requirements.

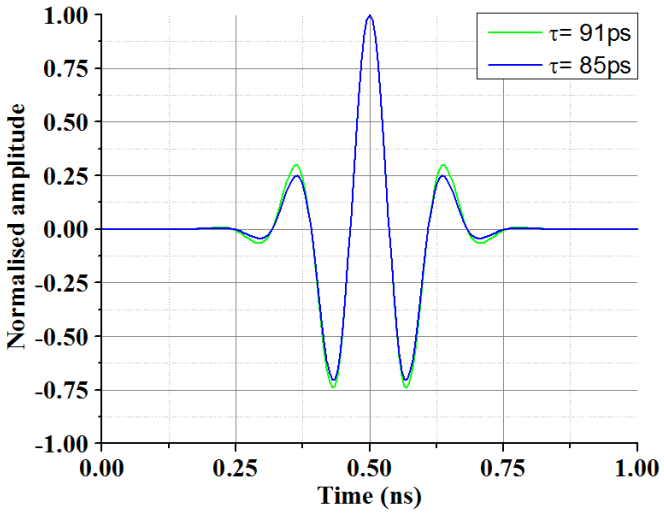

Figure 3-10: Gaussian pulse modulated at 6.85 GHz

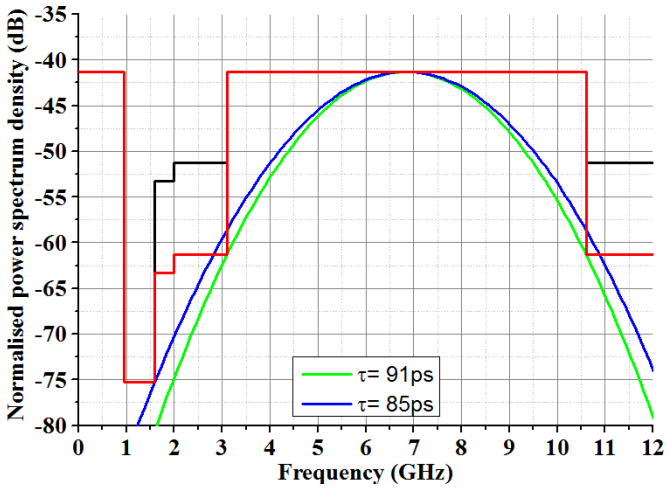

Figure 3-11: Power spectrum density of Gaussian pulse modulated at 6.85 GHz

However, Figure 3-11 also indicates that this type of pulse does not have a constant energy level across the UWB frequency range, with a total emitted power of −6.22 dBm (τ = 85 ps) and −6.53 dBm (τ = 91 ps) compared with the theoretical maximum EIRP of −2.55 dBm (0.556 mW).

3.2.3. Square Root Raised Cosine Pulse

The square root raised cosine (SRRC) function is well known in the filter and telecommunications field. For communications applications, the SRRC filters are used at the transmitter and receiver side to reduce Inter Symbol Interference (ISI), satisfying the Nyquist criterion. The analytical form of the SRRC transient function is shown in Equation (3.7) [41].

$$F_{SRRC}(t) = \left[\frac{2\beta}{\pi\sqrt{T_s}} \frac{\cos\left[(1+\beta)\pi\frac{t}{T_s}\right] + \frac{\sin\left[(1-\beta)\pi\frac{t}{T_s}\right]}{4\beta\frac{t}{T_s}}}{\left[1-(4\beta\frac{t}{T_s})^2\right]} \right] \quad (3.7)$$

where t is the time, $T_S = 1/R_S$, R_S being the symbol rate (3 dB bandwidth) and β is the unitless roll-off factor. By tuning the symbol rate and the roll-off factor, it is possible to generate a signal having an evenly contoured power spectrum. Figure 3-12 and Figure 3-13 shows a SRRC signal with a symbol rate R_S of 4.7 GHz and its power spectrum density in term of β. It is seen that as roll-off value decreases toward zero, the energy level becomes more constant at the 3 dB bandwidth, in the UWB frequency range, at the expense of greater side lobes in both time and frequency-domain. Since the pulse has an infinite duration, increasing the time span of the signal will lead to an improved spectrum shape, especially when the roll-off factor tends to zero.

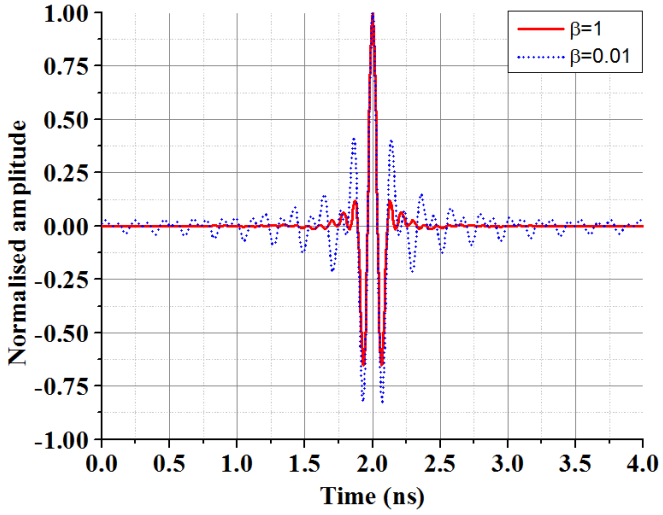

Figure 3-12: SRRC signal in terms of their roll-off factor

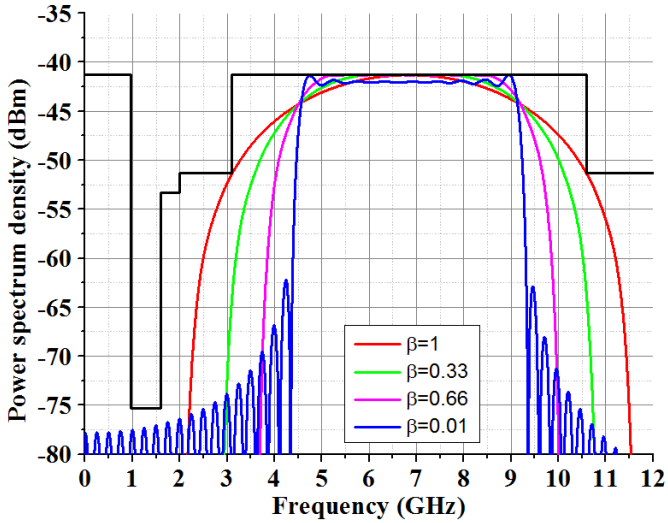

Figure 3-13: Spectral representation of SRRC signal in terms of their roll-off factor

This analysis of the SRRC pulse characteristics shows that an optimal pulse for the UWB mask is achievable. Figure 3-14 shows a modulated Gaussian pulse and a modulated SRRC pulse independently *of* wherever (roll-off factor of 0.1 and symbol rate of 7.1 GHz), both centred on 6.85 GHz. Figure 3-15 shows the respective PSD plots with the IEEE 802.15.4 UWB indoor spectrum mask. The analysis of Figure 3-14 and Figure 3-15, reveals that the modulated SRRC signal, with the parameters specified earlier, clearly has an optimal fit to the UWB indoor spectrum compared to the modulated Gaussian signal. Also the side lobes carry a low energy level, fulfilling the FCC UWB energy requirements, while the pulse conveys a power

of −2.86 dBm, in other words 93.1% of the theoretical maximum EIRP of −2.55 dBm (0.556 mW). Its improved bandwidth makes it an ideal excitation signal to characterise antennas in the time-domain as seen in Chapter 5.

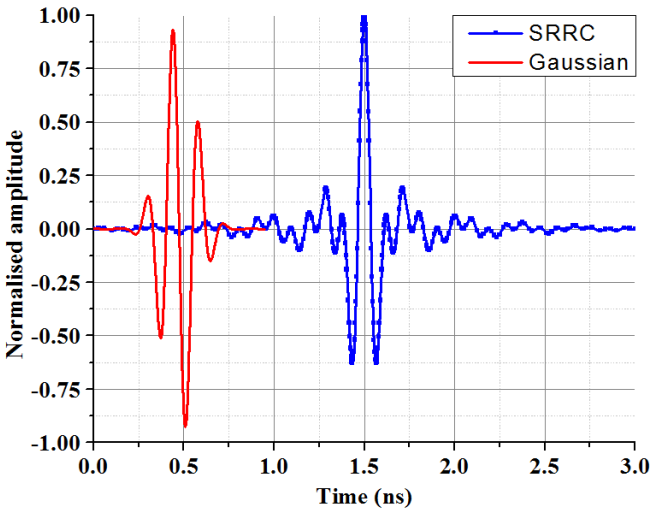

Figure 3-14: Modulated Gaussian and SRRC pulses

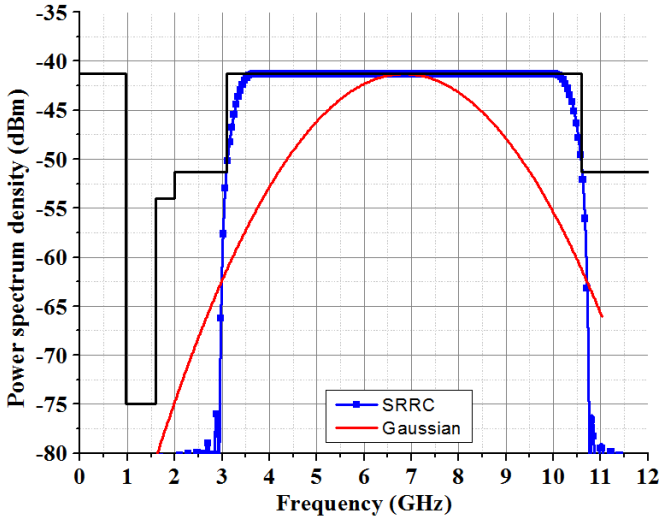

Figure 3-15: Power spectrum density of Gaussian and SRRC pulses with the IEEE 802.15.4 spectrum mask for indoor use.

3.2.4. Chirp Signal

The chirp signal is a signal commonly used in radar and in measurement hardware such as vector network analysers (VNA). Its main characteristic is a linear or exponential increase of frequency with time, as seen in Figure 3-16. In Figure 3-17, it can be seen that the spectrum is not constant over the UWB frequency

range and has ripples that do not comply with the UWB regulation. The latter problem can be solved by using filters to shape the spectrum in order to satisfy the spectral power constraint set by the different regulatory bodies.

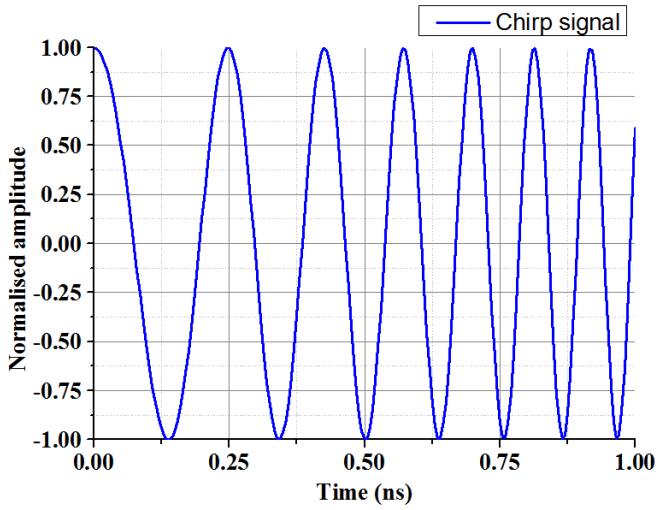

Figure 3-16: Chirp signal

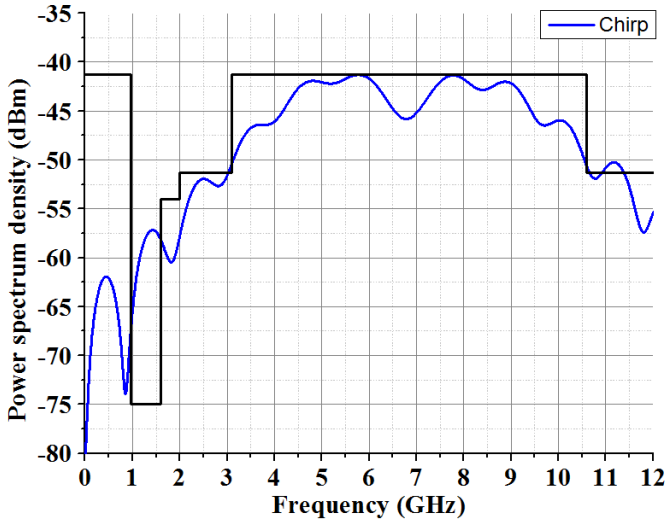

Figure 3-17: Power spectrum density of a chirp signal

3.2.5. Other UWB Pulses

A UWB spectrum can be generated by using sharp voltage transitions or extremely short pulses. These signals are relatively easy to generate but their spectral characteristics generally do not comply with the rules set by the regulatory bodies.

A step recovery diode (SRD) has the capability to create extremely sharp pulses. If a forward biased SRD diode is rapidly reverse-current biased and when its stored charges are depleted it will suddenly switch to its normal high reverse impedance, stopping the flow of reverse current, in a transition time taking less than a nanosecond. This fast transition then creates a pulse with wideband characteristics.

SRD diodes can be used as comb generators, generating a number of harmonics simultaneously that look like a *comb* on a spectrum analyser [42] [43], or as a pulse sharpener [44]. In this section the SRD diode are used for the latter application.

Figure 3-18 and Figure 3-19 shows a pulse generated by step recovery diode (SRD) GC082-361 from HEROTEK and its PSD respectively. It is seen that the SRD pulse has a 2.37 GHz 10 dB bandwidth but has a strong DC component. In order to attenuate the undesirable pulse spectral components, the pulse was filtered through a UWB band pass filter where the time and frequency-domain representations of the pulses are shown on Figure 3-18 and Figure 3-19. It is seen that the filtered signal has 4.28 GHz 10 dB bandwidth, however the power levels from 0 to 1.6 GHz do not satisfy the FCC UWB mask and thus make this signal unusable in commercial devices. One way to generate a pulse with a UWB compliant spectrum density is to use an SRD with a sharper transition time, generating a more wideband signal while the latter can be filtered through a single or cascaded raised cosine filter. Nevertheless it has been demonstrated that an UWB pulse can be generated with inexpensive components, and although they do not fully comply with regulation, they can find use in time-domain antenna UWB characterisation.

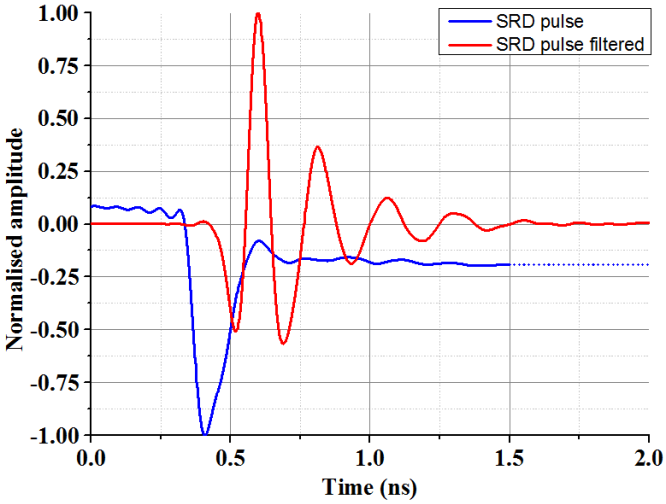

Figure 3-18: Original and filtered SRD pulses

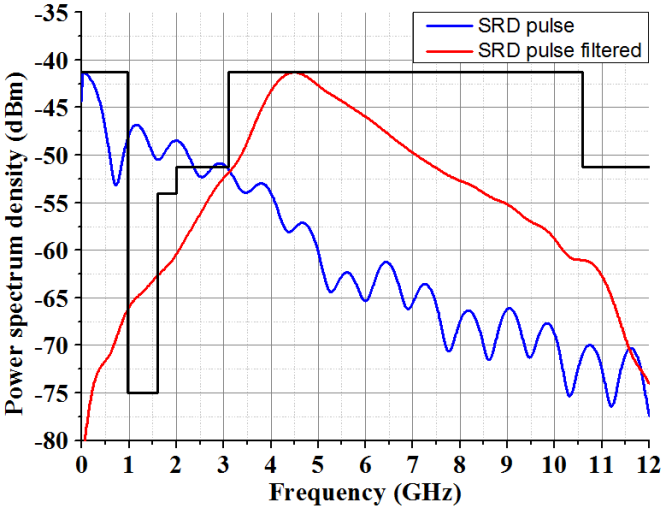

Figure 3-19: Original and filtered SRD pulse power spectrum density

3.3. Radiation of UWB Signal

Compared to narrow band signals, UWB signals exhibit interesting features when radiated. A narrow band radiated signal closely resembles a sine wave independently of wherever their observation point is, while UWB signals have different shapes depending of the radio link observation point.

It is well known that radiation in free space is the result of a time-varying current or acceleration of charges [45] [46]. When an antenna is excited with a signal, the

current travels along the conductive materials and encounters discontinuities in the conductors. These cause a change in current velocity and produce radiation as well as the opposite polarisation of the surface currents. Since acceleration is the time derivative of the velocity, it is expected that the radiation coming from the antenna corresponds to the partial derivative in time and delay of the current [47]. For narrow band signals this effect is not really important since, the derivative of a sinusoidal signal is a cosinusoidal signal, meaning that the signal shape will remain the same through the radiation process. However, the wider the pulse bandwidth is, the more the pulse differs from its time derivative. Consequently, for UWB systems, the shape of radiated signals will be dependent on the observation point, the type of antenna and will be different from the excitation signal at the antenna feed point [48] [49] [50].

Researchers have studied the antenna effect, when operating in transmitting mode, on UWB pulse shape [51]. It appears that only a few antennas, such as the long dipole and biconical antenna, are able to transmit a replica of the excitation signal [52] as long as the signal does not contain DC components. In general, UWB antennas tend to radiate a time derivative of the input signal [51]. Table 3-1 shows the general relationship between the input signal and the radiated signal for different antennas. By knowing the impulse response of the antenna, its effect on the radiated signal can be taken into account during the design of the UWB system, especially for precision ranging system. Also, if the impulse response of the antenna operating in transmitting mode is known, it is possible to synthesize the excitation pulse for the desired radiated signal [52].

Antenna	Radiated signal Versus excitation signal
Long dipole (h=∞)	*Replica*
Short dipole (h=0)	*2nd derivative*
Bicones (90° flares)	*Replica*
TEM horn	*1st derivative*
Vivaldi	*1st derivative*
Bow-tie	*1st derivative*

Table 3-1: Relationship between the input and radiated signal for different antennas

3.4. Reception of UWB Signal

The reception of UWB signals also exhibit interesting characteristics compared to the reception of narrowband signals. In the previous section it has been shown that the transmit impulse response of an antenna has little effect on the narrow band signal shape, since the derivative of a sinusoidal signal is also a sinusoidal-like signal and it is also valid for an antenna operating in receiving mode. However for the reception of UWB signals, the impulse response of the antenna in receiving mode can impair the received signal.

Signal reception is due to the electric field incident in the conductive surface of the antenna. Hence, the receiving voltage at the antenna feed point is the convolution of the incident field and the surface current that will be present on the antenna operating in transmitting mode, integrated over the volume [48].

M. Kanda has demonstrated that the transient response of an antenna operating in transmitting mode is proportional to the time derivative of the transient response of

the antenna operating in reception mode [35]. For example, a bicone antenna in receiving mode will have a received signal at its port that approximately corresponds to the integral of the incident electric field as shown in [51] [52]. Table 3-2 shows the relationship between the incident field and the received signal for antennas operating in receiving mode.

Antenna	**Received signal Versus incident signal**
Long dipole (h=∞)	*Integral*
Short dipole (h=0)	*1st derivative*
Bicones (90° flares)	*Integral*
TEM horn	*Replica*
Vivaldi	*Replica*
Bow-tie	*Replica*

Table 3-2: Relationship between the received signal versus the incident field for different antennas

From Table 3-1 and Table 3-2, and assuming that the antennas are not dispersive, it is seen that it is possible to create a radio channel where the received signal is proportional to the excitation signal.

3.5. Conclusion

In this chapter, the FCC UWB power regulation mask was described and several types of UWB signals were characterised and assessed in relation to the IEEE 802.15.4 standard UWB requirements.

It has been shown that the modulated Gaussian signal (the most commonly used in antenna design) cannot take full advantage of the UWB mask. It appears that the SRRC pulse is better suited and can provide an improved antenna time-domain characterisation by providing a quasi-constant energy level throughout the UWB frequency range. Moreover, its spectrum shape can be adjusted to fit different requirements, unlike other pulses.

It was also shown that the radiation and reception of UWB pulses differ from the radiation and reception of narrowband signals. The shape of the radiated pulse is dependent not only on the observation point but also on the impulse response of the transmitting antenna. Equally the received signal is dependent on the antenna orientation and the impulse response of the receiving antenna at the reception point. Moreover, the relationship between the impulse response of an antenna operating in transmitting mode and in reception mode was clarified.

CHAPTER 4: UWB MONOPOLE PERFORMANCE IN PROXIMITY TO PLANAR REFLECTORS

The power restrictions of IR-UWB radio imply that its use is generally limited to short range systems which may be portable. Also, in order to stimulate and to satisfy the electronic devices market, ever increasing functions and thus components are embedded into portable devices. This miniaturisation trend demands that antennas are integrated or placed close to PCB boards and electronics components.

In this chapter the time-domain performance of antennas in close proximity to a planar reflector is investigated. The study was validated with the fabrication of a compact UWB monopole antenna and by frequency- and time-domain measurement.

4.1. Antenna Geometries and Optimisation

4.1.1. Geometry

In order to assess the effect of a planar reflector in proximity to a UWB antenna, a UWB monopole was designed using an evolutionary algorithm and Bézier spline and optimised for wide-band performance and pulse fidelity in the frequency range of 3.1 to 7 GHz, using a multi-objective cost function. The antenna consists of a 50 Ω single-ended microstrip-fed monopole with the radiator and ground plane optimised using mirror spline elements. It was fabricated on a 20×36×0.7 mm FR4 double-sided PCB with a dielectric constant ε_r = 4.3 and loss tangent 0.02. The substrate dimensions were chosen following the work of researchers on ground

plane dimensions on antenna properties [53] and from previous antennas design. The geometry of the antenna is shown in Figure 4-1.

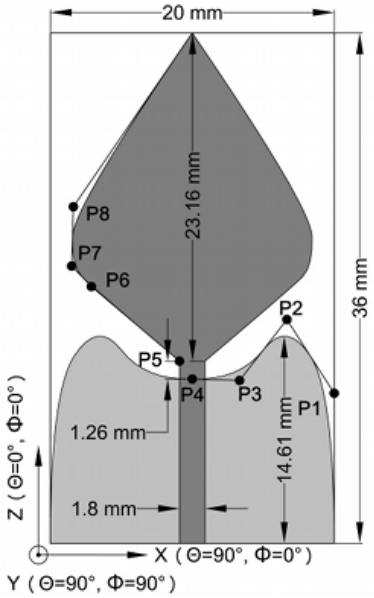

Figure 4-1: UWB monopole geometry and coordinate system

4.1.2. Optimisation

The UWB monopole was optimised using 8 construction points. The radiator construction point P5 uses one degree of freedom (Z-axis) while P6, P7 and P8 use 2 degrees of freedom (X and Z axis). The ground plane construction points (P1 to P4) use one degree of freedom (Z axis) in order to limit the complexity of the problem, raising the number of variables to 11. Table 4-1 shows the parameters constraints in millimetres.

$$P_{1,2,3,4}(z) = 5 < z < 20$$
$$P_5(z) = P_4 < z < (P_4 + 5)$$
$$P_{6,7,8}(x) = 0 < x < 10$$
$$P_{6,7,8}(z) = P_5 < z < 36$$

Table 4-1: UWB spline monopole geometry parameters (mm)

In order to efficiently optimise the antenna geometry, a genetic algorithm was used. At the time of the study, the CST package did not have an embedded optimiser and thus the antenna was optimised using a GA from the matrix software MATLAB

interfaced with the EM package CST Microwave Studio. For time-domain optimisation, 36 farfield virtual probes were placed around the H-plane in 10° steps to capture the radiated signal. The antenna was assessed by using two weighted goals, bandwidth and pulse fidelity, embedded in a cost function similar to the one proposed by M. John [54] and shown in Equation (4.1)

$$Cost = 1 - \left(0.3\,\frac{\zeta}{\mu} + 0.7\,\frac{\sum FF}{\gamma}\right) \text{ with } 0 \leq Cost \leq 1 \tag{4.1}$$

where ζ is the number of points for which $S_{11} < -10$ dB, μ is the number points that contain the S_{11} curve, FF is the fidelity factor (field probes relative to the derivative of the excitation pulse) at each angle and γ is the number of FF values. From Equation (4.1), it is seen that the possible values of the cost function lie between 0 (best result) and 1 (worst result) while the empirically selected coefficient weightings were chosen to provide a balance between optimization time and accuracy.

The excitation signal used during the optimisation was an amplitude modulated Gaussian signal, from the CST Microwave Studio package, having 3.9 GHz bandwidth at −20 dB. The initial population of the GA has been set to 1375 (125 individuals per variables). This number was found empirically and allows the GA to create a broad search landscape. The remaining populations were set to 70 and stop after 30 generations. The roulette selection scheme and the intermediate cross-over were used in the GA. Figure 4-2 represents the two objectives (X-Y axis) in terms of the number of iterations. It is seen that the GA considered has efficiently explored the search landscape during the first generation, in other words, up to the 1375th iteration. Then on each generation the result is refined, represented by the darker colour, until the GA stops at the 30th generation.

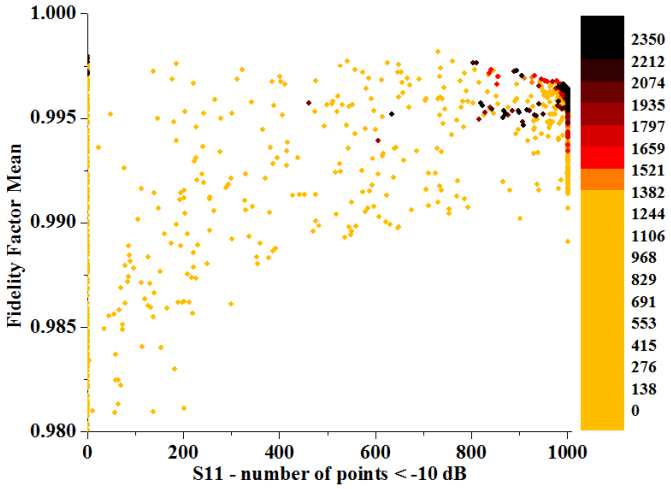

Figure 4-2: UWB spline monopole optimisation goal in terms of iteration number

4.2. Free Space Results

4.2.1. Return Loss

In order to measure the effect of the planar reflector on the performance of the antenna, it is essential to characterise the antenna in free space. To do so the antenna was measured by a Rohde & Schwarz ZVA 24 vector network analyser, illuminated in an anechoic chamber. The S_{11} of the antenna in free space is represented on Figure 4-3. Good agreement is achieved between simulation and measurement. The measured data exhibits a 10 dB bandwidth from 3.23 GHz to 8.14 GHz and a 6 dB return loss from 2.9 GHz to 9.29 GHz.

4.2.2. Radiation Pattern

The radiation patterns were measured in the H-plane (X-Y plane) from 3.1 GHz to 7 GHz to evaluate the radiation pattern stability. Figure 4-4 shows the measured co-polar realised gain in term of angle versus frequency. From 3.1 GHz to 7 GHz the radiation pattern remains stable and omnidirectional, with a peak of 4.3 dBi (φ, θ = 90°, 90°) at 7 GHz.

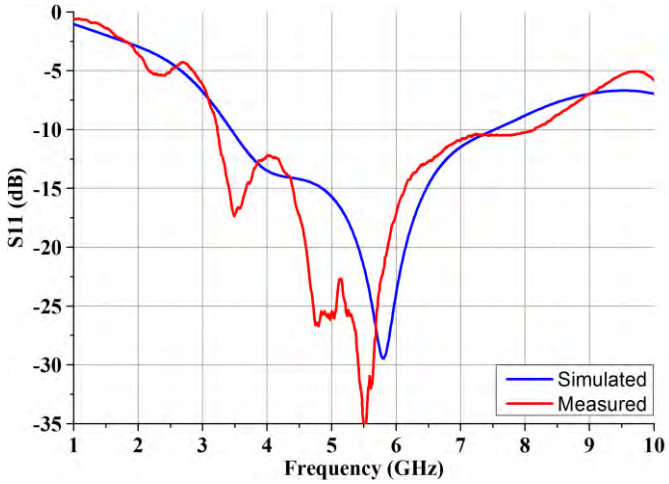

Figure 4-3: Simulated and measured S_{11} for the UWB spline monopole in free space

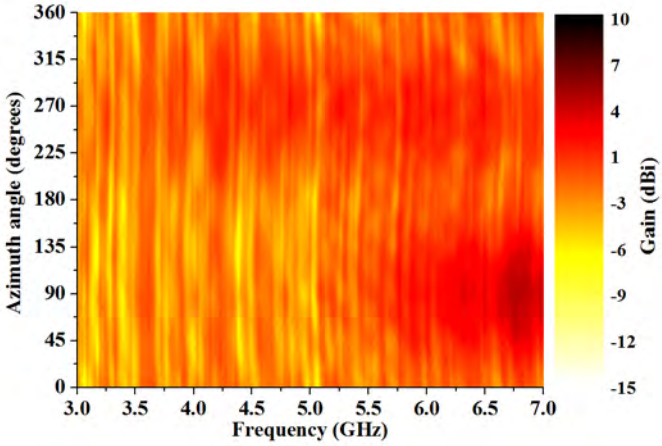

Figure 4-4: Measured free space radiation pattern of the UWB spline monopole

4.2.3. Fidelity Factor

In order to characterise the time-domain performance of the antenna, the transmission coefficients of the antenna system, composed of two identical UWB spline monopoles, were measured. The impulse responses of the channel were determined using the time-domain post processing capability of the vector network analyser [55] [56] [57] and were recorded every 5° degrees on the azimuth plane and quantified by cross-correlating the input impulse response against the channel impulse response. As seen in Figure 4-5, the simulated and measured fidelity factors are in good agreement while the antenna time-domain performance is very good. It shows an omnidirectional pulse fidelity pattern while the antenna system exhibits a

measured fidelity factor (FF) mean of 99.8% with the lowest and highest values equal to 99.7% (φ, θ = 90°, 45°) and 99.9% (φ, θ = 90°, 225°) respectively.

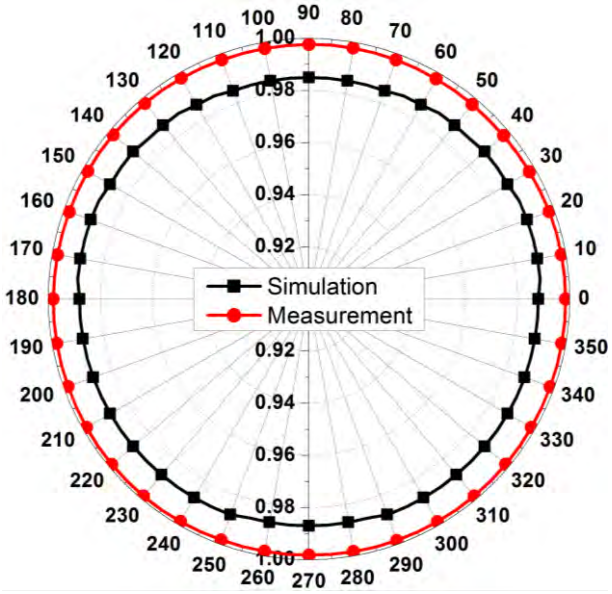

Figure 4-5: Measured Fidelity Factor

4.3. Reflector Proximity Effect on Antenna Performance

Generally, UWB antennas are likely to be embedded and in close proximity to metallic surfaces which can act as reflectors. These pseudo-reflectors can impair the performances of antenna in some cases. Therefore the study of reflector proximity effect on antenna performance is important, especially for integrated antenna.

4.3.1. Return Loss

In order to study the effect of reflector proximity on antenna performance, a sheet of brass of dimension 100 × 100 mm was positioned at various distances (from λ to λ/8 at 3.1 GHz) from the receiving antenna while both of them were rotated in 5° steps. Figure 4-6 represents the experiment while Figure 4-7 and Figure 4-8 demonstrate the effect of the reflector proximity on the S_{11}. It is seen that the

proximity of the reflector is negligible on S_{11} until the separation *d* between the antenna and reflector approaches λ/4.

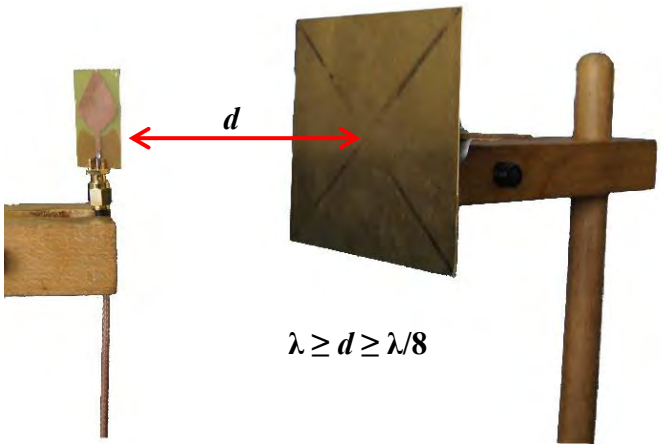

Figure 4-6: Experimental setup

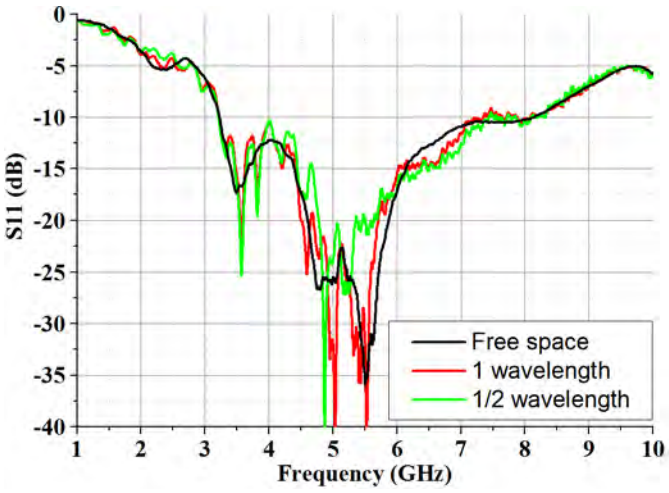

Figure 4-7: S_{11} dependence on antenna–reflector separation

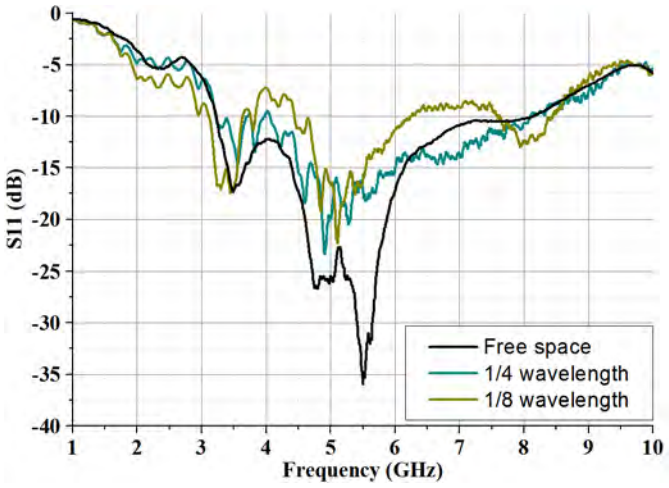

Figure 4-8: S_{11} dependence on antenna–reflector separation from λ/4 to λ/8

From λ/4, the S_{11} degrades especially from 3.5 to 4.5 GHz and from 6 to 7 GHz due to an increased variation in input impedance with frequency. However, even with d = λ/8, the return loss is still acceptable with a 6 dB bandwidth of 7.03 GHz starting from 1.98 GHz to 9.01 GHz.

4.3.2. Radiation Pattern

The measured azimuthal radiation pattern is shown in Figure 4-9. Up to d = λ/4, the radiation pattern exhibits additional side lobes also "scalloping effects" [58]. Referring to Figure 4-9, this effect is maximal for a separation of λ and is gradually reduced for shorter values of *d*.

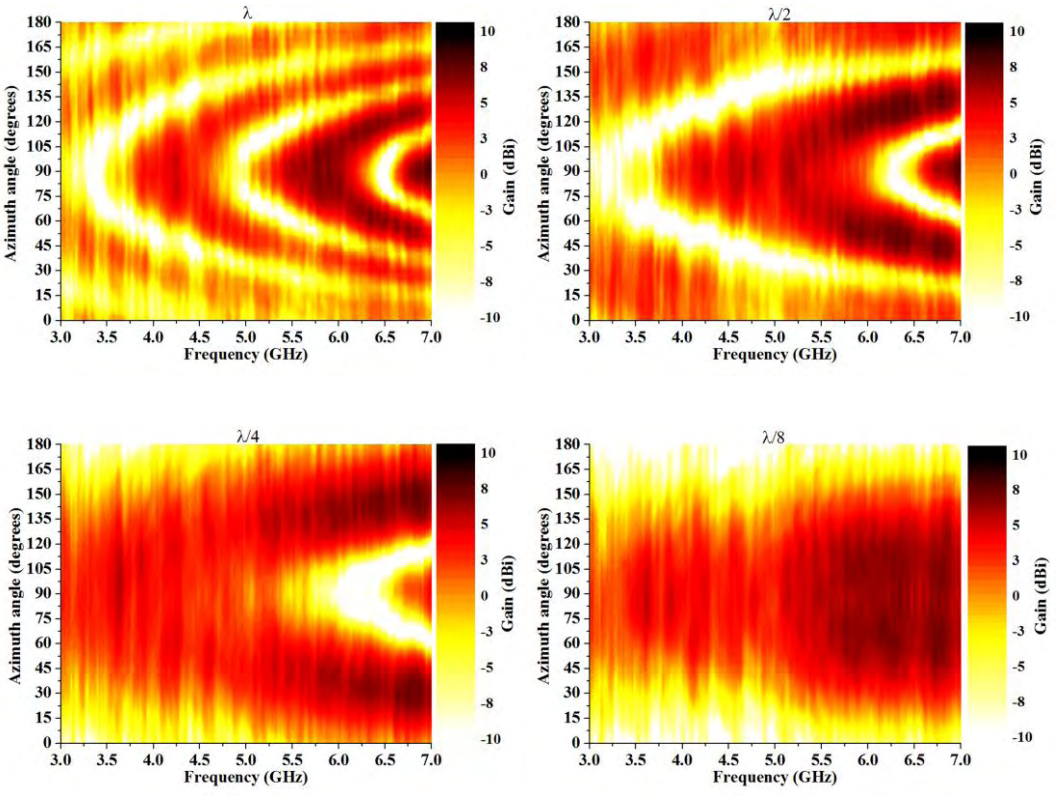

Figure 4-9: Realised gain radiation pattern angle vs. frequency in terms of antenna-reflector separation

For d>λ, a larger number of lobes will also be formed. The antenna-reflector combination can be approximated as a horizontal dipole over a horizontal infinite

perfect conductor. From this simplification the total number of lobes can be calculated from this equation [58], unity being the smallest number.

$$N_{LOBES} \cong 2\left(\frac{d}{\lambda}\right) \tag{4.2}$$

It is also seen that the directivity of the antenna increases when the separation *d* is short (λ/4 and λ/8). The simulated maximum directivity of the UWB spline monopole versus the distance *d* is shown in Figure 4-10. It is seen that the directivity is maximum at a separation of around λ/12, reaching a value of 8.3. At 0 λ the ground plane is shorting the antenna and no signal will be radiated from the antenna elements.

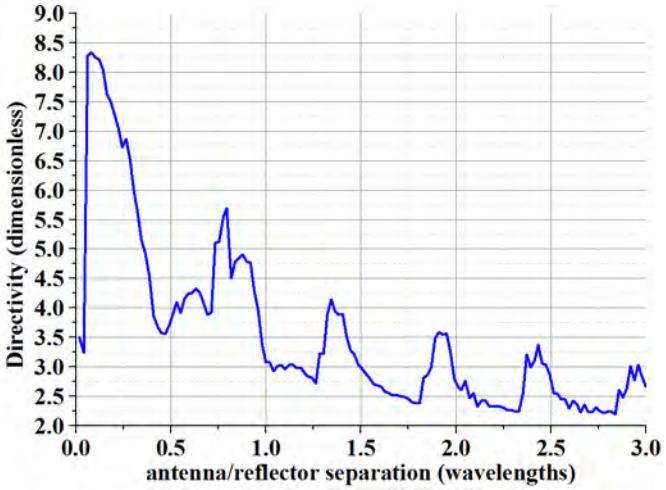

Figure 4-10: Maximum directivity of the antenna system in term of antenna-reflector separation.

4.3.3. Fidelity Factor

By using the method presented in Section 4.2.3, the impulse response of the antenna system was recorded for every 5° between φ=0° to φ=180° in the azimuth plane. Figure 4-11 shows the input impulse response versus the antenna system impulse responses for different values of *d* at φ= 90°. For *d* =λ, the second peak represents the reflected signal from the reflector. For *d* = λ/2, it is seen that the Full Width at Half Maximum (FWHM) was increased by 140 ps compared to the FWHM

input impulse response. This increase of width indicates that a signal reflection occurs but cannot be fully distinguished, due to the windowing function (*hann* windows), and the frequency range (3.1 to 7 GHz) limiting the discontinuity resolution [59]. By increasing the frequency span the resolution will be improved, but the antenna will be tested over a broader range of frequencies than designed for, corrupting the time-domain result. If a rectangular window is used, better accuracy can be achieved in the main pulse, but at the expense of accuracy in the impulse response side lobes [59]. Consequently the default windowing function (*hann* windows) was chosen for measurement. In order to quantify the impulse response distortion versus the distance *d*, the reference impulse response was cross-correlated against the different antenna impulse responses. Figure 4-12 shows the spatial fidelity factor and indicate the effect of the reflector on the pulse fidelity. It is interesting to note that the best time-domain performance is achieved when the reflector is located at a λ/4 from the received antenna.

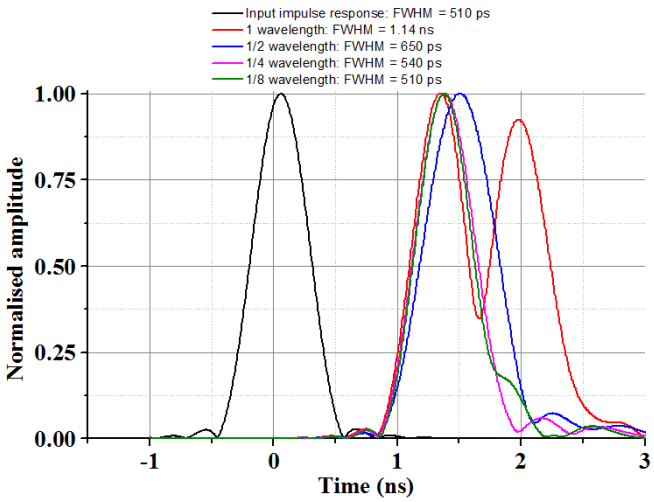

Figure 4-11: Input and antenna system impulse response in term of antenna-reflector separation

Figure 4-13 represents the measured antenna system impulse response 2D surface plots. For an antenna–reflector separation of λ and λ/2, the impulse response

is clearly distorted at every angle with a peak signal reflection occurring at φ= 90°. However for a separation of less than a λ/4, the impulse response is rather homogeneous through the azimuth plane.

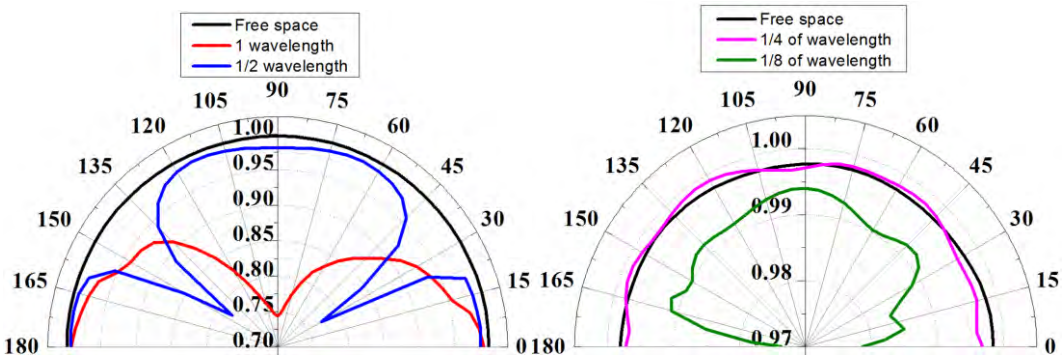

Figure 4-12: Impulse response fidelity factor for different antenna-reflector separation

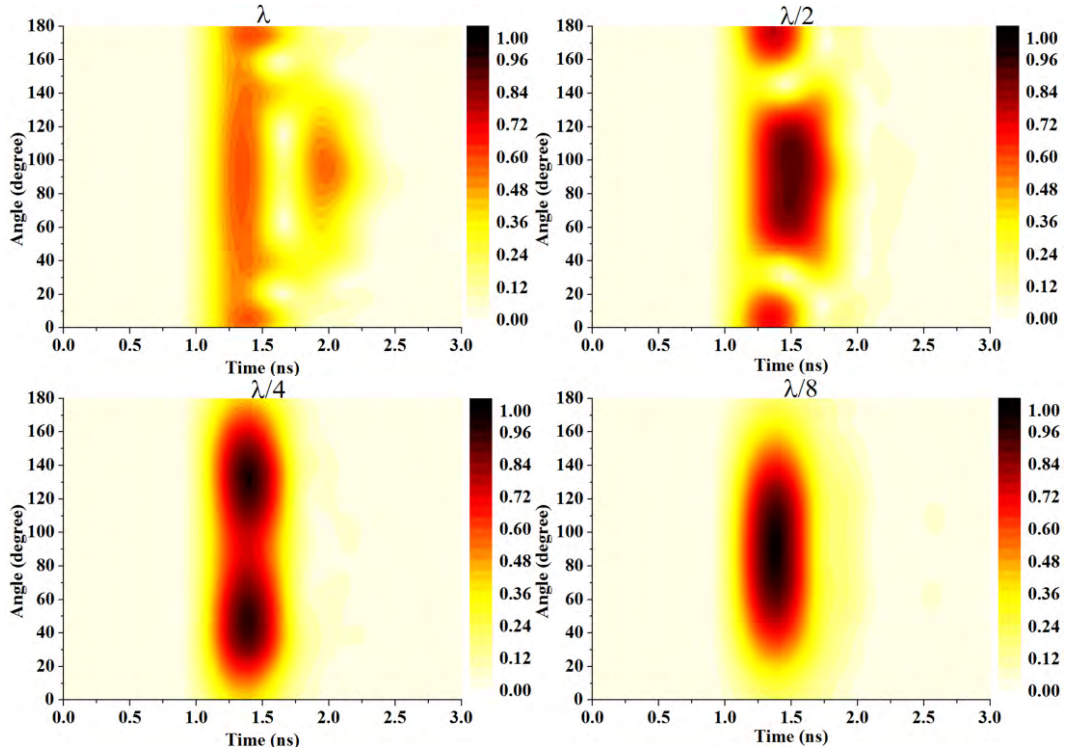

Figure 4-13: 2D surface graph representing the measured normalised impulse response in terms of angle versus time.

4.4. Conclusion

In this chapter, the effect of a 100 × 100 mm planar reflector on the pulse performance of an UWB spline monopole was presented. The antenna was optimized for time-domain performance over a frequency range of 3.1GHz to 7 GHz (band 1 to band 7). The antenna time-domain performance was measured using the time-domain post processing capability of a VNA. The free space measurements demonstrated that a system composed of a pair of identical UWB spline monopoles achieved an impulse response fidelity factor of 99.8% on average, for this frequency range. These performances were compared with those of an antenna system with reflector. It was shown that when the reflector is close to an antenna ($\lambda/4$), the antenna directivity significantly increases while the time-domain performance of the antenna remains comparable with those of the antenna in free space. However for larger antenna–reflector separation ($d > \lambda/2$), the antenna's performance, in both frequency- and time-domain, were impaired, due to formation of side lobes in the radiation pattern. In terms of application, the presence of a reflector can be advantageous due to the increased directivity, gain and pulse fidelity preservation.

Concerning the time-domain capability of the VNA, this measurement technique is efficient at providing information of the device performance at specific locations. However this method is unable to provide information on the time-domain performance of a single antenna and it has been shown that the results depends on the type of windowing function used and the frequency span, raising the need to have a more accurate measurement procedure.

CHAPTER 5: NOVEL METHOD FOR ANTENNA TIME-DOMAIN OPTIMISATION

This chapter describes the implementation of a new optimisation method to improve UWB antenna time-domain performance. Traditionally, UWB antennas were designed using Gaussian signals and Rayleigh pulses for antenna excitation [30] [60] [61] [39]. Their characteristics include a bell shaped energy distribution, very low level side lobes in the frequency-domain and fast energy damping in the time-domain. Using this method, several types of antennas were successfully designed [62] [63]. However, as the energy distribution of Gaussian like signals is not optimal for the UWB spectrum mask, this allows frequency discrimination during the optimisation. To compensate for this shortcoming, a series of modulated Gaussian pulse can be sequenced to cover the entire UWB mask [30] or by using a chirp signal [64]. However these approaches are not-suitable for antenna optimisation because they significantly extend the duration of the simulation time, which is proportional to duration of the excitation signal, and add complexity to the time-domain analysis of the models. However one solution to overcome the limitations is to use a SRRC pulse.

In this chapter, antennas will be optimised for time-domain performance by interfacing a GA with CST Microwave Studio, and by using a Gaussian and SRRC pulses as excitation signals. The radiating element and ground plane geometries are outlined using Bézier spline curves and are optimised simultaneously using control points. A key aspect of this chapter is to demonstrate that using a SRRC pulse as an

excitation signal during the optimisation process generates UWB antennas with superior time-domain performance.

5.1. Monopole Antenna Construction and Modelling

As seen in Section 3.2.3, it is clear that the SRRC signal has a more broadband energy profile compared to the Gaussian signal. Because of this essential characteristic, the SRRC signal can be used as an excitation signal to fully characterise and optimise the antennas for UWB time-domain performance.

In order to solve the pulse performance limitation imposed by traditional canonical shapes, the antenna radiator and ground plane geometries were designed using Bézier splines [18]. These curves allow for the generation of a large number of configurations. Monopole type antennas were designed for ultra wideband and dispersionless performance. In order to validate the SRRC optimisation approach, a monopole (*GM*) was optimised using the default Gaussian signal from CST Microwave Studio, while monopole (*SM*) was optimised using a SRRC excitation signal. These two antennas are shown in Figure 5-1 and Figure 5-2 respectively. In order to obtain superior performance in time-domain, the microstrip fed monopoles were optimised using mirrored splines with independent control points for both the ground plane (4 points) and the radiator (4 points). The ground plane spline points have one degree of freedom (Z-axis) as well as *P5* while the other radiator spline points have two degrees of freedom (X and Z-axis) as shown in Table 5-1. Antennas were designed and manufactured on a 40 × 40 × 0.7 mm FR4 double-sided laminate with a dielectric constant $\varepsilon_r = 4.3$ and loss tangent = 0.02. The antennas were initially performance-optimized when configured with the system circuitry in the simulation model; therefore without SMA connectors.

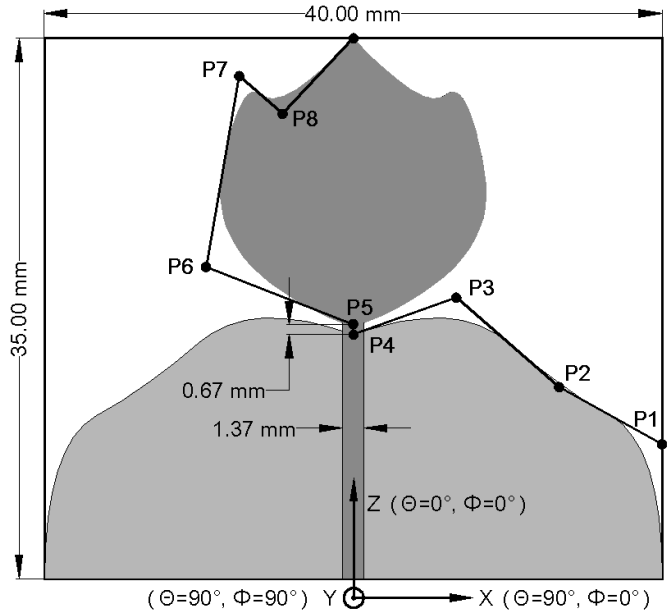

Figure 5-1: Gaussian Monopole *GM* geometry and coordinate system

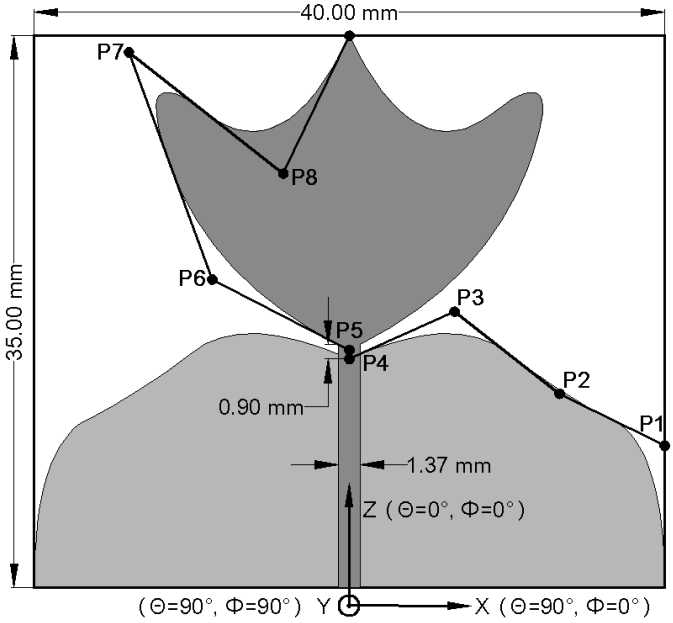

Figure 5-2: SRRC Monopole *SM* geometry and coordinate system

5.2. Design Optimisation

The shapes of monopole *GM* and *SM* antennas were optimised by CST Microwave Studio interfaced with the GA optimisation package from MATLAB. Compared with CST's GA optimiser, MATLAB's GA offers much improved setup options, such as the type of scaling, reproduction, mutation and crossover function to

name a few. The monopoles were optimised by assigning 11 parameters until the GA converges to a maximum performance goal. Table 5-1 indicates the different dimensional constraints, in millimetres, assigned to the optimiser.

$$P_{1,2,3,4}(z) = 5 < z < 25$$
$$P_5(z) = P_4 < z < (P_4 + 5)$$
$$P_{6,7,8}(x) = 0 < x < 20$$
$$P_{6,7,8}(z) = P_5 < z < 40$$

Table 5-1: Antennas geometry parameters (mm)

For time-domain optimisation, farfield probes were used to capture the radiated signal at different locations around the antenna H-plane. Because of the geometrical symmetry of the antenna, field symmetry in CST was used while limiting the probe to $\theta = 90°$, $90° \leq \varphi \leq 270°$ in 5° steps. During the optimisation, the antennas were assessed by using a weighted cost function using Equation (5.1) and Equation (5.2)

$$Cost = 1 - \left(0.3\,\frac{X}{\alpha} + 0.7\,\frac{\sum FF}{\gamma}\right), \text{ for } X < \alpha \tag{5.1}$$

$$Cost = 1 - \left(0.3 + 0.7\,\frac{\sum FF}{\gamma}\right), \quad \text{for } X \geq \alpha \tag{5.2}$$

Where X is the least magnitude value in the S_{11}, α is the S_{11} match target, FF is the fidelity factor (field probes relative to the derivative of the excitation pulse) at each angle and γ is the number of FF values. Equation (5.2) aims to prevent the optimizer to favour minimum S_{11} value at the expense of the FF value. Therefore, the range of the cost function lies between 0 and 1, zero the being the optimum value. Initially the GA had an initial population of 1650 individuals, which was then reduce to 165 for the remaining populations. The initial population number was chosen empirically to create a broad search landscape and thus to prevents the GA being stuck in local optima. The algorithm also uses an intermediate crossover, the roulette wheel selection, and stops after 30 population iterations (maximum antenna simulations ≤

8085). Also, a script was implemented to skip simulations of non-realistic structures, occurring mainly during the earlier generation, and re-simulation of identical structures appearing as the algorithm converges to an optimum solution. This subroutine significantly reduces the theoretical maximum optimisation time of 89.8 hours, while having minimum effect on the GA behaviour. Figure 5-3 represents the two objectives (X-Y axis) in terms of the number of iterations for the monopole *GM*. The first 1650 iterations (1st generation) indicate that the GA explored a broad search landscape. From 1650th iteration to final one, the GA progressively refines the different parameters towards the optimum values which are shown in darker colours.

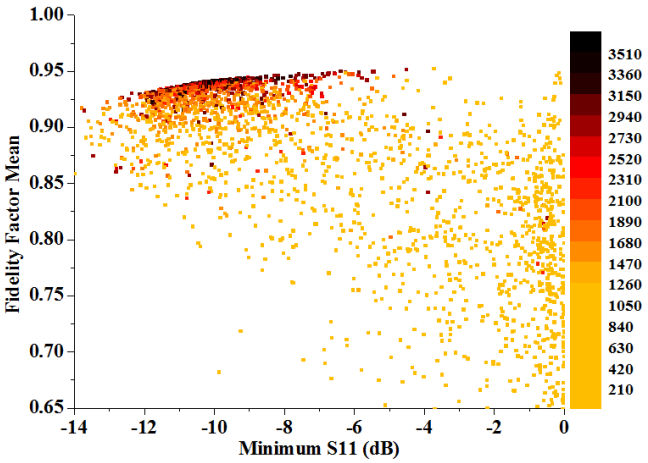

Figure 5-3: Monopole *GM* optimisation goal in terms of iteration number

5.3. Frequency-domain Results

5.3.1. Return Loss

The simulated and measured S_{11} for monopole *GM* and monopole *SM* are illustrated in Figure 5-4. Both antennas have a good impedance matching for the 3.1-10.6 GHz band, exhibiting a 10 dB return loss for 3.06 - 12.21 GHz and 2.97 - 12.22 GHz respectively, with good agreement between measurement and simulation.

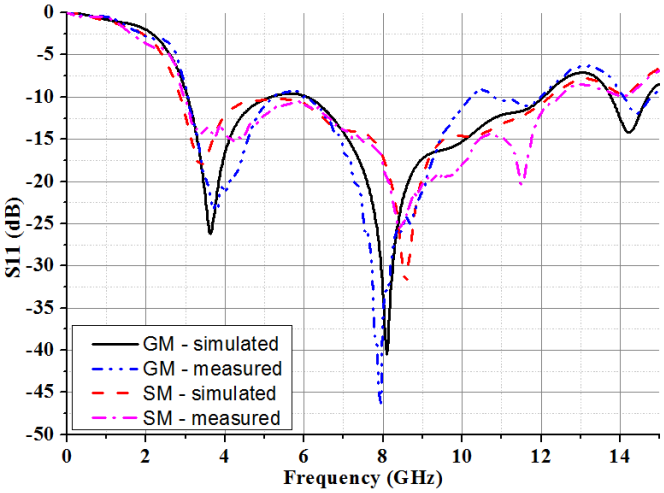

Figure 5-4: S_{11} for monopole *GM* and monopole *SM*

5.3.2. Radiation Pattern

The monopole radiation patterns were measured in the H-plane (X-Y plane) from 3-11 GHz to evaluate the performance of the antenna, in terms of realised gain and radiation pattern stability. Figure 5-5 and Figure 5-6 represent the measured co-polar gain against the frequency and azimuth angle for the monopole *GM* and the monopole *SM*. It is seen that both antennas exhibit an omnidirectional radiation pattern. The gain values are good across 3.1-10.6 GHz with an averages of 0.75 dBi (std. dev. = 2.29) for monopole *GM* and 0.8 dBi (std. dev. = 2.23) for Monopole *SM*. The respective maximum gains are 4.53 dBi (θ, φ = 90°, 40°) at 8.27 GHz and 4.51 dBi (θ, φ = 90°, 25°) at 8.93 GHz.

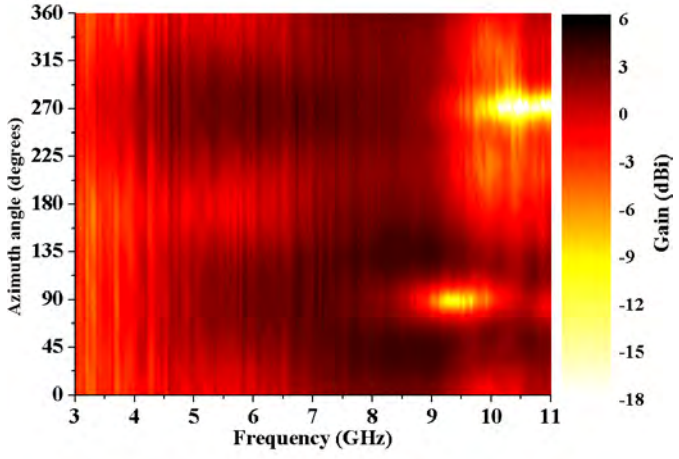

Figure 5-5: Measured monopole *GM* radiation pattern in the θ=90° plane

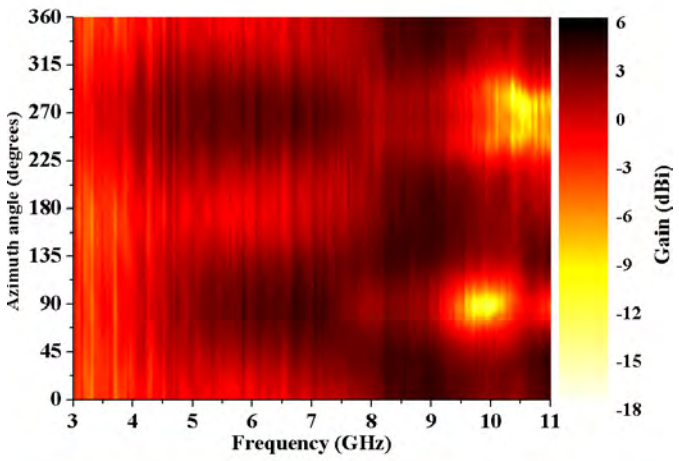

Figure 5-6: Measured monopole S*M* radiation pattern in the θ=90° plane

5.4. Time-domain Results

The fidelity factor was used as a metric to quantify the time-domain performance of the antennas. In an antenna system, the radiated pulse and the received signal are functions of the source pulse, the antenna and its operating mode. In Section 3.4 it was shown that the transient response of an antenna in transmitting mode is proportional to the time derivative of the transient response of the same antenna in receiving mode. It also has been shown that UWB antennas, in general, radiate the time derivative of the input signal. Consequently the radiated pulse must be cross-correlated with the 1st order time derivative of the input signal.

5.4.1. Simulation Results

In order to compare the performance of monopole *GM* and monopole *SM*, the antennas were fed using a modulated Gaussian signal and modulated SRRC UWB pulse (see Figure 3-14). Figure 5-7 represents the FF for the monopole antennas fed by the Gaussian and SRRC. The analysis of this graph indicates that the antennas fed with the SRRC pulse have lower FF values. Indeed because the SRRC signal is more broadband than modulated Gaussian signal, the radiated pulse is subject to more

frequency filtering effects from the antennas. Table 5-2 shows the antenna FF performance range when fed with a Gaussian and SRRC signal. It also shows that monopole *GM* outperforms monopole *SM* even though the latter antenna was optimised with an optimal UWB pulse. In order to explain this apparent contradiction each antenna was simulated with three narrow-band modulated SRRC excitation pulses ($\beta = 0.5$ and $R_S = 1.95\times10^9$, 2.5 GHz bandwidth at −10 dB) at different centre frequencies across the UWB band as shown in Figure 5-8 and Figure 5-9. Table 5-3 indicates that an antenna optimised with an SRRC pulse or with a signal having a constant energy level across the frequency range, achieved a better overall time-domain performance compared with an antenna optimised for Gaussian-like pulse. However monopole *GM* achieved better performance than monopole *SM* for the pulse centred at 6.85 GHz.

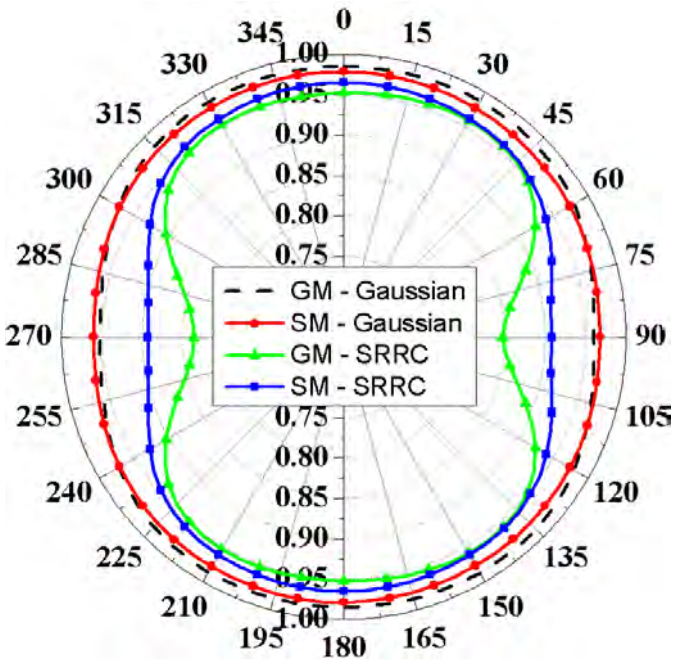

Figure 5-7: Simulated Fidelity Factor for monopole antenna fed with modulated Gaussian and SRRC pulse.

	Gaussian pulse		Square Root Raised Cosine pulse	
	Monopole GM	**Monopole SM**	**Monopole GM**	**Monopole SM**
Mean	0.97801	0.97395	0.93557	0.95598
Min	0.95237	0.96084	0.83538	0.89323
Max	0.98776	0.97888	0.95948	0.96498

Table 5-2: Fidelity Factor values for antennas fed by Gaussian & SRRC pulses

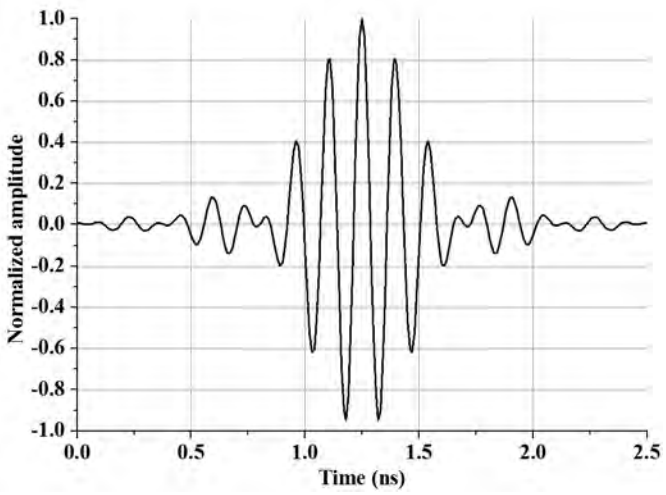

Figure 5-8: SRRC pulse: 2.5 GHz bandwidth, modulated at 6.85 GHz, with the peak value normalized to unity

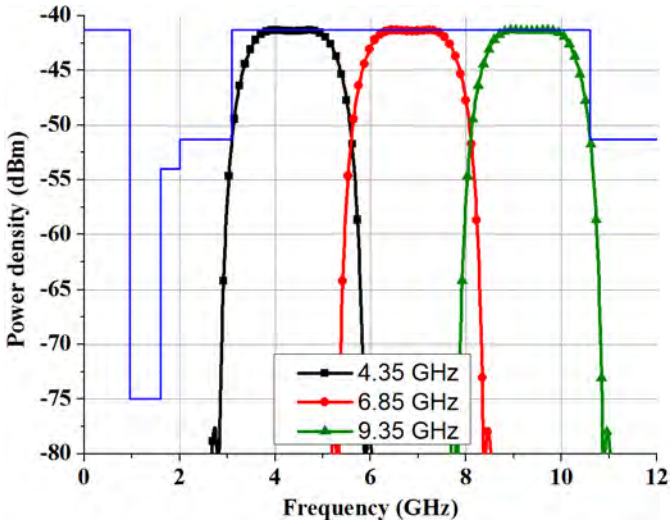

Figure 5-9: Spectrum Power Density for 2.5 GHz bandwidth SRRC pulse at various centre frequencies

	4.35 GHz	6.85 GHz	9.35 GHz
Monopole *GM*	0.97563	0.99647	0.97329
Monopole *SM*	0.98016	0.99270	0.99293

Table 5-3: Fidelity Factor mean for narrow band SRRC pulses

This result is due to the fact that monopole *GM* was optimised with a signal having its peak energy level at 6.85 GHz. Therefore the results show that the type of excitation pulse used for optimisation will affect how the optimiser will influence the antenna's geometric features. These also show that monopole *SM* has a better time-domain performance than monopole *GM* where the Gaussian pulse energy level is inferior to the energy distribution of the SRRC pulse, leading to a better overall time-domain performance compared to Gaussian optimised antennas.

5.4.2. Time-Domain Measurement Setup

In order to validate the simulation results, the antennas time-domain performances were measured at the Tyndall Institute, Cork, Ireland. To generate the SRRC UWB pulse, a digital sampled waveform was exported to a Tektronix AWG 7122C Arbitrary Waveform Generator (AWG). Due to its output voltage limitation, the AWG output signal was amplified with a Picosecond Pulse Labs wideband amplifier (Model 5865) and fed to the antenna under test. Also, in order to accurately measure the radiated pulse, the receiving antenna should not be dispersive. Consequently a directional tapered slot antenna was designed and its geometry is shown in Figure 5-10. Using the SRRC pulse (see Figure 3-14) as an incident signal instead of excitation signal, it was optimised for optimal time-domain performance on bore-sight in receiving mode. In this operating mode, the antenna has a simulated pulse fidelity factor of 98.6% at the bore-sight. This result indicates that the received signal at the antenna's port is nearly identical to the replica of the incident signal.

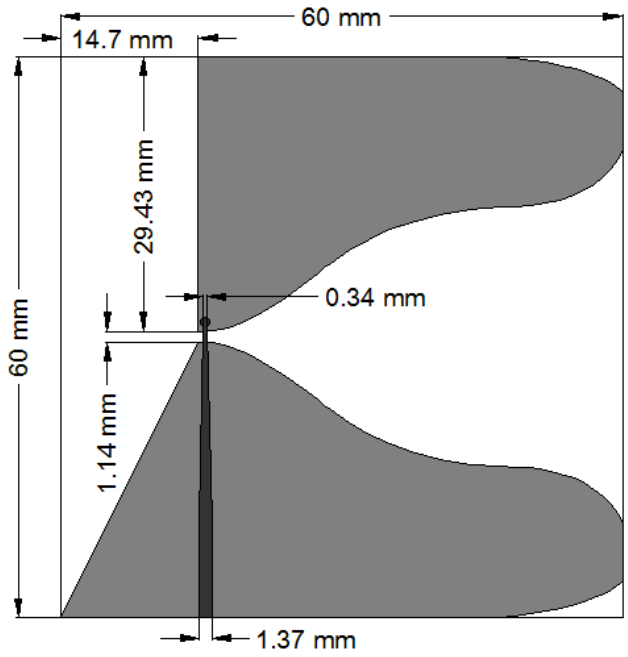

Figure 5-10: Tapered slot antenna optimised for time-domain performance in receiving mode

A distance of 20 cm was chosen between the transmitting and receiving antenna to maintain the farfield measurement while achieving an adequate signal to noise ratio (SNR) as from a distance of 50 cm, the SNR dropped to an unacceptable level, impairing the time-domain measurement. Figure 5-11, depicts the time-domain measurement setup.

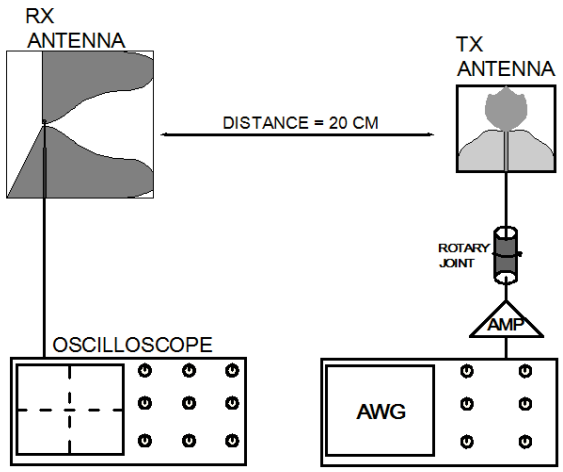

Figure 5-11: Time-domain measurement setup

5.4.3. Pulse Equalisation

Because of the imperfect impulse response of the transmit network components, the AWG generated SRRC pulse fed at the AUT's input port suffers from impaired frequency- and time-domain characteristics. If such a signal is fed to the transmit antenna, the measured pulse fidelity will not represent the full transient performance of the AUT.

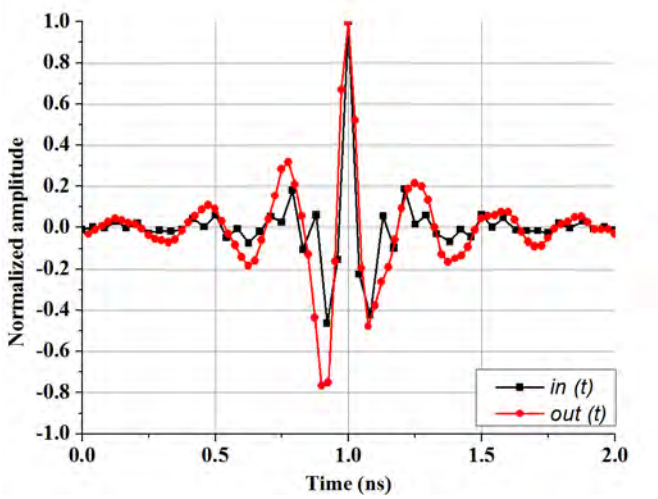

Figure 5-12: *in(t)* waveform to AWG and *out(t)* pulse

Figure 5-12 illustrates the AWG input waveform *in(t)* with the pulse *out(t)* offered to the transmit antenna. To subdue the component losses, the input signal was compensated using Equation (5.3), where the Inverse Fast Fourier Transform (IFFT) and the Fast Fourier Transform (FFT) are used to manipulate the pulse in frequency- and time-domain. In Figure 5-13, the power spectrum density of the compensated signal *out'(t)*, the input signal *in(t)* and the initial output signal *out(t)* are shown.

$$in'(t) = IFFT\left[FFT\big(in(t)\big) / FFT\big(out(t)\big)\right] \tag{5.3}$$

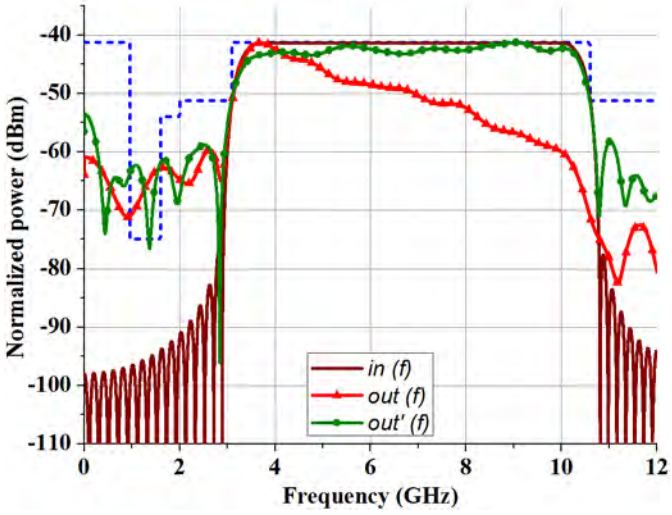

Figure 5-13: Input, output and output equalized pulse Power Spectrum

Compared to the original SRRC signal *in(t)*, the compensated signal *out'(t)* energy distribution level share many characteristics in the UWB band, demonstrating that the transmit network impulse response was equalised. Hence, the *out'(t)* signal was fed at the transmitting antenna port allowing an accurate time-domain characterisation of the AUT.

5.4.4. Antenna Impulse Response De-embedding

In the last section, an equalisation method was presented, suppressing the transmit network impulse response from the measurement. However, in order to get an accurate measure of the radiated signal, the receive network impulse response, which includes the one from the receiving antenna, should also be removed.

Using two identical antennas, in an antenna system configuration, and by using the method described by [65], it is possible to estimate the transient and frequency response of the AUT. Indeed, the UWB channel model can be decomposed in three different blocks, consisting of the transmitting antenna, the free space channel, and the receiving antenna. Each block can be described by a transfer function such as, $\vec{H}_{TX}(\theta, \varphi, \omega)$, $H_{CH}(\omega)$ and $\vec{H}_{RX}(\theta, \varphi, \omega)$, as shown on Figure 5-14.

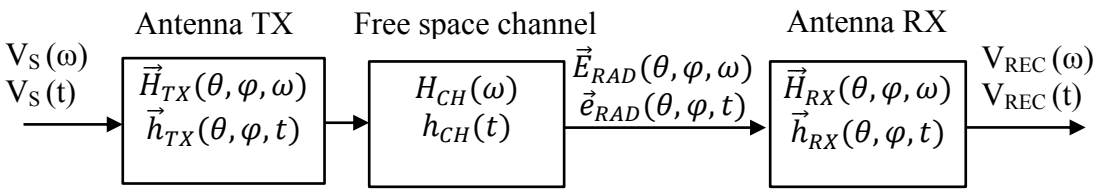

Figure 5-14: UWB channel model

Hence the UWB channel can be completely described in both frequency- and time-domain as shown in Equation (5.4) and Equation (5.5) [65].

$$\frac{V_{REC}(\omega)}{V_S(\omega)} = \vec{H}_{TX}(\theta,\varphi,\omega) \times H_{CH}(\omega) \times \vec{H}_{RX}(\theta,\varphi,\omega) \tag{5.4}$$

$$V_{REC}(t) = \vec{h}_{TX}(\theta,\varphi,t) * h_{CH}(t) * \vec{h}_{RX}(\theta,\varphi,t) * V_S(t) \tag{5.5}$$

where ω is the angular frequency, and the symbol $*$ is the convolution symbol. The free space channel transfer function can be defined using Equation (5.6), where c is the speed of light in free space, d is the antenna separation and λ is the wavelength.

$$H_{CH}(\omega) = \frac{\lambda}{2d}\exp\left(-j\omega\frac{d}{c}\right) \tag{5.6}$$

Then, by measuring the vectorial S_{21} of two identical antennas with same orientation, it is possible to deduce the transfer function of the antenna in transmitting and receiving mode as shown in (5.7) and (5.8).

$$\vec{H}_{TX}(\theta,\varphi,\omega) = \sqrt{\left(\frac{\vec{S}_{21}(\theta,\varphi,\omega)}{H_{CH}(\omega)}\frac{j}{\lambda}\right)} \tag{5.7}$$

$$\vec{H}_{RX}(\theta,\varphi,\omega) = \sqrt{\left(\frac{\vec{S}_{21}(\theta,\varphi,\omega)}{H_{CH}(\omega)}\frac{\lambda}{j}\right)} \tag{5.8}$$

By knowing the transfer function of the receiving antenna , the free space channel and the antenna system's S_{21}, the transfer function of the unknown transmitting antenna can be calculated has shown on Equation (5.9).

$$\vec{H}_{TX}(\theta,\varphi,\omega) = \frac{\vec{S}_{21}(\theta,\varphi,\omega)}{H_{CH}(\omega) \times \vec{H}_{RX}(\theta,\varphi,\omega)} \quad (5.9)$$

Hence the incident radiated pulse $\vec{e}_{RAD}(\theta,\varphi,t)$ at the receiving antenna can be deduced by using Equation (5.10)

$$\vec{e}_{RAD}(\theta,\varphi,t) = \vec{h}_{RX}(t) \; \bar{*} \; \left[IFFT\left(\vec{S}_{21}(\theta,\varphi,\omega)\right)\right] \quad (5.10)$$

where the symbol $\bar{*}$ stands for the deconvolution. Using this method, the measured radiated pulse from the transmitting antenna can be compared with the simulated radiated field captured from the virtual probe in the simulation model. It is seen that the measured radiated signal $\vec{e}_{RAD\_measured}(\theta = 90°, \varphi = 0°, t)$ is in good agreement with the simulated radiated signal $\vec{e}_{RAD\_simulated}(\theta = 90°, \varphi = 0°, t)$ as seen in Figure 5-15. Figure 5-16 demonstrates that the signal $\vec{E}_{RAD\_measured}(\theta = 90°, \varphi = 0°, f)$ energy distribution shares similarities, in the UWB frequency range, with the energy spectrum of the $\vec{E}_{RAD\_simulated}(\theta = 90°, \varphi = 0°, f)$ and the 1st order derivative of the reference signal *out'(f)*, demonstrating that the transmitting antenna tends to radiate a signal that is approximately proportional to the reference signal derivative at θ=90°, φ=0°.

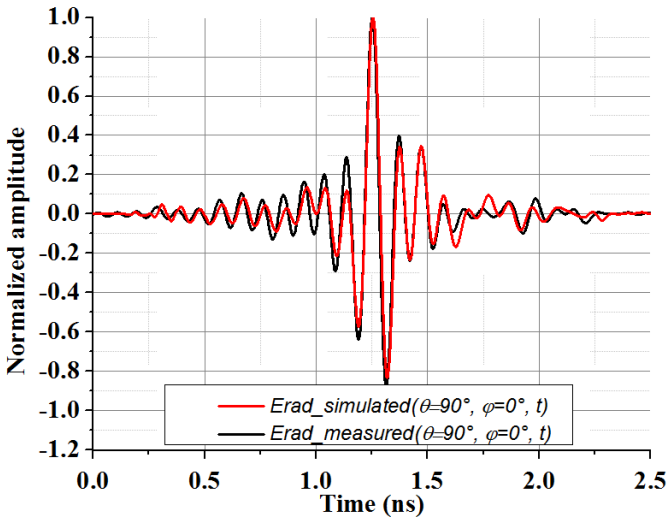

Figure 5-15: Simulated and measured radiated pulse

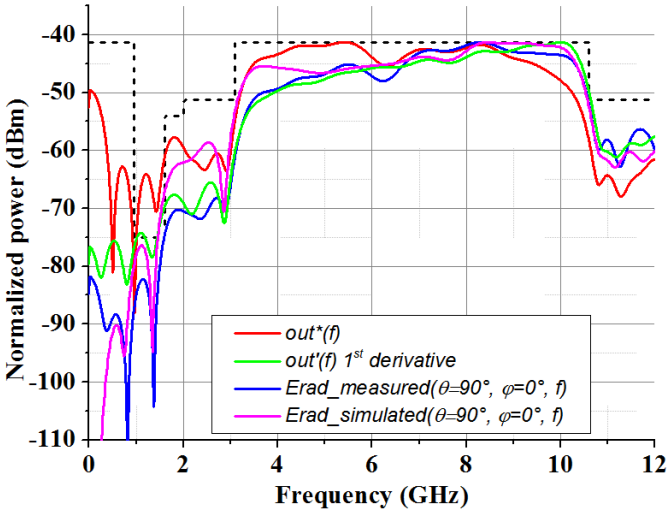

Figure 5-16: Received output signal *out*(t)*, 1st derivative pulse *out'(t)*, simulated radiated signal $\vec{e}_{RAD\_simulated}(\theta = 90°, \varphi = 0°, t)$, measured radiated signal $\vec{e}_{RAD\_measured}(\theta = 90°, \varphi = 0°, t)$, normalised power spectrum density.

5.4.5. Measured Time-domain Results

During the measurement process, the AUT was rotated in 15° steps in the radiation plane. In order to obtain an accurate oscilloscope pulse reading, the measured signal was averaged over 64 samples, improving the stability of the recorded pulse. The post-processed pulses were cross-correlated against the 1st order derivative of the AWG output pulse *out'(t)*, using the FF method, allowing a comparison with the simulated radiated results. Figure 5-17 shows the measured FF and simulated results with an equalised modulated SRRC excitation pulse. Good agreement between simulation and measurement is achieved. Furthermore the measured results confirm that antennas optimised with full UWB excitation signal have better performance in the full UWB range than antennas optimised with conventional optimisation techniques.

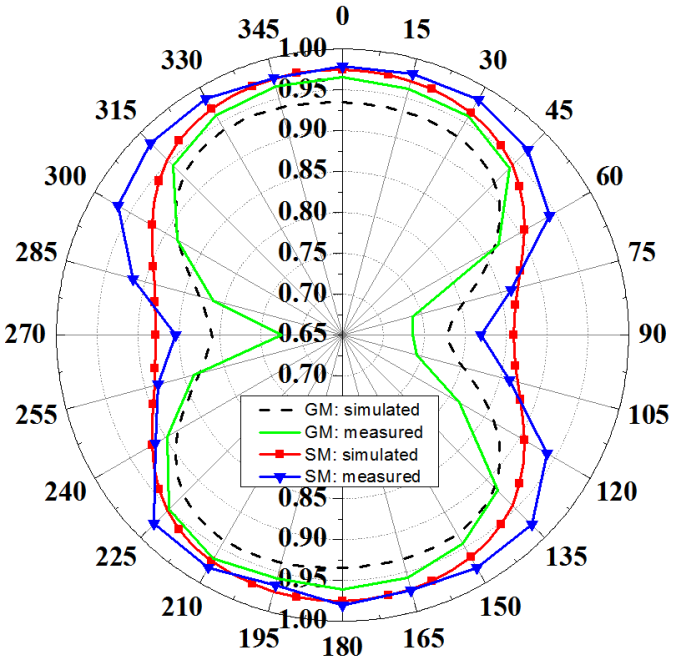

Figure 5-17: Measured and simulated Fidelity Factor for monopole GM and monopole SM with an equalized modulated SRRC excitation pulse

5.5. Conclusion

This chapter demonstrated that the time-domain performance of an antenna can be optimized according to the type of UWB pulse used. Two novel monopoles were designed using GA based optimisation techniques using Gaussian and SRRC pulses as excitation signals. To deal with the complexity of the antenna geometry, a broad search landscape was initiated during the optimisation process while computation time saving methods were implemented. Excellent time-domain performances were achieved, with a FF $\geq$ 93.5% and better for the full 3.1 to 10.6 GHz range. Furthermore the optimized antennas achieved good matching and radiation patterns, throughout the full FCC UWB frequency range. Moreover, by assessing the time-domain performance of the antenna with pulses having a third of the FCC bandwidth, it has been demonstrated that SRRC optimised antennas achieved better time-domain performances than Gaussian optimised antennas.

CHAPTER 6: DIFFERENTIALLY-FED UWB ANTENNAS

All the antennas shown in the previous chapters are monopole-like antennas. While these are suitable for most applications, they need a balanced to unbalanced transformer (BALUN), when connected to the differential IC output. The introduction of the balun will likely cause losses and dispersion in both transmission and reception mode, impairing the accuracy and range of the overall system. Unlike monopole antennas, balanced antennas, such as dipoles or slot antenna can be differentially fed making their integration into the system more straightforward.

This chapter will present several differentially fed antennas. In the first section the design of a differentially fed balanced dipole is introduced. This antenna was optimised using a SRRC excitation signal for minimum dispersion. Its spectral and time-domain performances are presented and compared with a dipole optimised with a modulated Gaussian like excitation signal. The second section will present the design of a novel differentially fed slot antenna presenting interesting characteristics compared to dipole like antennas. Finally the third and fourth sections focus on the miniaturisation and performance improvement of the antenna presented in the second section.

6.1. Differentially Fed Balanced Dipole Antennas

6.1.1. Geometry and Optimisation

In this section the dipole antennas were optimised for wide-band performance and pulse fidelity, using a SRRC excitation signal for the *SRRC* dipole *(SD)* and a modulated Gaussian like excitation signal for the *Gaussian* dipole *(GD)* shown in Figure 6-1 and Figure 6-2 respectively. Antennas *GD* and *SD*, shown in Figure 6-3 and Figure 6-4, are planar dipole-like with a balanced microstrip feed arrangement which requires a small ground plane. They consist of two identical dipole arms (defined by 4 spline points) fed with 50 Ω dual mitred microstrip lines and a mirrored splined ground plane (4 points). The spline points for the radiators have two degrees of freedom (X and Z-axis), while the spline points for the ground plane are restricted to one degree of freedom (Z-axis) in order to limit the complexity of the problem.

Both antennas were fabricated on a 40 × 40 × 0.7 mm FR4 double-sided laminate with a dielectric constant $\varepsilon_r = 4.3$ and loss tangent = 0.02. The antennas were initially performance-optimized without SMA connectors but the simulation model included the connectors to allow a fair comparison between measurement and simulation.

The antennas were optimised for best fidelity factor between the excitation signal derivative and the radiated signal. The optimisation process used was similar to that presented in Section 5.2.The antenna dimensional constraints, defined in millimetres, are shown in Table 6-1.

$P_{1,2,3,4}(z) = 5 < z < 26$
$P_5(x) = 0 < x < 4$
$P_5(z) = P_4 < z < 40$
$P_{6,7,8}(x) = 10 < x < 20$
$P_{6,7,8}(z) = P_5 < z < 40$
$G_1 = 1 < x < 5$
$G_2 = 0 < z < 5$

Table 6-1: Dipole antennas dimensional constraints (mm)

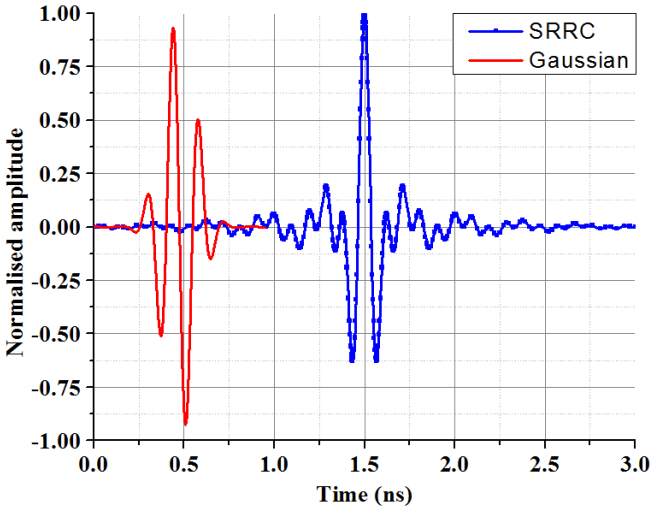

Figure 6-1: Modulated Gaussian and SRRC pulses

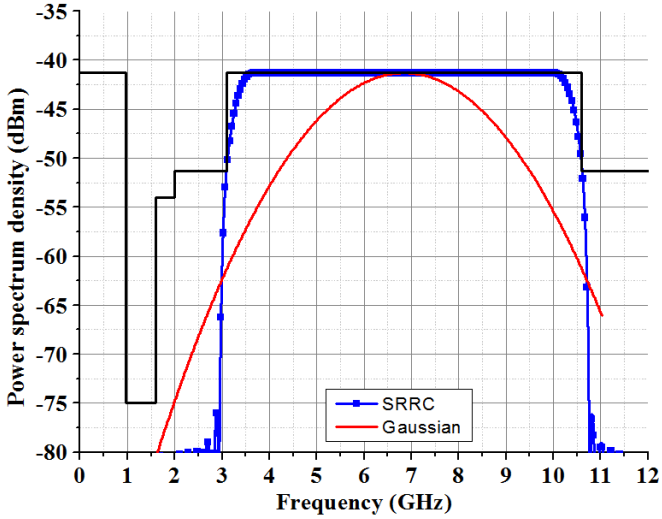

Figure 6-2: Power spectrum density of Gaussian and SRRC pulses with the IEEE 802.15.4 spectrum mask for indoor use

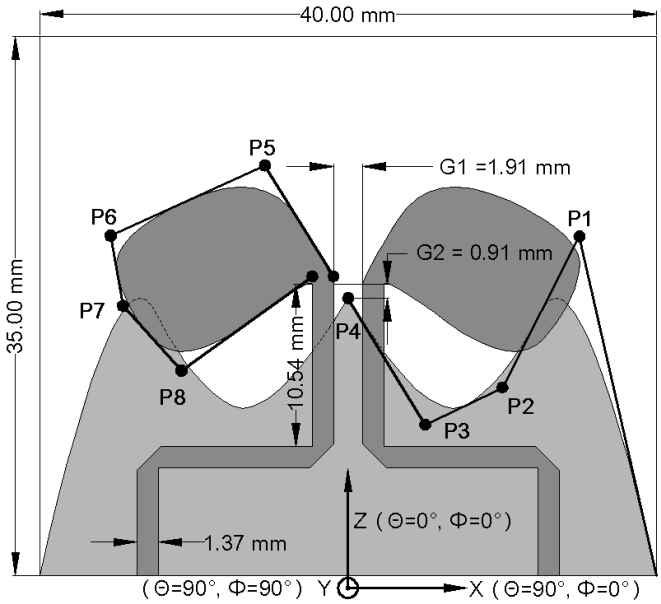

Figure 6-3: Gaussian dipole *GD* geometry and coordinate system

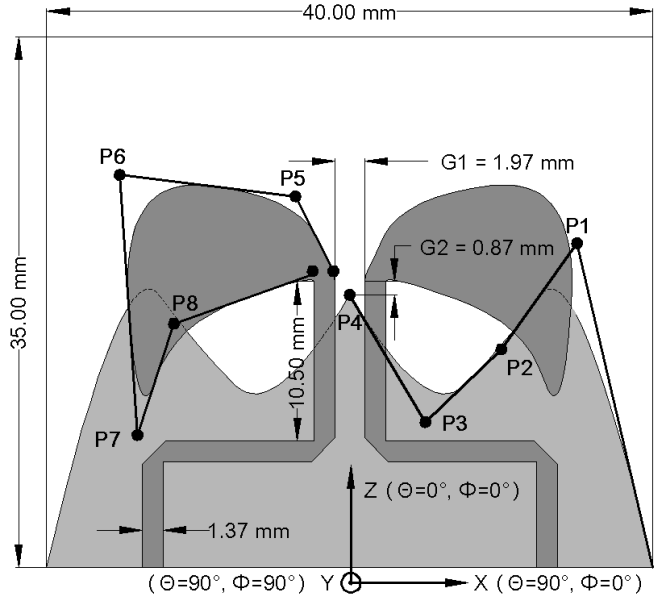

Figure 6-4: SRRC dipole *SD* geometry and coordinate system

For time-domain optimisation, farfield electric field probes were located at 30 cm from the dipole and configured in 5° steps along $\varphi = 90°$, $-90° \leq \theta \leq 90°$ half plane. The multi-objective cost function used for the dipole antenna geometries optimisation was the same as in Section 5.2, excepted that Γ corresponds to the differential input reflection coefficient S_{dd}

6.1.2. Frequency-domain Results

6.1.2.1. Return Loss

The measured and simulated S_{11} are shown in Figure 6-5. It is seen that dipole *GD* and *SD* achieve a measured 8 dB bandwidth across 2.75 GHz - 10.6 GHz and 2.9 - 13.8 GHz, respectively. Both antennas exhibit good matching across the UWB frequency range with good agreement between simulation and measurement.

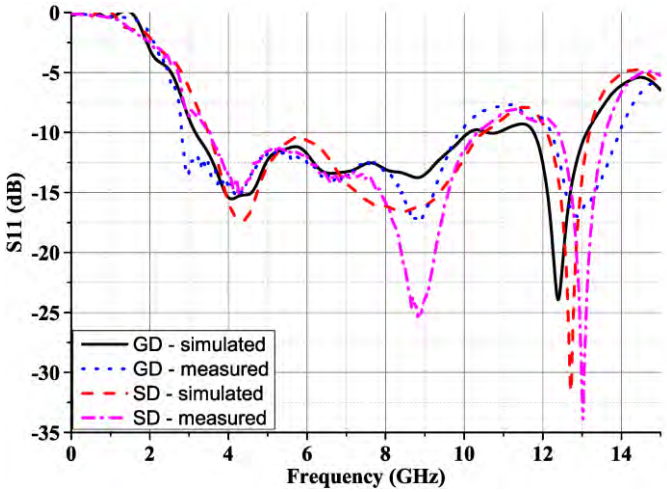

Figure 6-5: S_{11} for dipole *GD* and *SD*

6.1.2.2. Radiation Pattern

The dipole radiation patterns were measured in the H-plane (Z-Y plane) which covers the direction of main radiation. The frequency-domain measurements were made using a two port Rohde & Schwarz ZVA24 VNA, which required the use of Equation (2.14) [28] described in Section 2.1.5. By inputting the radiation pattern of the dipole with each port individually excited to Equation (2.14), the measured radiation pattern of the dipole operating in differential mode can be achieved, using a two port VNA.

As seen in Figure 6-6 and Figure 6-7, the dipoles show a good stability in their radiation pattern across the 3.1 - 10.6 GHz. The dipoles achieve an average co-polar realized gain of 0.27 dBi (std. dev. = 2.45) and 0.8 dBi (std. dev. = 2.47)

respectively. Regarding their maximum gain dipole *GD* achieved a gain of 6.4 dBi (θ, φ = 90°, 55°) at 8.88 GHz, while dipole *SD* had the maximum gain of 6.87 dBi (θ, φ = 90°, 60°) at 9.4 GHz.

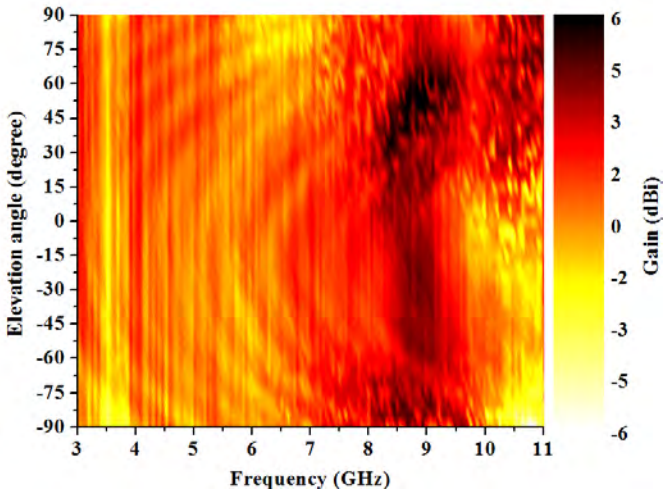

Figure 6-6: Measured dipole *GD* radiation pattern in the φ =90° plane

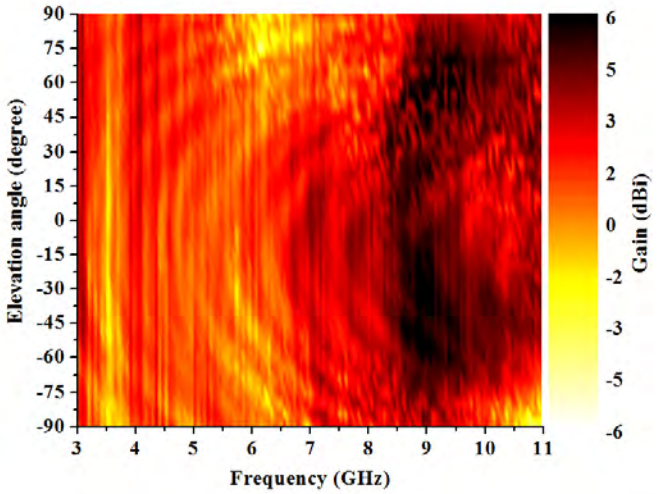

Figure 6-7: Measured dipole *SD* radiation pattern in the φ =90° plane

6.1.3. Time-domain Results

The antenna under test was operating in transmitting mode and rotated through 15° angle steps in the radiation plane. The time-domain measurement setup was similar to the one described in Section 5.4 with the exception that a UWB out of phase power divider [66], optimised for our needs, was connected between the UWB amplifier and the AUT as shown in Figure 6-8. The excitation signal, generated by

the AWG, was equalised in order to take account of the losses introduced by the transmit network, thereby feeding the antennas with a signal having a quasi-constant energy level across the UWB frequency range.

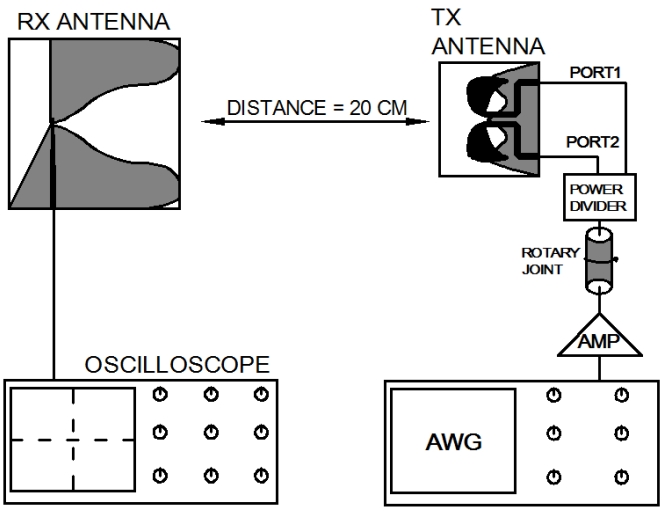

Figure 6-8: Time-domain measurement setup for differentially fed antennas

Finally the receive network impulse response, which includes the receiving antenna and the cables and connectors, was de-embedded from the received signal as shown in Section 5.4.4, allowing an efficient characterisation of the time-domain performance of the AUT

The measured signals were averaged over 64 samples, increasing the repeatability of measurement and cross-correlated with the derivative of the input signal received at the port of the AUT. From these results, the measured fidelity factor was calculated for each recorded signal, allowing an accurate comparison with simulated results. Figure 6-9 and Figure 6-10 show the measured radiated pulse at boresight for dipole *GD* and *SD*, compared with the simulated radiated E-field recorded at the same orientation. It is seen that the radiated signals from the dipoles are in excellent agreement with the simulation. Figure 6-11 represents the normalised PSD of the measured radiated signals at boresight for the dipoles and the derivative of the signal fed to the antenna ports. It seen that the PSD of the signal radiated by

the dipole *SD* is in better agreement with the derivative of the excitation signal than the one from dipole *GD*. This translates to a better FF for dipole *SD* at boresight as shown in Figure 6-12. It is also seen in Figure 6-12 that the agreement between simulation and measurement is acceptable around the φ =90° plane except at θ, φ =90°, 195°. This disagreement is due to the proximity of the coaxial cable to the reference antenna, impairing the quality of the received signal. It is seen that from θ, φ =90°, 270° to θ, φ =90°, 90° the fidelity factor values are greater than the value from θ, φ =90°, 90° to θ, φ =90°, 270° due to the fact that the antenna was optimised for best time-domain performance in the first half plane. Nevertheless the fidelity factor values from θ, φ =90°, 90° to θ, φ =90°, 270° are of lesser importance because of the reduced rearwards gain.

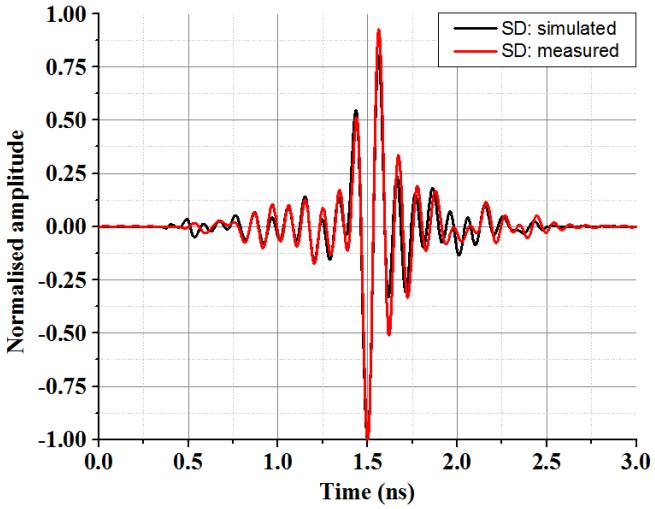

Figure 6-9: Dipole *SD* simulated and measured radiated signal at boresight

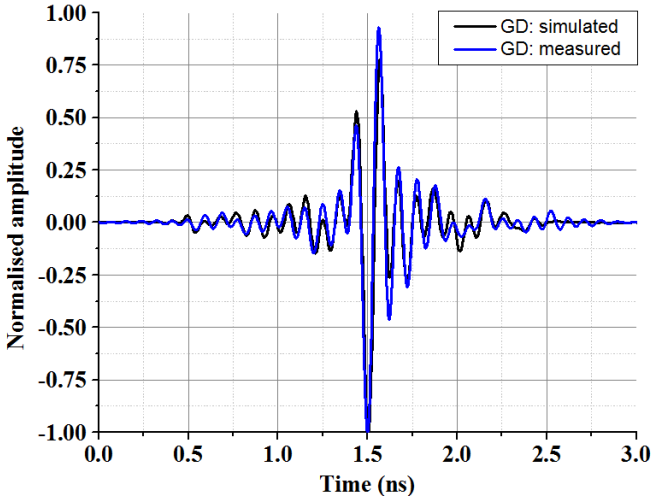

Figure 6-10: Dipole *GD* simulated and measured radiated signal at boresight

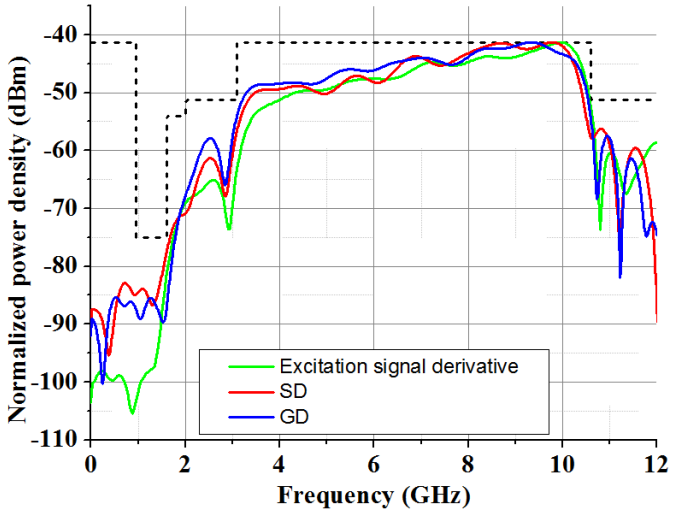

Figure 6-11: Power spectrum density of excitation signal derivative versus the measured radiated signals at boresight for dipole *GD* and *SD*

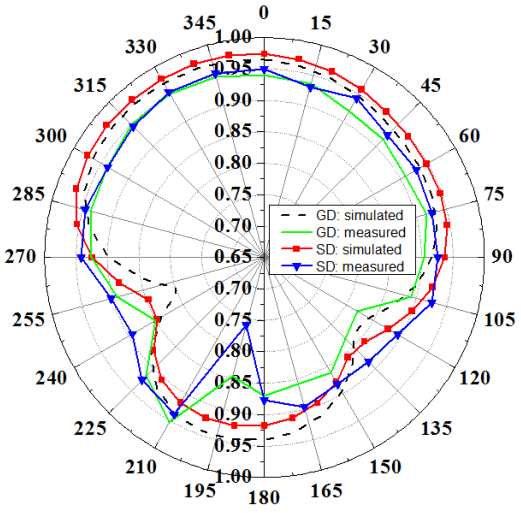

Figure 6-12: Measured and simulated Fidelity Factor for an antenna system for dipole *GD* and dipole *SD* with an equalized modulated SRRC excitation pulse

6.2. Differentially Fed Slot like Antennas

The previous sections successfully show the design of planar dipole for direct integration. Naturally, balanced dipole like antennas can have their performance impaired depending on the geometrical (dimension) and electromagnetic constraints (matching, radiation pattern, polarisation, etc…).

The slot antenna can be an alternative choice to dipole like antenna since its geometrical shape is complementary to the dipole antenna. For a dipole and slot antenna with identical shape, their radiation patterns will be similar, but the E-field and H-field of the slot will be interchanged from the ones of the dipoles. This means that a slot mounted vertically will radiate a horizontally polarised electric field, while a dipole mounted vertically will have its electric field vertically polarised [67].

This section will introduce the design of differentially fed slot like antennas using two optimization approaches for Real Time Location System (RTLS) applications requiring vertical polarization and a reasonably omnidirectional/bidirectional pattern. The geometries are created using canonical and Bézier spline shapes. Both were designed for pulse fidelity for the full UWB range while one was refined using genetic algorithm, trust region framework algorithm and SRRC pulse.

6.2.1. Elliptical Slot Antenna

6.2.1.1. Design Geometry

The initial project was to design a balanced differentially fed antenna to be integrated to a 110 × 70 × 0.7 mm RTLS test board with a maximum antenna dimension of 40 × 70 × 0.7 mm. This antenna was required to have a 10 dB bandwidth across 3.1 GHz to 10.6 GHz while radiating a reasonably

omnidirectional/bidirectional pattern, with vertically polarised electric field. Empirical design and optimisation studies have shown that dipole like antennas were unable to comply with the requirements, due to the proximity of the circuitry and components which can be approximated as ground plane as shown on Figure 6-13.

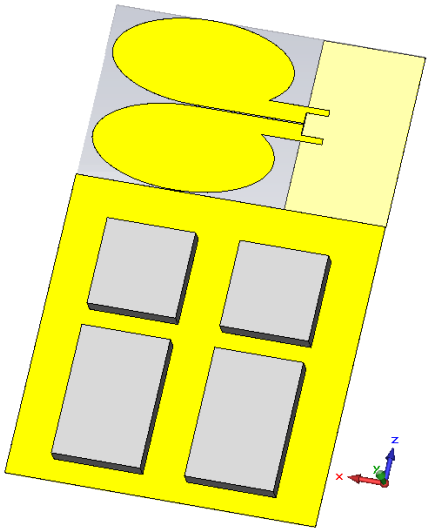

Figure 6-13: 3D model of an elliptical dipole integrated on 110 × 70 × 0.7 mm test board

To reach those objectives an elliptical slot antenna was fabricated on a 70 mm × 40 mm × 0.7 mm double copper clad FR4 PCB board as shown in Figure 6-14. The antenna geometry, optimized for time-domain performance using a conventional parameter sweep, consists of two mirrored elliptical slots connected with a rectangular microstrip-to-slot transition while being fed with 50 Ω dual mitred microstrip lines. Elliptical slots were chosen because of their non-dispersive properties [68]. The values, in millimetres, for the geometric parameters *A*, *B* and *C* are given in Table 6-2. Also virtual E-field probes were setup around the X-Y plane, providing spatial information about radiated electric fields.

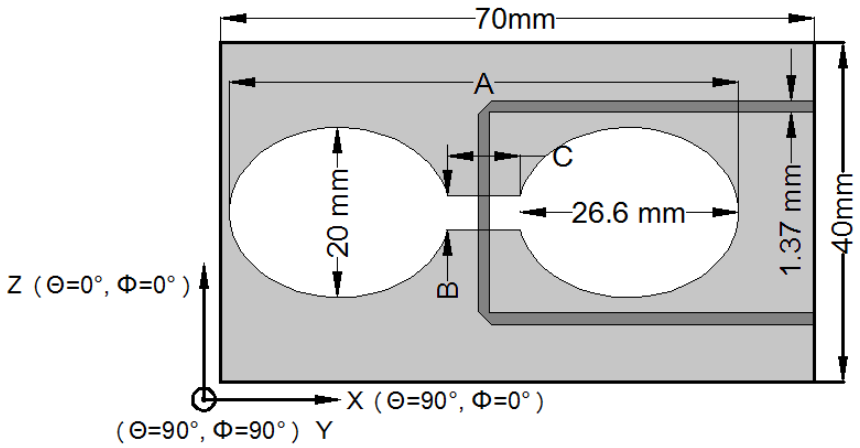

Figure 6-14: Elliptical slot geometry and dimensions

A = 60
B= 4
C= 4

Table 6-2: Elliptical slot antenna parameters (mm)

6.2.1.2. Frequency-domain Result

Figure 6-15 represents the S_{11} in terms of different values of parameters *A*, *B* and *C*. It is seen that the parameter *A* mostly determines the lowest 10 dB frequency point on the S_{11} curve, reducing the lowest 10 dB frequency point for high values of *A* and vice-versa. Parameter *B* influences the magnitude of the S_{11}, the lowest 10 dB frequency point with its optimal value being 4 mm. Parameter *C* impacts only the S_{11} overall magnitude. For high values of *C* the antenna matching improves from 2.6 GHz to 7 GHz and degrades in the higher frequency band, while from low values of *C* (up to 2 mm), the impedance is improved in the higher band and decreases and the lower band. A value of 4 mm for parameter *C* was chosen as it provides a good trade off. Figure 6-16 shows the elliptical slot measured S_{11}. As expected it is seen that the S_{11} is below −10 dB across the full UWB frequency range, with a −10 dB bandwidth starting a 2.98 GHz.

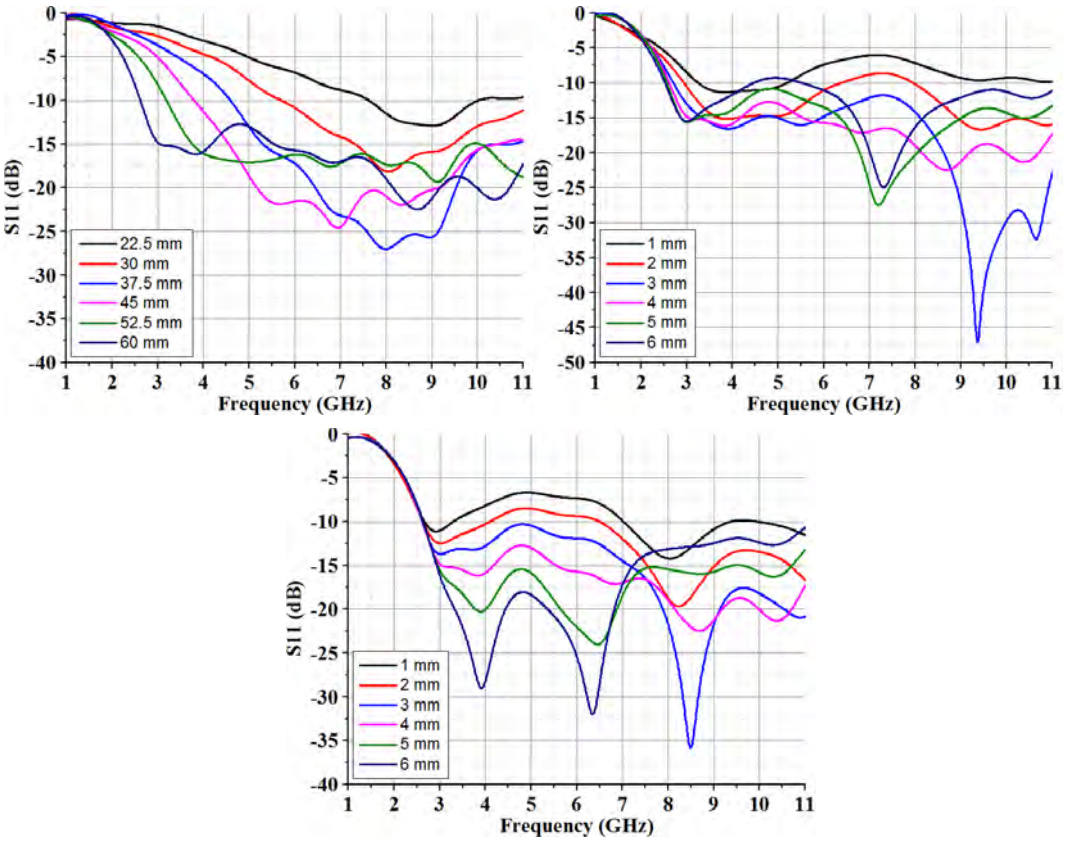

Figure 6-15: S_{11} for different parameter sweeps; *A* (left), *B* (Right), *C* (centre)

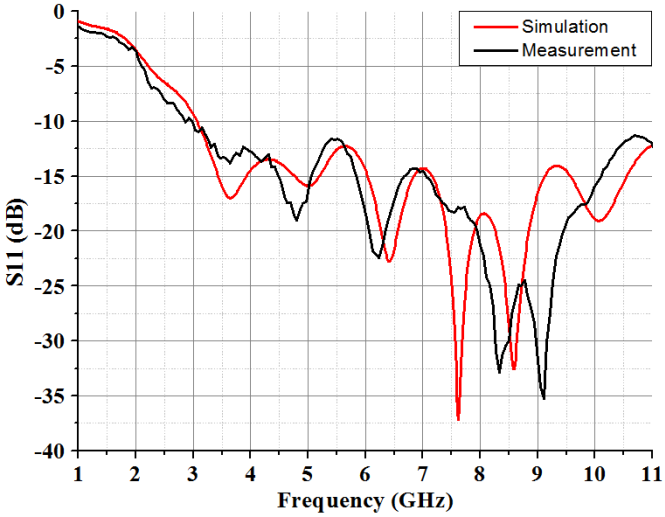

Figure 6-16: Elliptical slot measured and simulated S_{11}

Figure 6-17 shows clearly a bidirectional radiation pattern with its orientation approximately normal to the substrate plane up to 6 GHz. From 6 GHz to 9 GHz the radiation pattern becomes more omnidirectional with a peak value located at θ, φ = 90°, 115° for 8.88 GHz. The maximum gain is equal to 7 dBi while the average

azimuthal gain from 3 GHz to 11 GHz is equal to −1.94 dBi. The simulated value for the average (total) radiation efficiency over the UWB band was ≈66%.

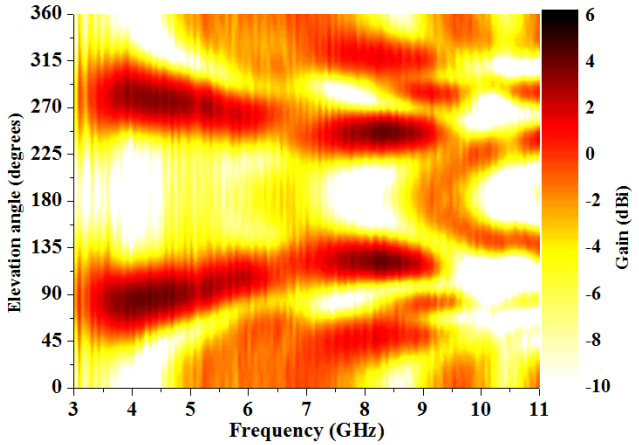

Figure 6-17: Measured elliptical radiation pattern in the φ =90° plane

6.2.1.3. Time-domain Results

The configuration setup used to characterise this antenna was identical to the one described in Section 6.1.3 and a SRRC signal was used to excite the antenna. Figure 6-18 represents the measured fidelity factor in the φ =90° plane, taking as reference signal the input signal at the antenna port and also the first derivative of this signal. It is seen that reasonable agreement is achieved. In the azimuth plane, the measured FF mean is equal to 89% with a minimum and maximum of 70.5% and 96.6%. The mean of the FF for the input derivative is equal to 84% with a minimum and maximum of 71% and 93.3% respectively. By analysing Figure 6-18 and Figure 6-17, it is seen that the elliptical slot tends to radiate a signal similar to the antenna excitation signal, especially in the direction of the two directional beams.

6.2.2. Optimised Open Slot Antenna

6.2.2.1. Design geometry

From the design of the elliptical slot antenna, another slot like antenna was designed and optimised using Bézier spline curves and a modulated SRRC (centred at 6.85 GHz and tailored to uniformly fit the full UWB mask) was used as excitation

pulse. The size was reduced by 36% and was fabricated on 45 mm × 40 mm × 0.7 mm double side FR4 laminate, as shown on Figure 6-19.

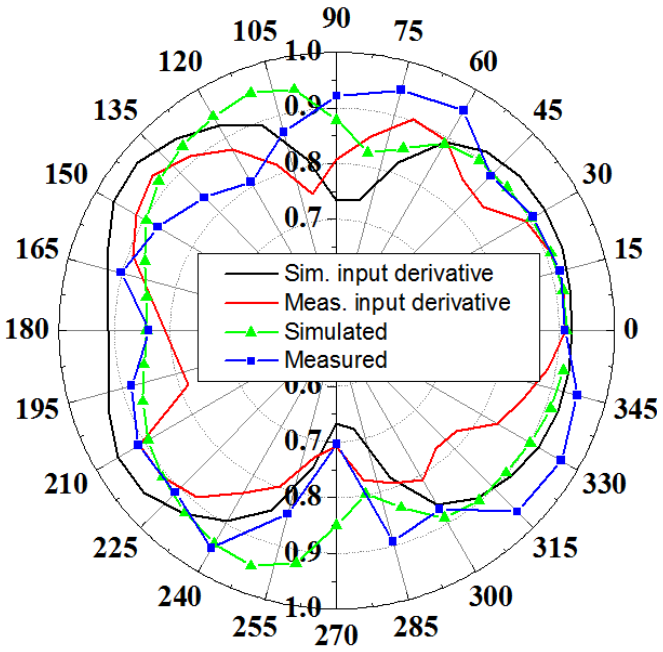

Figure 6-18: Measured fidelity factor in the φ =90° plane

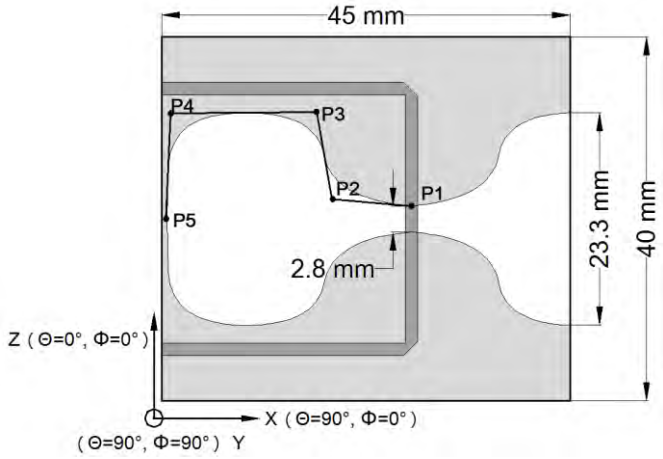

Figure 6-19: Optimised open slot antenna geometry and dimensions

The geometry consists of two mirrored 5 point spline shaped slots. Except for P1 and P5, each point had two degrees of freedom (X-Z plane). P1 and P5 have only degree of freedom because they both are in the symmetry axes. The geometry of the antenna was optimized with the MATLAB genetic algorithm for global optimization,

using the same configuration setup defined in Chapter 5, and refined through a Trust Region Framework (TRF) algorithm from the CST Microwave Studio package. The latter algorithm is very efficient for narrow search landscapes or pre-optimised problems and will optimise the parameters option towards their global optimal value, if the GA solution is not optimal. The multi-objective goal consists of two weighted cost functions taking account of the least matched magnitude in the S_{11} and the FF average in the plane of interest as indicated in Equations (5.1) and (5.2) in Section 5.2. The search landscape, show on Figure 6-20, indicates that a broad random search was done on the initial population, consisting of 750 individuals, reducing the probability of the GA to be stuck in local optima.

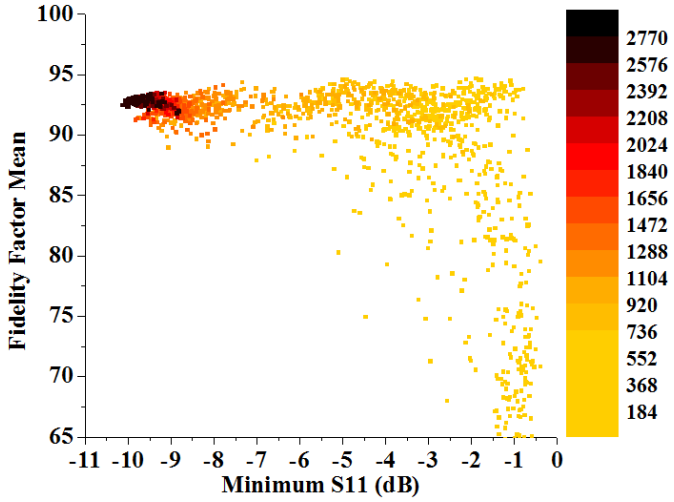

Figure 6-20: Genetic Algorithm optimisation search landscape for the optimised open slot antenna

6.2.2.2. Frequency-domain Result

From Figure 6-21, it is seen that the antenna exhibits a good impedance matching across the UWB frequency range, achieving a 10 dB bandwidth of 7.68 GHz starting from 2.52 GHz up to 10.2 GHz. The differential S_{11} is above −10 dB from 10.2 GHz due to the slight mismatch induced by the SMA connectors required for measurement purposes.

The differential mode radiation pattern was measured using the procedure described in Section 2.1.5 .The antenna shows a bidirectional radiation pattern with the two main lobes quasi-perpendicular to the substrate as seen in Figure 6-22. The antenna achieved an average gain of −2.83 dBi in Y-Z plane with a maximum gain of 5.26 dBi at θ, φ=90°, 260° at a frequency of 6.87 GHz. From 8 to 9 GHz the radiation pattern becomes omnidirectional, with an average gain of 0.39 dBi and a maximum and minimum gain of 4.56 dBi and −6.1 dBi respectively.

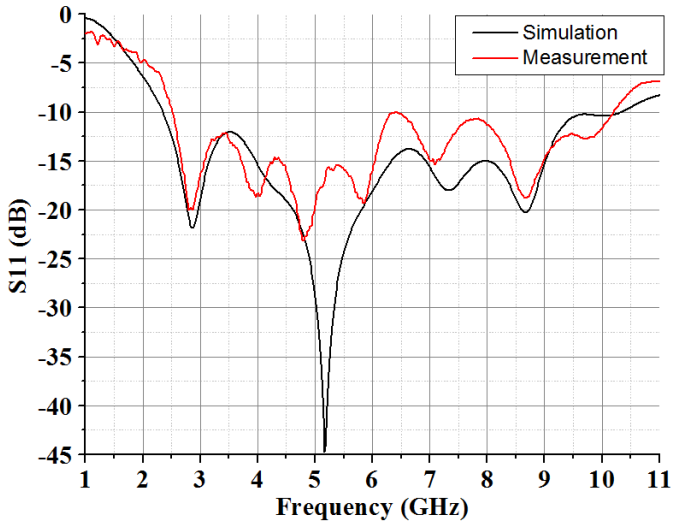

Figure 6-21: Optimised slot like antenna measured and simulated differential S_{11}

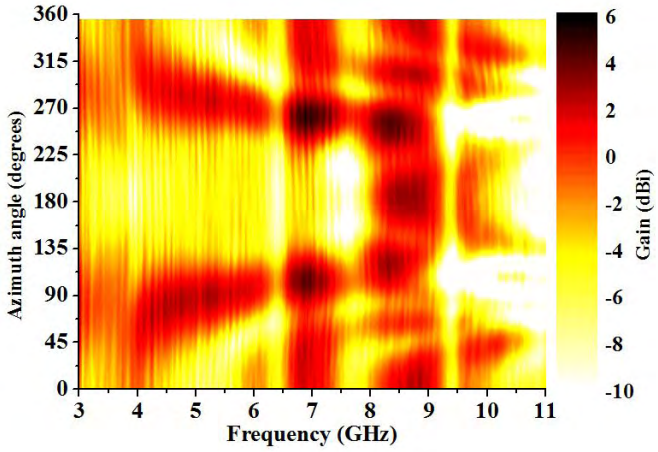

Figure 6-22: Measured optimised slot like antenna radiation pattern in the φ =90° plane

6.2.2.3. Time-domain Results

At the time of this study, no AWG was available to generate the SRRC signal, thus only simulated results are presented in this section.

Virtual farfield E-field probes were setup around the antenna on the Y-Z plane at 10° steps and at a distance of 300 mm while the antenna was excited using a modulated SRRC signal with a bandwidth of 7.5 GHz centred at 6.85 GHz. The fidelity factor was calculated by cross-correlating the captured electric field and the excitation signal or the first derivative of the latter. The antenna achieved an average FF of 0.91 with a minimum and maximum of 87.5 % and 96.3% respectively.

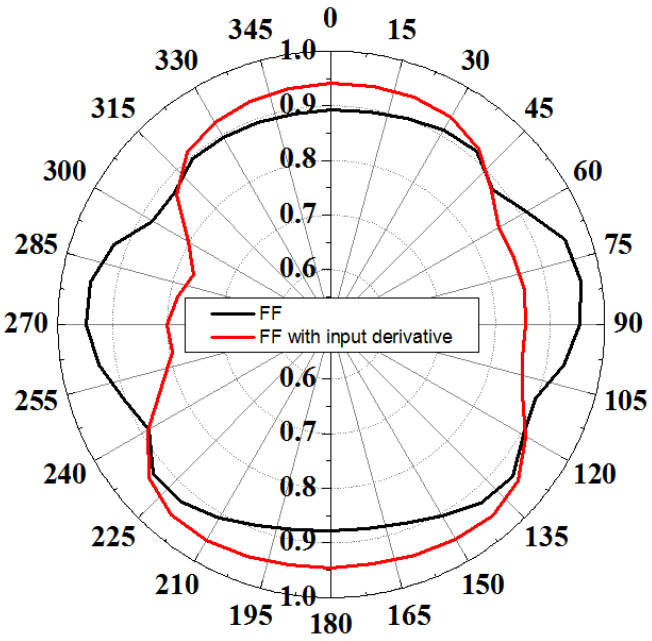

Figure 6-23: Optimised open slot fidelity factor

From the analysis of Figure 6-23, it is seen that the antenna has an omnidirectional FF and radiates excellent replicas of the excitation signal around θ, φ=90°, 90° and θ, φ=90°, 270°, which corresponds to the direction of the main beams seen in the radiation pattern plot (Figure 6-22). From a RF systems point of view, and assuming the receiving antenna is not dispersive, the cross analysis of Figure 6-22 and Figure 6-23 is important because it indicates that at the receiving

end the system should expect a signal similar to the signal fed to the open slot antenna (transmitting antenna), since most of the power is radiated around θ, φ=90°, 90° and θ, φ=90°, 270°.

6.3. Conclusion

This section described the time-domain performance optimisation of differentially-fed dipole and slot-like antennas for direct connection to the chip output. Antennas were fed with out-of-phase signals at their ports and exhibit good matching when operating in differential mode. Furthermore the differential gain of these antennas was characterised using a method based on the superposition principle and by measuring the gain when the antennas were excited at one port only. Measurement results show a stable gain throughout the full UWB frequency range whilst displaying excellent time-domain performances from θ, φ =90°, 270° to θ, φ=90°, 90°.

Unlike the dipole antennas, differentially fed slot-like antennas are shown to be a good alternative when vertical polarisation in constrained geometries is required with good frequency-domain performance. These antennas achieve a quasi-full UWB bandwidth (7.5 GHz), while being in proximity to the circuitry and components of a 110 × 70 × 0.7mm test board. Also it has been shown that in the direction of their main beams, these slot-like antennas radiate a signal that resembles the replica of the excitation signal, which is important for RF system designers.

Finally it was shown that the dipole and slot-like antennas optimised with SRRC as excitation signal outperform antennas optimised with excitation signal with non-constant energy levels, proving that the optimisation technique presented in Chapter 5 is efficient regardless of the type of antennas.

CHAPTER 7: CONCLUSION

A number of new and existing technologies were described, adapted and enhanced in this thesis. Time-domain and spectral characterisation was carried out on several types of signals and it was shown that signals with optimal fit to the UWB spectrum mask can be generated. The frequency- and time-domain performances of monopole antennas in close proximity to metallic surfaces were evaluated. A novel antenna optimisation method based on Bézier spline curves, genetic algorithms and SRRC signal was developed for improved antenna transient performance. An improved method of time-domain measurements was also implemented allowing a comparison of measurement and simulation results. Finally differentially fed dipole and slot antennas were designed for direct integration onto PCBs with integrated circuit UWB technology and optimised for best time-domain performance.

A study of UWB signals was carried out as the starting point of this investigation. It was shown that the temporal signal shape has a significant effect on the spectrum making it ultimately non-compliant to standard regulation. Also it was shown that the transmission and reception of UWB signals differ from the radiation and reception of narrowband signals due to the time derivative occurring between the impulse response of the antenna operating in transmitting and receiving mode. From this analysis it was demonstrated that the radiated signal is not only dependent on the observation point but also on the impulse response of the transmitting antenna.

The effect of a planar conductor in proximity to a UWB monopole was studied. The spline based monopole was optimised for bandwidth and time-domain

performance from band 1 to band 7 (in UWB MB-OFDM spectrum allocation), resulting in a measured antenna system fidelity factor of 99.8%. It was shown that an antenna-reflector separation between a wavelength and half of a wavelength significantly impaired the antenna time-domain and spectral performance due to formation of side lobes in the radiation pattern. At the contrary, for an antenna-reflector separation of a quarter wavelength, the antenna becomes significantly more directive, while its time-domain performance, in the main beam direction, remains comparable to the transient performance in free space. It was also shown that the time-domain option capability of VNAs is inefficient in providing direct time-domain characterisation of the antenna under test, due to the dependency on the type windowing function and frequency span used in the measurements.

The integration of UWB antennas for commercial asset tracking tag applications was demonstrated. In this case, the antenna needed to achieve a −6 dB bandwidth on channel 4 and channel 7, and a total radiation efficiency of greater than 50%, while being in close proximity to IC components, dielectric and conductive materials. In order to reduce the complexity of the problem the 3D model was simplified dividing the computational size by 3. An evolutionary global optimisation was used to optimise the geometry and antenna performance. The optimised antenna impulse response was characterised using SRRC signals with different bandwidths. It demonstrates that the ability of an antenna to transmit distortionless pulses is also dependent on the excitation signal bandwidth.

Two novel monopole antennas were designed to radiate distortion less signals. They were designed using the combination of a genetic algorithm based techniques and modulated Gaussian or SRRC excitation signals. An initial broad search landscape was used while computation time saving techniques were implemented.

Both antennas have shown excellent spectral and time-domain performance with FF $\geq$ 93.5% for a signal having a full UWB bandwidth (7.5 GHz). Also, the study has shown that a monopole antenna optimised with a excitation signal having a constant energy level will have significantly better overall time-domain performance than antennas optimised with Gaussian like excitation signals, proving that use of SRRC signals can enhance the time characterisation of antennas. Time-domain measurements were carried out, using a pulse equalisation and reference antenna de-embedding allowing a direct comparison between simulated and measured results.

Novel differentially fed balanced dipole and slot like antennas were designed for direct integration to the chip output. The differential mode impedance matching and radiation pattern of these antennas were characterised using the superposition principle and a two port VNA. Both types of antennas exhibit a stable gain in the direction of their main beams across the UWB frequency range. The SRRC optimised dipole shows excellent time-domain performance with a measured average FF of 93.2 % from θ, φ =90°, 270° to θ, φ =90°, 90°.

In the case of conductive surface proximity and polarisation issues, differentially fed slot like antennas appear to be a good alternative to dipole antennas. In that respect two novel slot antennas were designed and optimised using SRRC optimisation techniques and both exhibit a −10 dB bandwidth across the UWB frequency range. It was also demonstrated that the best FF is achieved in the direction of their main beam, indicating that these slot antennas radiated a replica of the excitation signal.

CHAPTER 8: FUTURE WORK

During the development of this thesis, several research topics and potential improvements were identified.

Increased demand for localisation systems with improved accuracy and range is creating the need for reconfigurable antennas for time-domain performance. Reconfigurable S_{11} and radiation patterns enable selective antenna filtering of unwanted frequencies and bands, direction changing of the main beam or improved impulse response in particular directions [69] [70]. Possible reconfigurable approaches could include combining several antennas having different characteristics into a single antenna. Each active part of the antenna could be control by using PIN diodes, phase shifters or Micro-Electromechanical system (MEMS) [71] [72]. Another solution would be to use antennas with multiple tuneable elements such as a UWB array or reflect array antenna. The latter antenna type has the advantage of having a high directivity and could be used to provide improved point to point connection by steering the main beam in the direction of the received signal, improving the range, accuracy and battery life of the system.

Possible future research efforts should also focus on the study of circularly polarised antennas optimised for time-domain performance, in contrast to the linearly polarised antennas designed in this thesis. It was shown in Chapter 6, that the radiated and received signal polarisation is an important criterion for radio systems. However RTLS devices such as UWB RFID tags are often oriented in a random manner, which can degrade the system performance due to polarisation mismatch loss. This problem can be solved by using time-domain optimised UWB

circularly polarised antennas. Although UWB circularly-polarised antennas have been reported [73] [74] [75], there is significant variation in the axial-ratio across the wide bandwidth and very little has been reported on the impulse response. A circularly-polarised antenna with good axial-ratio and impulse response enable UWB RTLS systems to achieve a high level of accuracy independent of the radiated-received signal polarisation. Combining these two characteristics is a very challenging topic and is highly relevant from an industrial and academic point of view. Time-domain optimised circularly-polarised antennas could initially be applied in the anchor devices of RTLS systems, whereas the antenna integrated in tag could be linearly polarised. Using this configuration the system accuracy would be more independent of tag orientation.

Further investigation on the miniaturisation and resilience to proximity de-tuning for UWB antennas should be carried out. In Chapter 6, it was shown that by using a Bézier spline, good time-domain performance can be realised even for very small antennas. By designing antennas to operate in the ECC UWB 6 GHz to 9 GHz band and because of the smaller bandwidth used, antennas operating in this frequency range will be significantly smaller, with antenna surface area less than 1 $cm^{2.}$ This will allow the antenna to be applied in systems such as compact UWB RFID tags or body-worn RTLS systems. However for such small antenna the ground plane size becomes critical and a study on ground plane miniaturisation must be undertaken. These studies are of the outmost importance since miniaturisation is an extremely important topic for the industry and will eventually lead to patents and commercialisation of antenna solutions.

Chapter 4 has shown that antennas are subject to detuning when in close proximity to conductors or dielectrics. Also previous work [76] [77] shows that

when a free space optimised antenna is placed near body tissue, its S_{11}, radiation efficiency and impulse response are degraded, impairing the radiated or received signals and therefore degrading the system accuracy. Therefore, a study on the improvement of antenna resilience to de-tuning due to body proximity will be of great benefit, especially for time-domain optimised UWB body-worn devices.

UWB antennas array have demonstrated a great potential in the field of imaging [78]. Since UWB imaging systems and radar are pulse based systems, an investigation on the performance of through-wall and body imaging using time-domain optimised UWB array antennas fed with SRRC signal should be made. This investigation involves the design of a time-domain optimised antenna array where the coupling between each element must be considered and optimised in order to maximise the directivity of the radiation pattern. A study of the geometry of each of the antenna elements and the feeding structure will have to be done to characterise their effects on the antenna impulse response.

For array elements, is critical and will have to be optimised to reduce the mismatch loss and to improve the impulse response of the array. UWB array antennas could be optimised for farfield imaging applications, such as through-wall imaging or ground penetrating radar, or for near field imaging application [79] such as body imaging. For the latter application, the study of the antenna in a coupling medium is important since it acts as a transitional layer between the antenna and the skin of the body. Finally, an investigation could be carried out on the imaging system performance improvement when using a UWB SRRC waveform compared to other signals.

The optimisation technique reported in this thesis is a key enabling method for antenna operating in the FCC UWB. Electronic manufacturers are more and more

interested in the millimetre wave range especially above 60 GHz. At this frequency the antenna size becomes very small, and substrates exhibit increases losses, making the design tolerance more critical. An investigation could be undertaken to determine if the optimisation process described in this thesis, is relevant for UWB millimetre wave antenna. Due to the specific constraints of millimetre wave antenna, a new optimisation technique could be derived to enable the design of high performance UWB millimetre antenna that would have been impossible to achieve using traditional optimisation technique. Furthermore by using a SRRC excitation signal, it would allow the creation of antennas with best-in-class time-domain performance.

Bibliography

[1] J. C. Maxwell, "A dynamical theory of the electromagnetic field," *Philosophical Transactions of the Royal Society of London,* vol. 155, pp. 459-512, 1865.

[2] Wikipedia, "Wikipedia, The Free Encyclopedia," Wikimedia Foundation Inc, 24 April 2012. [Online]. Available: http://en.wikipedia.org/wiki/Oliver_Heaviside. [Accessed 10 May 2012].

[3] C. A. Balanis, "Historical advancement," in *Antenna Theory, Analysis and Design, Third Edition*, Hoboken, John Wiley & Sons, Inc., 2005, p. 20.

[4] T. W. Barret, "History of Ultra Wideband Communication and Radar: Part I, UWB," *Microwave Journal,* pp. 22-54, January 2001.

[5] "Micropower Impulse Radar," *Science & Technology Review,* pp. 17-29, January 1996.

[6] K. Mandke, H. Nam, L. Yerramneni and C. Zuniga, "The Evolution of UWB and IEEE 802.15.3a for Very High Data Rate WPAN," 06 May 2003. [Online]. Available: http://kom.aau.dk/group/03gr993/Papers/802.15/GT3a.pdf. [Accessed 05 May 2012].

[7] M. Carr, "Testing WiMedia UWB," TEST & MEASUREMENT WORLD, 2009.

[8] IEEE Computer Society, "Part 15.4: Low-Rate Wireless Personal Area Networks (LR-WPANS)," IEEE, New York, 2011.

[9] B. Allen, M. Dohler, E. E. Okon, W. Q. Malik, A. K. Brown and J. D. Edwards, "Introductions to UWB Signals and Systems," in *Ultra-wideband Antennas and Propagation for Communication Radar and Imaging*, Chichester, John Wiley & Sons Ltd, 2007, p. 5.

[10] Electronic Communications Committee, "ECC Decision of 30 March 2007 on specific Material Sensing devices using Ultra-Wideband (UWB) technology," Electronic Communications Committee, 2007.

[11] H. Nikookar and R. Prasad, "UWB Regulation," in *Introduction to Ultra Wideband for Wireless Communication*, Springer, 2009, pp. 163-171.

[12] J. L. Volakis, Antenna Engineering Handbook, New York: McGraw-Hill, 2007.

[13] Z. N. Chen, M. J. Ammann, X. Qing, X. H. Wu, T. S. See and A. Cai, "Planar Antennas," *IEEE Microwave Magazine,* pp. 63-73, December 2006.

[14] K. Bahadori and Y. Rahmat-Samii, "A Miniaturized Elliptic-Card UWB Antenna With WLAN Band Rejection forWireless Communications," *IEEE Transactions on Antennas and propagation,* vol. 55, no. 11, pp. 3326-3332, 2007.

[15] S. Honda, M. Ito, H. Seki and Y. Jinbo, "A disk monopole antenna with 1:8 impedance bandwidth and omnidirectional radiation pattern," in *International Symposium on Antennas and Propagation*, Japan, 1992.

[16] J. Evans and M. Ammann, "Planar trapezoidal and pentagonal monopoles with impedance bandwidths in excess of 10:1," in *IEEE International Symposium on Antennas and Propagation*, Orlando, 1999.

[17] C. A. Balanis, "Fundamental limits of electrically small antennas," in *Antenna Theory, Analysis and Design, Third Edition*, Hoboken, John Wiley & Sons, Inc., 2005, p. 641.

[18] M. John and M. J. Ammann, "Spline-based Geometry for Printed Monopole Antennas," *Electronics Letters,* vol. 43, no. 6, pp. 317-319, 2007.

[19] H. Prautzch, W. Boehm and M. Paluszny, Bézier and B-Spline Techniques, Berlin: Springer-Verlag, 2002.

[20] H. Muhlenbein, D. Schomisch and J. Born, "The parallel genetic algorithm as function optimiser," *Parallel Computing,* vol. 17, no. 6-7, pp. 619-632, September 1991.

[21] M. Johnston, "An evolutionary algorithm approach to multi-objective scheduling of space network communications," *Intelligent automation and Soft Computing,* vol. 14, no. 3, pp. 367-376, 2008.

[22] N. Telzhensky and Y. Leviatan, "Novel Method of UWB Antenna Optimization for Specified Input Signal Forms by Means of Genetic Algorithm," *IEEE Transactions on Antennas and Propagation,* vol. 54, no. 8, pp. 2216-2225, August 2006.

[23] S. Radiom, H. Aliakbarian, G. Vandenbosch and G. Gielen, "Optimised small-size tapered monopole antenna for pulsed ultra-wideband applications designed by a genetic algorithm," *IET Microwaves, Antennas & Propagation,* vol. 3, no. 4, pp. 663-672, May 2009.

[24] S. Chamaani, S. Mirtaheri and M. Abrishamian, "Improvement of Time and Frequency Domain Performance of Antipodal Vivaldi Antenna Using Multi-Objective Particle Swarm Optimisation," *IEEE Transactions on Antennas and Propagation,* vol. 59, no. 5, pp. 1738-1742, May 2011.

[25] MathWorks, "MATLAB," The MathWorks, Inc, 08 May 2012. [Online]. Available: http://www.mathworks.co.uk/products/matlab. [Accessed 08 May 2012].

[26] "CST Microwave Studio," Computer Simulation Technology GmbH, 08 May 2012. [Online]. Available: www.cst.com. [Accessed 08 May 2012].

[27] D. M. Pozar, Microwave Engineering, Boston: Addison Wesley, 1990.

[28] R. Bourboutian, P. Ciais and S. Toutain, "A novel method for measuring differential antennas radiation characteristics," *Antenna Measurement Techniques Association,* 2007.

[29] P.-S. Kildal, Foundations of Antennas, A Unified Approach, Lund: Studentlitteratur, 2002.

[30] Z. Chen, X. H. Wu., H. F. Li, N. Yang and M. Y. W. Chia, "Considerations for Source Pulses and Antennas in UWB Radio Systems," *IEEE Transactions on Antennas and Propagation,* vol. 52, no. 7, pp. 1739-1748, 2004.

[31] L. Babour, "ETUDE ET CONCEPTION D'ANTENNES ULTRA LARGE BANDE MINIATURISEES EN IMPULSIONNEL," Institut polytechnique de Grenoble, Grenoble, 2009.

[32] B. Scheers, M. Acheroy and A. V. Vorst, "Time-domain simulation and characterisation of TEM horns using a normalised impulse response," *IEE Proceedings Microwaves, Antennas and Propagations,* vol. 147, no. 6, pp. 463-468, 2000.

[33] E. G. Farr and C. E. Baum, "Time Domain Characterisation of Antennas with TEM Feeds," Air Force Research Laboratory, 1998.

[34] W. Sorgel and W. Wiesbeck, "Influence of the antennas on the Ultra-Wideband Transmission," *EURASIP Journal on Applied Signal Processing,* vol. 3, pp. 296-305, 2005.

[35] E. K. Miller and M. Kanda, "Time Domain Sensor and Radiators," in *Time Domain Measurement in Electromagnetics*, Van Nostrand Reinhold Company Inc., 1986, p. 125.

[36] D. H. Kwon, "Effect of Antenna Gain and Group Delay Variations on Pulse-Preserving Capabilities of Ultrawideband Antennas," *IEEE Transactions on Antennas and Propagation,* vol. 54, no. 8, pp. 2208-2215, 2006.

[37] C. A. Balanis, "Fundamental parameters of antennas," in *Antenna Theory, Analysis and Design, Third Edition*, Hoboken, John Wiley & Sons, Inc., 2005, p. 112.

[38] K. Siwiak and D. McKeown, "Generating and Transmitting UWB Signals," in *Ultra-Wideband Radio Technology*, Chichester, John Wiley & Sons Ltd, 2004, p. 62.

[39] L. Guo, J. Liang, C. C. Chiau, X. Chen, C. G. Parini and J. Yu, "Performance of UWB disc monopoles in time-domain," *IET Microwaves, Antennas and Propagation,* vol. 1, no. 4, pp. 955-959, august 2007.

[40] G. A. A. Saleeb and M. G. T. El-Kholy, "Improved Performance of a UWB Gaussian Monacycle Antenna Array," in *Seminar on Wideband Multiband Antennas and Arrays for Defence or Civil*, London, 2008.

[41] X. Zhang, L. Larson and P. M. Asbeck, "Linearity Performance of Outphasing Power Amplifier Systems," in *Design of linear RF outphasing powers amplifiers*, Norwood, Artech House, Inc., 2003, p. 47.

[42] M. Lin, Y. Zhang and Z. Zhang, "Design And Characterization of SRD-Based Comb Generator," in *Conference on Precision Electromagnetic Measurements*, Daejeon, 2012.

[43] A. T. Corp., "Comb Generators," API Technologies Corp., 2011. [Online]. Available: http://www.spectrummicrowave.com/comb_generator.aspx. [Accessed 11 May 2012].

[44] P. Protiva, J. Mrkvica and J. Machac, "A Compact Step Recovery Diode Subnanosecond Pulse Generator," *Microwave and Optical Technology Letters,* vol. 52, no. 2, pp. 438-440, 2010.

[45] C. A. Balanis, "Radiation mechanism," in *Antenna Theory, Analysis and Design, Third Edition*, Hoboken, John Wiley & Sons, Inc., 2005, p. 10.

[46] B. Allen, M. Dohler, E. E. Okon, W. Q. Malik, A. K. Brown and J. D. Edwards, "Fundamental Electromagnetic Theory," in *Ultra-wideband Antennas and Propagation for Communication Radar and Imaging*, Chichester, John Wiley & Sons Ltd, 2007, p. 27.

[47] K. Siwiak and D. McKeown, "Radiation of UWB Signals," in *Ultra-Wideband Radio Technology*, Chichester, John Wiley & Sons Ltd, 2004, p. 91.

[48] K. Siwiak and D. McKeown, "Radiation of UWB Signals," in *Ultra-Wideband Radio Technology*, Chichester, John Wiley & Sons Ltd, 2004, p. 97.

[49] W. Wiesbeck, G. Adamiuk and C. Sturm, "Basic Properties and Design Principles of UWB antennas," *Proceedings of the IEEE,* vol. 97, no. 2, pp. 372-385, 2009.

[50] C. L. Bennett and G. F. Ross, "Time-domain electromagnetics and its applications," *Proceedings of the IEEE,* vol. 66, no. 3, pp. 299-318, 1978.

[51] K. Rambabu, A. E.-C. Tan, K. K.-M. Chan and M. Y.-W. Chia, "Estimation of Antenna Effect on Ultra-Wideband Pulse Shape in Transmission and Reception," *IEEE Transactions on Electromagnetic Compatibility,* vol. 51, no. 3, pp. 604-610, 2009.

[52] D. Ghosh, A. De, M. C. Taylor, T. K. Sarkar, M. C. Wicks and E. L. Mokole, "Transmission and Reception by Ultra-Wideband (UWB) Antennas," *IEEE Antennas and Propagation Magazine,* vol. 48, no. 5, pp. 67-99, 2006.

[53] S. Curto, M. John and M. J. Ammann, "Groundplane Dependent Performance of Printed Antenna for MB-OFDM-UWB," in *IEEE 65th Vehicular Technology Conference - VTC2007-Spring*, Dublin, 2007.

[54] M. John, "Study of Design Principles and Optimisation Techniques for Ultra-Wideband Printed Antennas," Dublin Institute of Technology, Dublin, 2008.

[55] A. M. Abbosh and M. E. Bialkowski, "Design of Ultrawideband Planar Monopole Antennas of Circular and Elliptical Shape," *IEEE Transactions on Antennas and Propagation,* vol. 56, no. 1, pp. 17-23, 2008.

[56] Anritsu Corporation, "Time Domain," March 2009. [Online]. Available: http://downloadfile.anritsu.com/RefFiles/en-US/Services-Support/Downloads/Application-Notes/Application-Note/11410-00206.pdf. [Accessed 13 March 2012].

[57] Rohde&Schwarz GmbH & Co. KG, "Time Domain Measurements using Vector Network Analyser ZVR," 19 May 1998. [Online]. Available: http://www2.rohde-schwarz.com/file_6340/1ez44_0e.pdf. [Accessed 13 March 2012].

[58] C. A. Balanis, "Linear elements near or on infinite perfect conductors," in *Antenna Theory, Analysis and Design, Third Edition*, Hoboken, John Wiley & Sons, Inc., 2005, p. 201.

[59] M. Hiebel, "Time-Domain Measurements," in *Fundamentals of Vector Network Analysis*, Munchen, Rohde & Schwarz, 2008, pp. 238-239.

[60] L. Lizzi, L. Manica and A. Massa, "Time Domain Analysis for UWB Antenna Synthesis," in *European Microwave Conference*, Rome, 2009.

[61] Z. Chen, X. Qing and M. Y. W. Chia, "UWB Characteristics of Disc Cone Antenna," in *IEEE International Workshop on Antenna Technology*, Singapore, 2005.

[62] S. Chamaani, S. A. Mirtaheri and M. S. Abrishamian, "Improvement of Time and Frequency Domain Performance of Antipodal Vivaldi Antenna Using Multi-Objective Particle Swarm Optimization," *IEEE Transactions on Antennas and Propagation,* vol. 59, no. 5, pp. 1738-1742, May 2011.

[63] P. Cerny and M. Mazanek, "Optimization of Transient Response Radiation of Printed Ultra Wideband Dipole Antennas (Using Particle Swarm Optimization Method)," *Radioengineering,* vol. 16, no. 2, pp. 9-14, 2007.

[64] H. Hu, X. Sun, Z. Zheng and C. Z. W. Liu, "A novel UWB pulse design based on chirp waveform with multiband division," in *6th Conference on Artificial Intelligence on Applications and Innovations*, AYIA NAPA, 2011.

[65] Y. Duroc, A. Ghiotto, T. P. Vuong and S. Tedjini, "UWB Antennas: Systems With Transfer Function and Impulse Response," *IEEE Transactions on Antennas and Propagation,* vol. 55, no. 5, pp. 1449-1451, May 2007.

[66] A. M. Abbosh and M. E. Bialkowski, "Design of a Compact UWB Out-of-Phase Power Divider," *IEEE Microwave and Wireless Components Letters,* vol. 17, no. 4, pp. 289-291, 2007.

[67] C. A. Balanis, "Aperture antenna," in *Antenna Theory, Analysis and Design, Third Edition*, Hoboken, John Wiley & Sons, Inc., 2005, p. 700.

[68] G. Quintero and A. Skrivervik, "Analysis of Planar UWB Elliptical Dipoles Fed by a Coplanar Stripline," in *IEEE International Conference on UWB*, Hannover, 2008.

[69] D.Rodrigo, L. Jofre and B. Cetiner, "Circular Beam-Steering Reconfigurable Antenna With Liquid Metal Parasitics," *IEEE Transactions on Antennas and Propagation,* vol. 60, no. 4, pp. 1796-1802, 2012.

[70] T. Aboufoul and A. Alomainy, "Reconfigurable printed UWB circular disc monopole antenna," in *Loughborough Antennas and Propagation Conference (LAPC)*, Loughborough, 2011.

[71] S. Nikolaou, R. Bairavasubramanian, C. J. Lugo, I. Carrasquillo, D. Thompson, G. Ponchak, J. Papapolymerou and M. Tentzeris, "Pattern and frequency reconfigurable annular slot antenna using PIN diodes," *IEEE Transactions on Antennas and Propagations,* vol. 54, no. 2, pp. 439-448, 2006.

[72] J. Romeu, M.-J. Lee, S. Blanch, L. Jofre, F. De Flaviis and A. Grau, "A Dual-Linearly-Polarized MEMS-Reconfigurable Antenna for Narrowband MIMO Communication Systems," *IEEE Transactions on Antennas and Propagation,* vol. 58, no. 1, pp. 4-17, 2010.

[73] J. Pourahmadazar, C. Ghobadi, J. Nourinia, N. Felegari and H. Shirzad, "Broadband CPW-Fed Circularly Polarized Square Slot Antenna With Inverted-L Strips for UWB Applications," *IEEE Antennas and Wireless Propagation Letters,* vol. 10, pp. 369-372, 2011.

[74] X. Qing, Z. N. Chen and H. L. Chung, "Ultra-wideband Circularly Polarized Wide-slot Antenna Fed by Three-stub Hybrid Coupler," in *IEEE International Conference on Ultra-Wideband, ICUWB 2007*, Singapore, 2007.

[75] X. L. Bao and M. J. Ammann, "Printed Circularly-Polarized Antenna with Ultra-Wide Axial-Ratio Bandwidth," *IET Microwaves, Antennas & Propagation,* vol. 5, no. 9, pp. 1089-1096, 2011.

[76] R. Cooper and R. Radcliff, "The effects of a nearby biological body on the parameters of a small hand-held radio operating in the H.F. band (3MHz-30MHz)," in *Twenty-Fifth Southeastern Symposium on System Theory*, Athens, USA, 1993.

[77] Z. N. Chen, T. See and X. Qing, "Study of human body effects on received pulse characteristics by a planar UWB antenna," in *IEEE Antennas and Propagation Society International Symposium*, Honolulu, 2007.

[78] G. Charvat, L. Kempel, E. Rothwell, C. Coleman and E. Mokole, "An ultrawideband (UWB) switched-antenna-array radar imaging system," in *IEEE International Symposium on Phased Array Systems and Technology*, East Lansing, 2010.

[79] B. Yang, A. Yarovoy and L. Ligthart, "UWB stacked patch antenna design for near-field imaging radar antenna array," in *3rd European Conference on Antennas and Propagation*, Berlin, 2009.

List of Publications

Journal Publication

[JP 1] A. Dumoulin, M. John, M. J. Ammann, and P. McEvoy, "Optimized Monopole and Dipole Antennas for UWB Asset Tag Location Systems", *IEEE Transactions on Antennas & Propagation*, vol. 60, 06/2012, In Press

Invited Conference Publication

[ICP 1] M. J. Ammann, A. Dumoulin, M. John, and P. McEvoy, "(Invited) Time-Domain Performance of Printed UWB Antennas", *European Conference on Antennas and Propagation - EuCAP*, Berlin, 2009, 3766-3769

Conference Publications

[CP 1] A. Dumoulin, M. John, P. McEvoy, and M. J. Ammann, "An Enhanced Method to Measure Pulse Disperion in UWB Antennas", *IEEE International Symposium on Antennas and Propagation*, Chicago, 2012

[CP 2] A. Dumoulin, and M. J. Ammann, "Differentially-fed UWB Slot Antenna for Direct Board Integration", *European Conference on Antennas and Propagation - EuCAP*, Prague, 2012, A13.1

[CP 3] A. Dumoulin, M. John, P. McEvoy, and M. J. Ammann, "Optimised Tapered-Slot Antenna for Real Time Location Systems", *Communications and Radio Sciences Research Colloquium 2012*, Dublin, 2012

[CP 4] D. Gaetano, A. Dumoulin, P. McEvoy, and M. J. Ammann, "Conformal UWB Impulse Antenna for Pipe Telemetry", *Loughborough Antennas & Propagation Conference - LAPC*, Loughborough, 2011

[CP 5] A. Dumoulin, M. John, M. J. Ammann, and P. McEvoy, "Evaluation of the Effect of a Planar Reflector on the Pulse Performance of an UWB Monopole", *Loughborough Antennas & Propagation Conference - LAPC*, Loughborough, 2010, 189-192

[CP 6] A. Dumoulin, M. John, M. J. Ammann, and P. McEvoy, "Performance Evaluation of Antennas for UWB Radar and Positioning Systems", *Irish Signals & Systems Conference*, Dublin, 2009